

Layered Cathode Materials for Lithium-Ion Batteries: Review of Computational Studies on $\text{LiNi}_{1-x-y}\text{Co}_x\text{Mn}_y\text{O}_2$ and $\text{LiNi}_{1-x-y}\text{Co}_x\text{Al}_y\text{O}_2$

Arup Chakraborty,[†] Sooraj Kunnikuruvan,[†] Sandeep Kumar,[†] Boris Markovsky, Doron Aurbach, Mudit Dixit, and Dan Thomas Major^{*}



Cite This: *Chem. Mater.* 2020, 32, 915–952



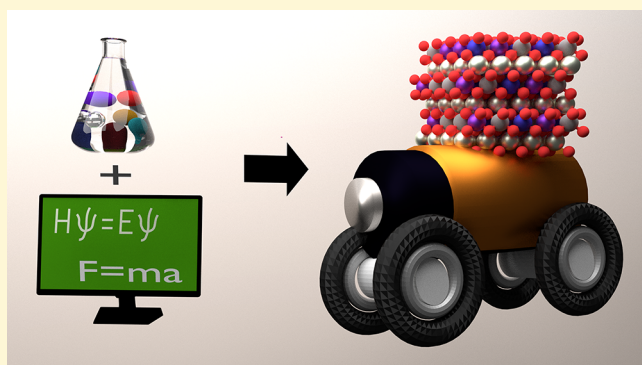
Read Online

ACCESS |

Metrics & More

Article Recommendations

ABSTRACT: At present the most successful rechargeable battery is the Li-ion battery, due to the small size, high energy density, and low reduction potential of Li. Computational materials science has become an increasingly important tool to study these batteries, and in particular cathode properties. In silico studies of cathode materials have proven to be a valuable tool to understand the workings of cathodes, without having to do sophisticated experiments. First-principles and empirical computations have been used by various groups to study key properties, such as structural stability, electronic structure, ion diffusion mechanisms, equilibrium cell voltage, thermal and electrochemical stability, and surface behavior of Li-ion battery cathode materials. Arguably, the most practical and promising Li-ion cathode materials today are layered oxide materials, and in particular $\text{LiNi}_{1-x-y}\text{Co}_x\text{Mn}_y\text{O}_2$ (NCM) and $\text{LiNi}_{1-x-y}\text{Co}_x\text{Al}_y\text{O}_2$ (NCA). Here, some of the computational approaches to studying Li-ion batteries, with special focus on issues related to layered materials, are discussed. Subsequently, an overview of theoretical and related experimental work performed on layered cathode materials, and in particular on NCM and NCA materials, is provided.



1. INTRODUCTION

Development of practical renewable energy sources is essential to meet the surging global energy needs.^{1–6} Traditional fuel sources, such as petroleum and coal, are continuously being depleted, and their combustion causes significant environmental hazards that have been connected to dire climate changes. It is therefore of utmost importance to develop energy sources that are both efficient and environmentally benign.

Several renewable natural energy sources exist, such as solar, wind, and tide,^{1,2,5,6} although practical application of these sources has been limited due in part to seasonal and geographic variations and the requirement for efficient grid-based storage systems.^{4,7} In an effort to overcome past limitations, recent years have seen intense research efforts in energy harvesting and storage areas, such as solar cells, fuel cells, super capacitors, and batteries.⁸ Perhaps the currently most ubiquitous renewable energy technology that is safe, eco-friendly, cost-effective, and portable and has high energy and power density and a good cycle life is rechargeable batteries.^{3,4,7,9–11}

At present the most successful rechargeable battery is the Li-ion battery (LIB), due to the small size, high energy density, and low reduction potential of Li (-3.04 V with respect to standard hydrogen electrode).^{12–14} Much of the research in

the field of batteries in recent years has focused on improving the performance of LIBs.^{15–31} The performance and stability of a battery depend on the properties of its components, such as cathode, anode, electrolyte, and separator.^{8,9,16,18,22,27,30,32,33} In LIBs, the cathode is often a Li intercalated transition metal oxide, while anode materials include graphite, which is most commonly used, as well as lithium titanium oxide ($\text{Li}_4\text{Ti}_5\text{O}_{12}$), lithium metal, and silicon.^{20,34} We note that the use of Li metal as the anode is restricted due to the formation of dendrites, though it can provide high capacity.³⁵ Alkyl carbonate based organic solvents (for instance, ethylene carbonate, ethyl-methyl carbonate, etc.) with Li salts, such as LiPF_6 , are the most commonly used electrolytes in LIBs, although electrolytes based on ionic liquids, solid polymers, and inorganic liquids are also used in LIBs.^{16,18,20–23,27–29,33,36} During charging, Li ions are deintercalated (extracted) from the cathode and diffuse to the anode via the electrolyte medium, which is a conductor for ions and an insulator for the electrons generated at the

Received: October 4, 2019

Revised: January 5, 2020

Published: January 6, 2020

cathode, while the electrons reach the anode via an external circuit, whereas discharging reverses this process (Figure 1).^{14,15,27,28,30,33}

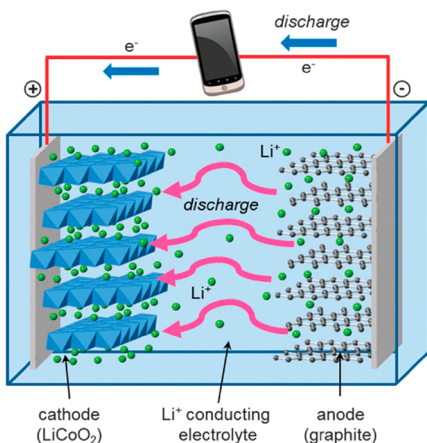


Figure 1. Schematic diagram of a first-generation rechargeable lithium-ion cell. During charging, lithium ions flow to the negative electrode through the electrolyte medium and electrons flow via the external circuit. During discharge the directions are reversed, generating electric energy. (Reprinted with permission from ref 37. Copyright 2014, published by The Royal Society of Chemistry. This image is taken from the article titled “Lithium and sodium battery cathode materials: computational insights into voltage, diffusion and nanostructural properties”, and it is under the Creative Commons Attribution 3.0 International License. To view a copy of this license, visit <https://creativecommons.org/licenses/by/3.0/>.)

The equilibrium voltage of a battery is directly proportional to the difference in chemical potentials of the cathode and the anode. The working potentials of carbon-based Li-intercalating anodes used in LIBs, such as graphite, are usually higher than

that of Li metal anodes, and their specific capacity is much lower (by a factor of 10 in the case of graphite). Thus, to improve the potential of LIBs, it is crucial to focus on the development of cathode materials with improved chemical potential. Indeed, the majority of studies reported in recent years focused on development of cathode materials for LIBs.^{3,14–18,20–25,27–29,32,33,36,38–40}

LIB cathode materials may be categorized based on their structure.^{37,41} There has been extensive research on layered-structure oxide materials, which have the formula LiMO_2 (M is a 3d transition metal, like Ni, Co, Mn, and Al, and also can be a mixture of transition metals). These layered oxides have $\alpha\text{-NaFeO}_2$ -like structures and belong to the $R\bar{3}m$ space group (Figure 2a).^{40,42} In this structure, Li and M are arranged in alternating layers, and Li and M are surrounded by a tetrahedral or octahedral environment of oxygens. Spinel structured oxide materials, LiM_2O_4 , with the space group of $F\bar{d}\bar{3}m$ (Figure 2b), have Li and M arranged in tetrahedral and octahedral environments of O. In spinel structures, there are edge sharing octahedra of MO_6 within the M layer only, with MO_6 creating a three-dimensional network with Li tetrahedra. Additionally, several polyanionic materials, such as olivine phosphate, silicate, and tavorite, have shown promise as cathodes.^{15,20,43} Olivine phosphate, LiMPO_4 , has an orthorhombic $Pnma$ structure (Figure 2c), where MO_6 octahedra and PO_4 tetrahedra are in corner-sharing networks, and MO_6 and LiO_6 share edges of their octahedra. Silicate- Li_2MSiO_4 (Figure 2d) and tavorite- LiMSO_4F (Figure 2e) have also been proposed as cathode materials. Silicates can have different types of structures, e.g., silicate with the space group $Pmn2_1$ has orthorhombic structure, while silicate with $P2_1$ has a monoclinic structure, where Li, M, and Si are surrounded by a tetrahedral environment of oxygens.⁴⁴ Tavorite structures have the space group $P\bar{1}$, i.e., triclinic structure, where MO_6 octahedra are bridged to SO_4 tetrahedra.^{32,45}

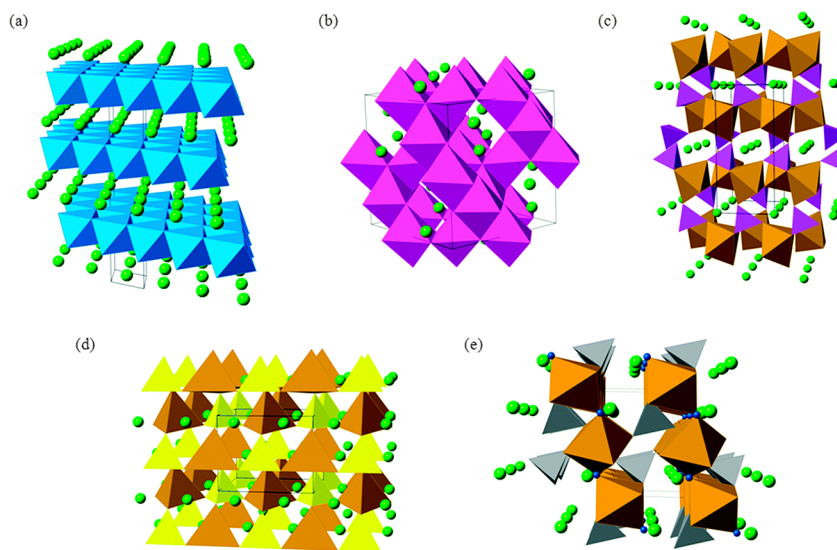


Figure 2. Representative crystal structures of cathode materials for lithium-ion batteries: (a) layered $\alpha\text{-LiCoO}_2$; (b) cubic LiMn_2O_4 spinel; (c) olivine-structured LiFePO_4 ; (d) $\beta_{\text{II}}\text{-Li}_2\text{FeSiO}_4$; and (e) tavorite-type LiFeSO_4F . Li ions are shown as light green spheres, CoO_6 octahedra in blue, MnO_6 octahedra in mauve, Fe–O polyhedra in brown, PO_4 tetrahedra in purple, SiO_4 tetrahedra in yellow, SO_4 tetrahedra in gray, and in (e) fluoride ions in dark blue. Black lines demarcate one unit cell in each structure. (Reprinted with permission from ref 37. Copyright 2014, published by The Royal Society of Chemistry. This image is taken from the article titled “Lithium and sodium battery cathode materials: computational insights into voltage, diffusion and nanostructural properties”, and it is under the Creative Commons Attribution 3.0 International License. To view a copy of this license, visit <https://creativecommons.org/licenses/by/3.0/>.)

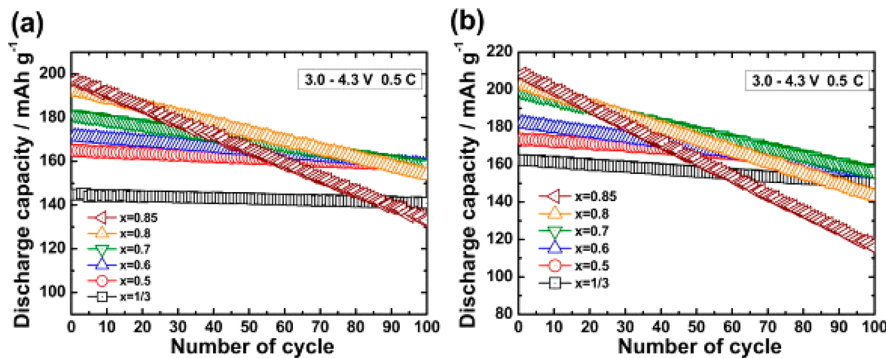


Figure 3. Discharge capacity vs cycle number for the $\text{Li}/\text{Li}[\text{Ni}_x\text{Co}_y\text{Mn}_z]\text{O}_2$ ($x = 1/3, 0.5, 0.6, 0.7, 0.8$, and 0.85) cells at (a) 25°C and (b) 55°C . The applied current density across the positive electrode was 100 mA g^{-1} (0.5C) in the voltage range of 3.0 – 4.3 V. (Reprinted with permission from ref 72. Copyright 2013, Elsevier.)

Among the above-mentioned cathode materials, layered materials are arguably the most practical and promising for LIBs.^{20,46–50} LiCoO_2 (LCO), LiNiO_2 (LNO), and LiMnO_2 (LMO) are three basic layered oxides that have been extensively studied.²⁷ LCO was first introduced in 1980 by Goodenough⁵¹ and was commercialized by Sony in 1991.⁵² In this context, we mention that the 2019 Nobel prize in chemistry was awarded to John Goodenough, M. Stanley Whittingham, and Akira Yoshino for the development of Li-ion batteries. At the heart of this Nobel prize award was the work on layered cathode materials such as LiTiS_2 and LCO cathodes in conjunction with a graphite anode.^{51,53–55} LCO ($\bar{R}\bar{3}m$ rhombohedral) has a theoretical capacity of 274 mAh g^{-1} , practical capacity of 135 mAh g^{-1} , and voltage range of 3.0 to 4.2 V for different intercalation limits of Li ions.⁵⁶ The rapid capacity fading upon cycling and high cost are major drawbacks of this material.^{15,46} Ni is cheaper than Co, but synthesis of stoichiometric LNO ($\bar{R}\bar{3}m$ rhombohedral) is quite difficult.^{57–59} The theoretical rechargeable capacity of LNO is 275 mAh g^{-1} , yet the practical capacity is only 150 mAh g^{-1} , with a voltage window of between 2.5 to 4.2 V.^{20,58,60} Due to the similar sizes of Li^+ and Ni^{2+} ions, Ni can migrate to Li sites (i.e., cation mixing), creating disorder that hinders diffusion of Li ions.^{50,61,62} Additionally, there are also structural changes during charge–discharge, which hamper cycling performance. LMO is another basic layered cathode material that is cheaper than both LCO and LNO.⁶³ LMO is mostly synthesized with an orthorhombic structure ($Pmmn$ space group), with Li–O layers corrugated. It has a theoretical capacity of 285 mAh g^{-1} , a practical capacity of 200 mAh g^{-1} , and a voltage range of 2.5 to 4.3 V.²⁰ The main disadvantage of LMO is rapid capacity fading, as the material transforms into a spinel structure upon cycling.^{64,65} The transformation of layered to spinel structure limits the specific capacity of LMO cathodes because the electrochemical activity of the latter structure is split to two domains: at 3 and 4 V vs Li–Li intercalation via phase transition at both voltage domains. This split activity forces operation at either the higher or lower potentials with half of the theoretical capacity in each domain (practically $<120 \text{ mAh g}^{-1}$), because operation throughout the potential domain causes structural degradation due to Jahn–Teller distortions.^{66,67} An additional problem of LMO cathodes is the pronounced dissolution of Mn ions into the solution phase, and the migration of these Mn ions to the anode side has a detrimental effect on their passivation.⁶⁸

Due to the drawbacks of the individual layered materials (e.g., LCO, LNO, LMO), mixing of different transition metals (TM) has been proposed as a way to improve their performance as cathode materials in LIBs. Reports on different binary layered oxide materials have shown that TM mixing is beneficial,^{50,69,70} and trinary oxides⁷¹ have shown further promise. Trinary oxides combining Ni, Co, and Mn are usually referred to as NCM ($\text{LiNi}_{1-x-y}\text{Co}_x\text{Mn}_y\text{O}_2$) or NMC, while combinations of Ni, Co, and Al are dubbed NCA ($\text{LiNi}_{1-x-y}\text{Co}_x\text{Al}_y\text{O}_2$). NCM layered materials can provide capacities in the range 200 – 210 mAh g^{-1} in the voltage range of 3.0 – 4.3 V as shown in Figure 3.⁷² Details of commercialized LIBs can be found in a review by Zeng et al.⁷³

In the mixing phase diagram in Figure 4, we show some common NCM compositions, and in Table 1 we show some commercialized NCM and NCA cathodes.

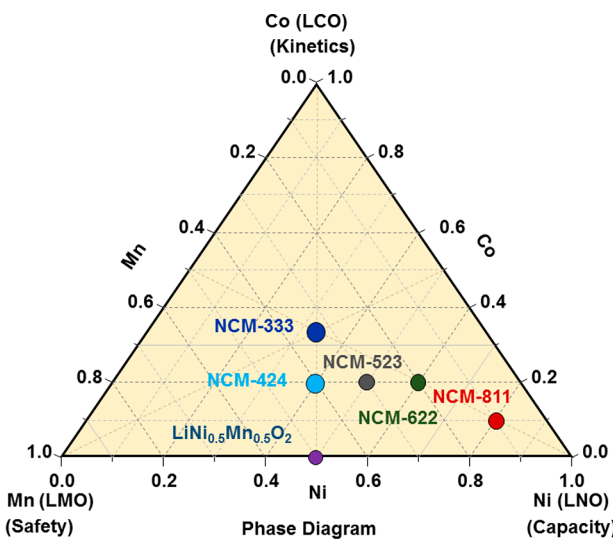


Figure 4. Phase diagram of the ternary system generated from LNO, LCO, and LMO with some representative compositions shown.

The rationale for mixing Ni, Co, and Mn is based on the important physical features that each element contributes: Ni, cathode capacity; Co, charge–discharge kinetics; and Mn, material structural stability on cycling (i.e., lower reactivity with the electrophilic electrolyte solutions based on alkyl carbonate solvents).⁸⁴ In NCM materials, Mn remains in a +4 oxidation state throughout cycling and stabilizes the structure

Table 1. List of Experimentally Determined Electrochemical Properties of Different NCM and NCA Cathode Materials

cathode material	electronic conductivity (S cm ⁻¹)	initial (first cycle) discharge capacity (mAh g ⁻¹)	voltage range (V) ^{a,b}	current density (mA cm ⁻²)	capacity retention (%)
LiNi _{0.33} Co _{0.33} Mn _{0.33} O ₂ (NCM333)	5.2 × 10 ⁻⁸ [ref 72]	163 [ref 72]	3.0–4.3 [ref 72] ^a	0.1C [ref 72]	93 [ref 76]
		150 [ref 74]	3.0–4.3 [ref 74] ^a	0.3 [ref 74]	
		150 [ref 71]	2.5–4.2 [ref 71]	0.17 [ref 71]	
		220 [ref 71]	2.5–5.0 [ref 71]	0.17 [ref 71]	
			3.0–4.6 [ref 75] ^a	0.2C [ref 75]	
LiNi _{0.50} Co _{0.20} Mn _{0.30} O ₂ (NCM523)	4.9 × 10 ⁻⁷ [ref 72]	175 [ref 72]	3.0–4.3 [ref 72] ^a	0.1C [ref 72]	95 [ref 77]
		150 [ref 77]	3.0–4.3 [ref 77]	0.4C [ref 77]	
		160 [ref 78]	4.3 [ref 78] ^b	C/3 [ref 78]	
		189.2 [ref 79]	3–4.4 [ref 79] ^b	0.2C [ref 75]	
LiNi _{0.60} Co _{0.20} Mn _{0.20} O ₂ (NCM622)	1.6 × 10 ⁻⁶ [ref 72]	187 [ref 72]	3.0–4.3 [ref 72] ^a	0.1C [ref 72]	95 [ref 76]
		178 [ref 80]	3.0–4.3 [ref 80] ^a	0.2C [ref 80]	
		~156 [ref 76]	4.2 [ref 76] ^a	1C [ref 76]	
			3.0–4.6 [ref 75] ^a	0.2C [ref 75]	
LiNi _{0.80} Co _{0.10} Mn _{0.10} O ₂ (NCM811)	1.7 × 10 ⁻⁵ [ref 72]	203 [ref 72]	3.0–4.3 [ref 72] ^a	0.1C [ref 72]	66 [ref 76]
		198 [ref 81]	3.0–4.3 [ref 81] ^a	0.1C [ref 81]	80 [ref 82]
			3.0–4.6 [ref 75] ^a	0.2C [ref 75]	
			4.2 [ref 50]	1C [ref 50]	89.3 [ref 83]
LiNi _{0.80} Co _{0.15} Al _{0.05} O ₂ (NCA815S)	200 [ref 50]	183 [ref 83]	3.0–4.3 [ref 83] ^a	0.2C [ref 83]	

^aVoltage was measured vs a lithium anode. ^bVoltage was measured vs a graphite anode.

and Co was found to reduce cation mixing, while Ni is the key redox active element in NCM, as it cycles among +2, +3, and +4 oxidation states.^{56,85–87} In NCA materials, the presence of Al improves the thermal stability of the transition metal oxides in combination with Ni and Co. Here, the stability of Al³⁺ ions in tetrahedral sites inhibits cation migration, hence avoiding phase transitions at high temperatures.⁸⁸ Guilmard and co-workers performed detailed studies on Li_xNi_{0.89}Al_{0.16}O₂ and Li_xNi_{0.7}Co_{0.15}Al_{0.15}O₂ and suggested that the migration of Al³⁺ to tetrahedral lattice sites suppresses layered-to-spinel transformation.^{89,90}

Due to the need for improved battery capacity, so-called Ni-rich cathodes constitute the state-of-the-art, and the current challenge is to achieve high capacity, without sacrificing stability and kinetics.⁵⁶ Lattice doping with cations like Na⁺, Mg²⁺, Al³⁺, Zr⁴⁺, Ti⁴⁺, W⁶⁺, and Mo⁶⁺ or anions, e.g., F⁻, and thin surface coating with inorganic oxides or salts have been suggested as solutions to capacity fading and structural stability problems in these materials.^{56,64,86,87,91–93}

Doping is a versatile technique to improve the thermodynamic, kinetic, electronic, chemical, and magnetic properties of layered cathode materials.^{64,87,94–96} To understand the effect of doping on cathode material properties, it is important to understand the effects dopants have on the intrinsic physical and chemical properties of the layered materials, as well as the effect on various types of defect, such as vacancy, substitutional, interstitial, antisite, Frenkel, and Schottky defects, which have been observed in cathode materials.⁹⁷ Important factors when considering dopants are, for instance, ionic charge, ionic size, and magnetism. Much work on dopants has focused on

the effect of dopants on the bulk properties of NCM and NCA materials.³⁹ Delmas and co-workers identified the tendency of segregation of Ni and Al in Al-substituted LNO using synchrotron X-ray powder diffraction, electron diffraction, and energy-dispersive X-ray spectroscopy (EDX) and electron energy loss spectroscopy (EELS) analyses. The authors identified an inhomogeneous distribution of Ni and Al at the surface.⁹⁸ Recent experimental work also suggests that dopants tend to segregate at the surface of cathode particles.^{78,93} Therefore, to better understand the role of dopants in NCM and NCA materials, it will be important to focus on how dopants affect surface properties.

Computational materials science has become an increasingly important tool in the field of LIB.⁹⁹ Cathode properties, such as equilibrium voltages and voltage profiles, ion mobilities, thermal stability, and TM oxidation states, may readily be computed.¹⁰⁰ Using related techniques, one can also estimate the properties of additional battery components¹⁰⁰ such as anode materials,^{101–104} solid electrolytes,^{105–107} and the electrode surface.¹⁰⁸ Early studies in this area addressed computation of cathode properties employing density functional theory (DFT) and showed that theory is capable of reproducing cathode properties from first principles.^{109–111} These pioneering works addressed layered cathode materials but have since penetrated just about every area of battery components.

First principles computations were used by various groups to study key properties, such as structural stability, electronic structure, ion diffusion mechanisms, equilibrium cell voltage, thermal and electrochemical stability, and surface behavior of

LIB cathode materials.^{37,112–114} In 1997, Aydinol et al. calculated the equilibrium cell voltage from first-principles using the so-called DFT local density approximation and found voltage trends similar to those of experiments.^{109,110} Also, the average intercalation voltage of layered LiMO₂ was calculated by Benco et al. using DFT.¹¹¹ First principles calculations have also been used to determine the diffusion rate and mechanism of Li ions in LIBs.^{115–117} Furthermore, Ceder and co-workers revealed that rate capacity of the layered cathode materials can be enhanced by the integration of low-valent transition-metal cations, which results in low strain in the activated state.¹¹⁸ In 2011, Ceder and co-workers implemented high-throughput computational strategies within a DFT framework to design new cathode materials for LIBs.^{112,113} The many advances in theoretical studies, together with improved computational resources, allow design of new materials based on guidance from computational studies.¹¹⁹ A general overview of the application of computational studies on battery materials can be found elsewhere.^{37,41,100,114}

In the following we will focus on theoretical studies of layered cathode materials and refer the interested reader to excellent reviews by Islam,³⁷ Ceder,¹⁰⁰ Meng,⁴¹ and others for a wider perspective on the role of theory in battery research.^{50,84,99,114,120,121} The current review is arranged as follows: In **Section 2** we discuss some of the computational approaches to studying LIBs, with special focus on issues related to layered materials. Subsequently, in **Section 3** we provide an overview of theoretical work performed on layered cathode materials, and in particular on NCM and NCA materials.

2. COMPUTATIONAL METHODS FOR CATHODE MATERIALS

2.1. Potential Energy Surface (PES). The PES is a key ingredient of any theoretical study of cathode materials in a LIB. The available methods may be categorized as quantum mechanical (electronic structure) or classical mechanical methods. In the following we give an overview of the most common approaches for treating the PES of cathode materials.

2.1.1. Electronic Structure Methods. The electronic structure of matter plays a crucial role in determining the physical and chemical properties of layered cathodes, and it is therefore essential to choose a suitable theoretical framework when modeling such materials. Quantum mechanics provides the necessary mathematical framework via Schrödinger's wave equation or density functional theory (DFT).^{122–124} The latter has been applied extensively to model NCM and NCA materials, as it is considerably cheaper computationally than wave function methods of comparable accuracy. The energy within DFT is written as

$$\begin{aligned} E[\rho(\mathbf{r}); \mathbf{R}] = & T[\rho(\mathbf{r})] + E_{xc}[\rho(\mathbf{r})] + \int V_{ij}[\rho(\mathbf{r})] d\mathbf{r} \\ & + \int \rho(\mathbf{r}) V_{ext}[\rho(\mathbf{r}); \mathbf{R}] d\mathbf{r} \end{aligned} \quad (1)$$

where $\rho(\mathbf{r})$ is the electron density, the first term on the right-hand side is the kinetic energy of the electrons, the second term is the exchange-correlation (XC) energy, the third term is the electron-electron repulsion, and the last term is the electron-ion attraction. \mathbf{R} represents the nuclear coordinates, while \mathbf{r} describes the electronic coordinates. The exact form of the XC term is unfortunately not known and must be approximated, and a range of different functionals have been

suggested over the years. These XC functionals may be categorized as belonging to the following types of DFT with increasing complexity:^{125,126} local density approximation¹²³ (LDA; dependence on electron density), generalized gradient approximation¹²⁷ (GGA; + dependence on gradient of the electron density), meta-GGA^{128,129} (+ dependence of kinetic energy density), hybrid functionals (+ dependence on exact Hartree–Fock exchange via the occupied orbitals^{130,131}), and double hybrid functionals¹³² (+ dependence on virtual orbitals). The GGA family of functionals is by far the most commonly employed for layered cathode materials, and in particular the Perdew–Burke–Ernzerhof (PBE) functional¹³³ has been widely used. This functional has been shown to provide good structural and energetic properties. Typically, the LDA and GGA functionals suffer from so-called electron self-interaction, a peculiar deficiency that is partly resolved in higher rung functionals, such as hybrid functionals. However, the usually improved performance of hybrid functionals comes at a computational overhead, and a significantly cheaper strategy to deal with self-interaction is via inclusion of Hubbard U parameters, where U is an on-site Coulomb interaction parameter.^{134,135} DFT+U (e.g., PBE+U) can predict the properties of strongly correlated systems more accurately than standard local and semi-local DFT functionals. The common practice is choosing a constant U value that produces properties matching experimental observations. First principle calculations may be used to determine optimal U values for a particular system. For instance, one can use the constrained random phase approximation (cRPA) or DFT + dynamical mean field theory (DMFT) and linear response to get proper values of U for a particular system (as implemented in the Quantum ESPRESSO package).^{136,137} In spite of the success in using DFT+U in materials chemistry, there are certain caveats when using DFT+U to study electrochemistry, as will be discussed below.¹³⁸ This is because constant U values can lead to incorrect results when there is change in the physical composition or conditions of the material or the material undergoes a structural transition.¹³⁶ Ideally, the value of U should depend on the position of all atoms within the lattice, as well as the magnetic and electronic states of the system. Along these lines, Kulik and Marzari showed that U depends on the position of the atoms, and this position dependent DFT+U(R) approach can predict properties like binding energies, frequencies, and equilibrium bond length better than standard DFT+U.¹³⁹ A recent approach termed DFT+U+V, considering on-site U and intersite (V) effective interactions, can predict properties for mixed valence ground states and can treat localized states in partially delithiated cathode materials, like olivine phosphates.¹⁴⁰

Many DFT approaches do not properly account for the dispersion interaction, and these are often added as empirical corrections.^{141–145} The importance of dispersion corrections in modeling layered cathode materials will be emphasized below in **Section 2.3.1**. A very useful recent DFT method from the meta-GGA family that shows good performance for layered LIB systems is the strongly constrained and appropriately normed (SCAN) semilocal density functional.^{138,146}

In practice, many solid-state DFT codes are implemented using plane waves as a basis set, using the projected augmented wave (PAW) method.¹⁴⁷ Within this plane wave basis set approach, many codes also employ pseudopotentials, forming an efficient computational framework. The pseudopotential approach relies in the reasonable assumption that the valence

electrons determine most of the properties of molecules and solids, whereas the core electrons are inert and retain their atomic character even when engaged in bonding. This pseudopotential approach is the basis of many modern electronic structure packages such as Quantum ESPRESSO,¹⁴⁸ ABINIT,^{149,150} CASTEP,¹⁵¹ and VASP.^{152–154} The forces acting on atoms and the stress on unit cells may be computed using the Hellmann–Feynman theorem.¹⁵⁵

The NCM and NCA materials are magnetic, largely due to the coexistence of transition metals, namely, Ni, Co, Mn, and Al, and possible dopants. It is essential to identify the lowest energy configuration for spin-polarized systems, and this can be a challenge in NCM and NCA materials. In some of the NCM and NCA materials studied computationally, antiferromagnetic (AFM) configurations are found to be energetically favorable compared to ferromagnetic (FM) configurations (Table 2). It is of great practical importance to choose reasonable initial guess magnetic moments to facilitate rapid convergence for large, spin-polarized systems.

Table 2. Selected NCM and NCA Materials and Their Energetically Favorable Magnetic Configuration

type of NCM	energetically favorable configuration
NCM333 ^{156,157}	antiferromagnetic (AFM)
NCM523 ⁸⁵	antiferromagnetic (AFM)
NCA ¹⁵⁸	antiferromagnetic (AFM)

It is possible to estimate the electronic configuration and formal oxidation states of transition metals from the calculated magnetic moments per atom and projected density of states (PDOS).^{85–87,91} A related tool that can quantify the local electronic environment around atoms and can be useful in NCM/NCA materials is the Bader charge analysis scheme.¹⁵⁹ An additional useful tool is the crystal orbital Hamiltonian population (COHP) method, which can deduce the covalent vs ionic contribution in bonds.^{160–162}

2.1.2. Electronic Structure with Cluster Expansion. The electronic structure for layered oxide LIB cathode materials is most often calculated using DFT, and this works well if one has an atomic resolution crystal structure of the system. However, the structures of NCM and NCA materials are complicated to model due to ionic mixing in the TM layers, as well as possible mixing between Li and TM.^{50,61,62} When the system modeled is large, it can be prohibitively expensive to evaluate all possible configurations using DFT, and alternative approaches must be sought. There are many proposed approaches to find stable structures for binary or ternary alloys, and such methods can be applied for NCM and NCA as well. One such method, the cluster expansion (CE) approach, which is implemented in the Alloy Theoretic Automated Toolkit (ATAT) code^{163,164} and the Clusters Approach to Statistical Mechanics (CASM) code,^{165–167} has been applied to NCM and NCA materials.^{168,169} The CE method is adopted from the Ising model of statistical mechanics, where the total lattice is constructed from different possible clusters at lattice sites. The total energy for a configuration can be obtained by considering the energetic contributions from different clusters (σ) at the lattice sites, $E(\sigma)$:

$$E(\sigma) = E^{\text{CE}}(\sigma) = \sum_f J_f \Pi_f(\sigma) \quad (2)$$

Here, J_f denotes the “effective interaction strength” (an energy term) associated with a particular combination of lattice sites, f . The sum runs over all possible inequivalent “types” of lattice site combinations f , such as nearest-neighbor pairs, second-nearest-neighbor pairs, a nearest-neighbor triplet, etc. σ depends on the nuclear coordinates R . $\Pi_f(\sigma)$ are spin-products averaged over the entire lattice, which are different for each given configuration, σ . Further details can be found in refs 163 and 164.

The energies for these different predicted configurations are calculated using CE and are fitted with DFT for a few selected configurations. The calculations continue until they reach a convergence criterion. The energy profile for different configurations forms a convex hull, and one can get the most stable structure from the minimum energy of the convex hull.¹⁶³

2.1.3. Classical Mechanics Methods. The computational time for DFT computations scales formally as N^3 (LDA and GGA), where N is the number of basis functions, and this limits the size of the model systems treated by DFT. As the reliability of computational predictions depends greatly on the choice of an accurate atomistic model, it is important to construct a system that is large enough to predict the material properties of interest. In many cases, DFT is impractical for systems beyond a few hundred atoms,^{170–172} and computationally cheap approaches that can model large systems are vital.^{37,173}

Classical simulation approaches constitute one possible avenue that can reduce the computational cost significantly. In this approach, explicit treatment of electrons is omitted by using predefined internuclear potentials. As the electronic degrees of freedom are taken in an average way, the total energy of the system in this approach is a function of nuclear coordinates only. Molecular mechanics, or force fields, is a popular approach,¹⁷⁴ where the energy function for an N -nuclei system has the following general form

$$\begin{aligned} E(\mathbf{R}) = & \sum_{\text{bonds}} k_i(R_i - R_{i,0})^2 + \sum_{\text{angles}} k_i(\theta_i - \theta_{i,0})^2 \\ & + \sum_{\text{torsions}} \frac{V_n}{2}(1 + \cos(n\phi - \omega)) + E_{\text{ele}} + E_{\text{vdw}} \end{aligned} \quad (3)$$

In this equation, the total potential energy, E , of an atomistic system is written as a sum of bonded (first three terms) and nonbonded terms (last two terms). Here, the bonded terms include the bond stretching, angle bending, and torsional components, and the nonbonded terms include electrostatic (E_{ele}) and van der Waals (E_{vdw}) contributions to the potential energy. In the above equation, k_i represent the harmonic force constant for bond stretching and angle bending in the first two terms on the right-hand side. R , θ , and ϕ are the bond length, angle, and dihedral, respectively, and R_0 and θ_0 are the equilibrium bond length and angle, respectively. V_n in the third term represents the rotational barrier height, and n represents the number of minima over a complete rotation of a bond. Usually, a Lennard-Jones or a Buckingham potential is used for E_{vdw} , and a Coulombic potential is used for E_{ele} . Charge polarization may be included via approaches such as point ion dipolar polarizability¹⁷⁵ and the core–shell model or the Drude oscillator model.¹⁷⁶ Among these, the core–shell model is the most widely used approach for atomistic simulation of LIBs.^{43,97,177} Among various classical simulation packages,

GULP¹⁷⁸ and DL_POLY¹⁷⁹ programs have been widely used.³⁷

Though potential based approaches are computationally cheap, harmonic potentials and fixed-point charges cannot mimic the complex bonding patterns and changes in the electrostatic environment during the ion diffusion in battery materials. This is particularly difficult for cathode materials, such as NCM and NCA, where more than one type of transition metal is present, and each metal may be present in different oxidation states, which may change as a function of atomic position. Thus, development of accurate and flexible potential models is necessary for an efficient application of these approaches. Recently, coupling of variable charge models with empirical potential parameters such as the charge transfer modified nearest neighbor molecular embedded atom method (CT-MEAM)¹⁸⁰ and second nearest neighbor molecular embedded atom method coupled with charge equilibration (2NNMEAM+Qeq) have been used for diffusion studies in battery materials.¹⁸¹

2.2. Traversing the Potential Energy Surface. Minimization of the energy functions (eqs 1–3) with respect to the nuclear coordinates, \mathbf{R} , using established minimization algorithms are employed to determine the minimum energy configurations on the PES. For solid-state materials, such minimization includes the relaxation of lattice parameters along with the nuclear coordinates under periodic boundary conditions.

Diffusion constants of Li^+ ions and their solid-state diffusion mechanisms are important properties for the electrochemical performance of battery materials. The molecular dynamics (MD) simulation technique is one of the most popular approaches for such studies. Here, Newton's equations of motion are solved numerically to generate the trajectory for a system over a time period at finite temperature and pressure to obtain time dependent and average equilibrium properties. The time scales that can be achieved by using ab initio MD (AIMD) simulations are often limited to a few picoseconds for hundreds of atoms, whereas MD simulation utilizing predefined empirical potentials can achieve nano- to microseconds time scale even for tens of thousands of atoms, depending on available computational facilities. An additional method to traverse the PES to probe diffusion is the nudged elastic band (NEB) method.¹⁸² NEB allows one to find the minimum energy diffusion paths in complex, high-dimensionality systems, such as NCM and NCA materials. The NEB method is discussed in greater detail below (Section 2.3.4).

2.3. Computable Properties in Cathode Materials. **2.3.1. Structural Properties.** LIB oxide cathode materials have different structures, like rhombohedral, monoclinic, and spinel. The rhombohedral structure, with space group $R\bar{3}m$, is the most common one for NCM and NCA materials, and it has a prototype $\alpha\text{-NaFeO}_2$ structure.^{40,128,157,183} In this structure, TMs and Li atoms are arranged in alternating layers, and the cations are located in a tetrahedral or octahedral environment of O atoms (Figure 5). The stacking of the cations depends on the coordination (octahedra/tetrahedra) of the Li atoms, and these can be of different types, e.g., O1, O3, P3, O2, and P2. The nomenclature is as described by Delmas et al.,^{40,42} i.e., O is for octahedra, P for prismatic, and T for tetrahedra.

In layered NCM cathode materials, the TMs may form repeating clusters or patterns within the TM planes. Koyama et al. showed that the superlattice model of $[\sqrt{3} \times \sqrt{3}] R30^\circ$ (in Wood's notation) type is energetically favorable compared to a

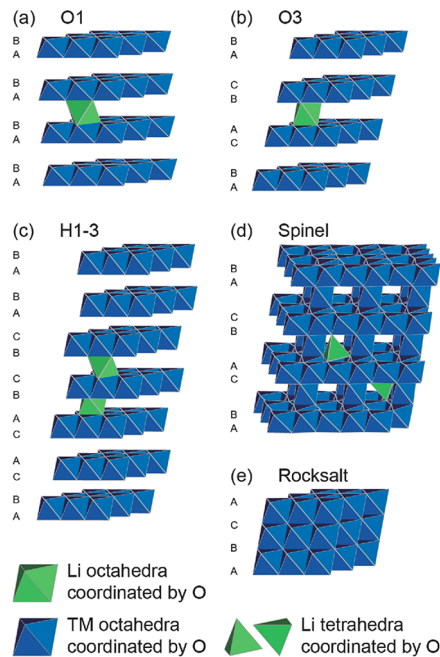


Figure 5. Crystal structures relevant for layered Li intercalation electrodes. Blue octahedra represent MO_6 units, and green octahedra/tetrahedra represent Li sites. (Reprinted with permission from ref 40. Copyright 2017, Wiley-VCH.)

piled up model from NiO_2 , CoO_2 , and MnO_2 sublayers for $\text{Li}[\text{Co}_{1/3}\text{Ni}_{1/3}\text{Mn}_{1/3}]\text{O}_2$ (NCM333) materials.¹⁸⁴ Using high-resolution solid-state ^6Li NMR spectroscopy, Cahill et al. observed local (short-range) TM ordering, with clustering of Mn^{4+} and Ni^{2+} in NCM333.¹⁸⁵ Importantly, such configurations avoid high-energy $\text{Mn}^{4+}\text{-Mn}^{4+}$ contacts. Subsequently, Zeng et al. similarly showed that layered mixed TM oxides (such as NCM333) exhibit a $[\sqrt{3} \times \sqrt{3}] R30^\circ$ type local ordering in the TM layers.¹⁸⁶ These authors also showed that NCM333 has a tendency to form $\text{Ni}^{2+}\text{-Mn}^{4+}$ local clusters, whereas the Co^{3+} ions adopt random positions. Using electron diffraction experiments, Weill et al. observed $\sqrt{3} \times \sqrt{3}$ superstructures in the transition metal layers in $\text{LiNi}_{0.425}\text{Co}_{0.425}\text{Mn}_{0.15}\text{O}_2$.¹⁸⁷ Meng et al. studied $\text{Li}[\text{Ni}_x\text{Li}_{1/3-2x/3}\text{Mn}_{2/3-x/3}]\text{O}_2$ for $x = 0, 1/2$, and $1/3$, and in-plane $\sqrt{3} \times \sqrt{3}$ ordering was also noted in all of the above samples.¹⁸⁸ The stability of a structure for NCM and NCA can be determined theoretically using DFT, cluster expansion, or classical potential methods, as discussed in the previous section. Using first-principles calculations, Yu et al. explored $\text{LiNi}_{0.42}\text{Mn}_{0.42}\text{Co}_{0.16}\text{O}_2$ and suggested that Co $\sqrt{3}$ ordering is most stable among the different orderings studied.¹⁸⁹ Dixit et al. predicted the cationic ordering of NCM523 and also noted that cationic ordering of $\sqrt{3}$ -type ordering parameters are more stable than the structures with other types of ordering.⁸⁵ The authors presented a systematic funneled approach for predicting cationic ordering of NCMs by employing a classical mechanical atomistic energy function for initial screening of a large number of configurations, followed by DFT rescored of the lowest energy configurations from the classical calculations. Sun and Zhao studied the energetics for different configurations of various NCM materials (NCM333, NCM523, NCMC424, NCM811, NCM622), and they have shown that there is no such favorable long-range ordering pattern for TM

in superlattice models in the case of Ni, Co, and Mn, in contrast to the short-range ordering discussed above.¹⁹⁰

Significant changes may occur in the lattice parameters a and c of the unit cell of $\text{R}\bar{3}m$ NCM and NCA during cycling. This may occur as a result of lithiation and delithiation, and it has been shown that the c parameter can have a rather complicated behavior as a function of Li content.¹⁹¹ Specifically, it is important to include dispersion interactions to correctly reproduce the experimentally observed c parameter behavior.^{85,86,191,192} Changes in cell parameters can also occur as a result of local phase changes taking place, e.g., layered to spinel transformation.^{14,193}

The LDA functional was found to correctly predict the decreasing trend of c lattice parameters with decrease in Li concentration in the case of Li_xTiS_2 , as LDA is known to exhibit overbinding at short range, whereas the GGA functional was found to predict the opposite trend.¹¹⁵ However, the c lattice parameters predicted by LDA are consistently lower than the experimentally measured values.¹¹⁵ Underestimation of the c lattice parameter was also observed for LiCoO_2 , LiMnO_2 , LiNiO_2 , and NCM333 using LDA.^{184,194} The PBE and PBE+U functionals fail to reproduce the experimentally observed trend in the change of c lattice parameters during Li deintercalation (initial increase with decreasing Li concentration followed by a decrease during the last stage of delithiation).^{85,195} A comparison of c lattice parameters for NCM523 computed with and without dispersion with the PBE functional indicated that dispersion correction is vital for predicting the experimentally observed value and trend in the c lattice parameter with varying Li concentration for NCM523.⁸⁵ This is in line with calculations on LCO by Aykol et al.¹⁹² Further, Yoshida et al. also showed that DFT with a van der Waals exchange-correlation functional is essential to reproduce the contracting nature of LNO with delithiation.¹⁹⁶ Since the diffusion kinetics depends on the interlayer separation and thus the c lattice parameter, it is important to use functionals that include dispersion correction.⁸⁵ We recently showed that the SCAN functional, as well as PBE+U+D3, reproduce well the changes in lattice parameter with delithiation, as shown in Figure 6.¹³⁸

2.3.2. Electronic Structure. One can compute relevant electronic properties, such as band gap, density of states (DOS), and magnetic moments, using an electronic structure method, such as DFT. Additionally, one can predict derived properties that depend on the electronic structure, such as oxidation states. The accuracy of the prediction of these properties will depend on the level of theory employed, such as LDA, GGA, LDA/GGA+U, meta-GGA, hybrid functional, and double hybrids.^{123,124,129–133} It is prudent to benchmark the electronic structure method against available experimental data, such as band gap and X-ray photoelectron spectroscopy (XPS), for the material of interest.^{37,100,197} Yet, subtleties may come up, such as perturbation of the electronic structure due to the use of U parameters.^{135,197} Adding empirical Hubbard U parameters to PBE often improves the band gap and average voltages but can perturb the electronic structure in the process.^{85,138} Also, + U approaches are fundamentally problematic for electrochemical (de)intercalation processes, as the oxidation states of transition metals change during the course of (de)intercalation, and the U parameter depends on the oxidation states; however, U cannot be changed with charge state/oxidation state to calculate continuous (de)intercalation processes, as + U with varying values is not a constant

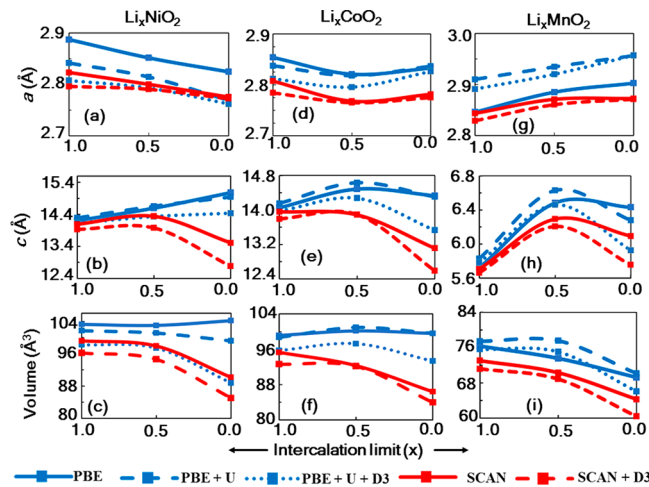


Figure 6. Variation in unit cell lattice parameters, a , c , and volume, at different intercalation levels (x) for Li_xNiO_2 , Li_xCoO_2 , and Li_xMnO_2 using different functional combinations. (Reprinted with permission from ref 138. Copyright 2018, Springer Nature. This image is used under the Creative Commons Attribution 4.0 International License. To view a copy of this license, visit <https://creativecommons.org/licenses/by/4.0/>.)

operator.^{85,91} For instance, for NCM523, the DOS obtained using the PBE+U method (with constant U values of the TMs) predicts a high contribution of oxygen states near the Fermi level, whereas the TM d-states are found to be shifted to energies significantly below the Fermi level.⁹¹ Such locations of d states of the TMs and p states of oxygens are at odds with the known electrochemical activity based on classical redox.

An additional detail worth noting is that even though empirical dispersion corrections do not affect the electronic structure directly, an indirect effect might be observed due to different ionic minima positions or cell parameters.¹⁴⁴

Some layered oxide materials are small gap insulators, e.g., LiCoO_2 has a band gap of 2.7 eV.¹⁹⁸ In comparison, the band gaps of LiMnO_2 and LiNiO_2 are 1.64 and 0.4 eV, respectively.^{195,199} In mixed NCM materials, the band gap closes as one introduces more Ni (Figure 7).¹⁹⁰ LDA and GGA functionals often underestimate the band gap in these materials,¹³⁵ and it is necessary to include Hubbard U (with appropriate U values) for the TMs to open up the band gap. Alternatively, one may employ hybrid or meta-GGA functionals, such as SCAN,¹³⁸ where the inclusion of some exact exchange or kinetic energy density can reduce electron self-interaction and open up the band gap.

Calculation of DOS for the materials is an important tool to understand the crystal field d-orbital splitting (e_g and t_{2g}) and the hybridization of different orbitals. For instance, the Ni-ion d-orbitals are located close to the Fermi level, as expected for the electrochemically active ion. Additionally, in NCMs the TM d-orbitals are usually hybridized with oxygen p-orbitals, and these states are located near the Fermi energy (Figure 8).

The TM ions in NCM and NCA materials often have a multitude of possible formal oxidation states. For example, Ni can be in 2+/3+/4+ states, and Co can be in 3+/4+ states, while Mn can be in 3+/4+ states.^{16,47,156} Different spin states of TMs in NCM and NCA materials that can exist at various Li-intercalation states are shown schematically in Figure 9. Understanding the coexistence of multiple TM oxidation states in NCM materials is crucial, as it determines much of the

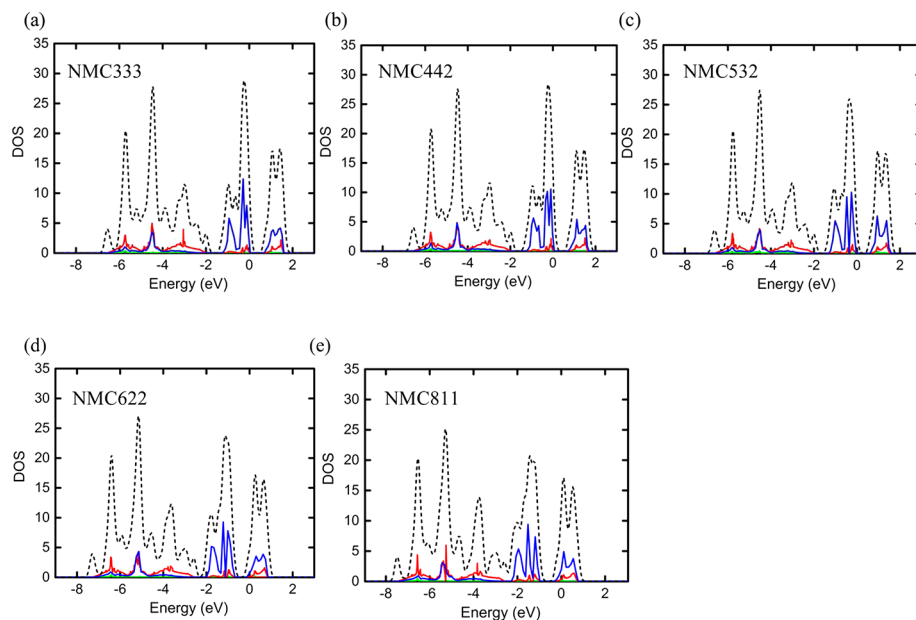


Figure 7. Total and partial densities of states for (a) NMC333, (b) NMC442, (c) NMC532, (d) NMC622, and (e) NMC811, respectively. The dashed lines represent the total densities of states. The blue, red, and green lines represent the partial densities of states of the TM 3d, O 2p, and Li s orbitals, respectively. The Fermi energy is shifted to zero. Energy levels below -4 eV show large overlaps between O 2p and TM 3d orbitals due to strong covalent interactions. The t_{2g} population for the TM 3d orbitals dictates the energy range of -2 to 0 eV. The higher energy region above the Fermi level includes antibonding states composed of TM 3d e_g^* orbitals and O 2p orbitals. The band gap gradually closes, and the Fermi energy shifts to larger values from NMC333 to NMC811 due to the increasing amount of Ni. (Reprinted with permission from ref 190. Copyright 2017, The American Chemical Society.)

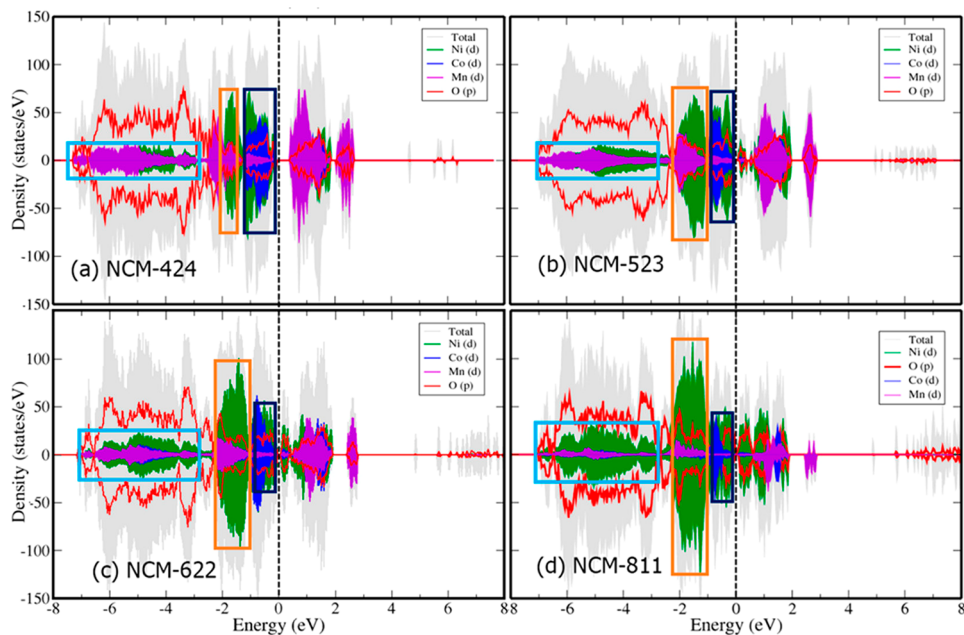


Figure 8. Densities of states for (a–d) NCM-424, NCM-523, NCM-622, and NCM-811, respectively. The center, right, and left boxes indicate the Ni- t_{2g} band, Ni- e_g band, and metal character in hybridized O-metal bonding states, respectively. (Reprinted with permission from ref 86. Copyright 2017, The American Chemical Society.)

electrochemical behavior and issues such as capacity fading.⁸⁶ For instance, the number of Ni^{2+} ions decreases, with a concomitant increase in the number of Ni^{3+} ions, with increasing Ni contents in NCM materials, e.g., from NCM333 to NCM811.⁸⁶ One can predict the oxidation state of metal ions from the occupancy of different orbitals and the spin states (i.e., magnetic moments) of the atoms (Figure 10).

The oxidation state of TMs is also important for understanding phenomena such as Ni/Li disorder. Li/Ni cation disorder can take place between Li^+ and Ni^{2+} or Ni^{3+} ions. The similar sizes of Ni^{2+} and Li^+ suggest that Ni^{2+} is most prone to diffuse into the Li-layer. However, Zheng et al.²⁰⁰ suggested cation disorder involving both Ni^{2+} and Ni^{3+} ions with Li^+ ions and that this depends on the exchange interaction between the TMs. These authors employed the PBE+U

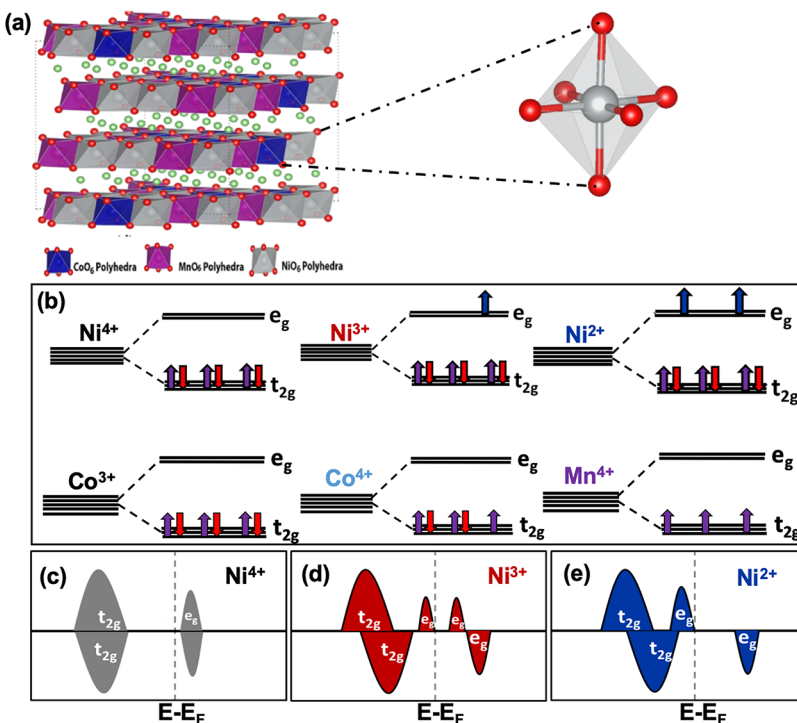


Figure 9. (a) Structure of $\text{LiNi}_{0.5}\text{Co}_{0.2}\text{Mn}_{0.3}\text{O}_2$. (b) Electronic configuration of Ni^{4+} , Ni^{3+} , Ni^{2+} , Co^{3+} , Co^{4+} , and Mn^{4+} in MO_6 octahedra in NCM523. (Reprinted with permission from ref 85. Copyright 2016, published by the PCCP Owner Societies.) Schematic DOS for (c) Ni^{4+} , (d) Ni^{3+} , and (e) Ni^{2+} in NCM811. (Reprinted with permission from ref 86. Copyright 2017, The American Chemical Society.)

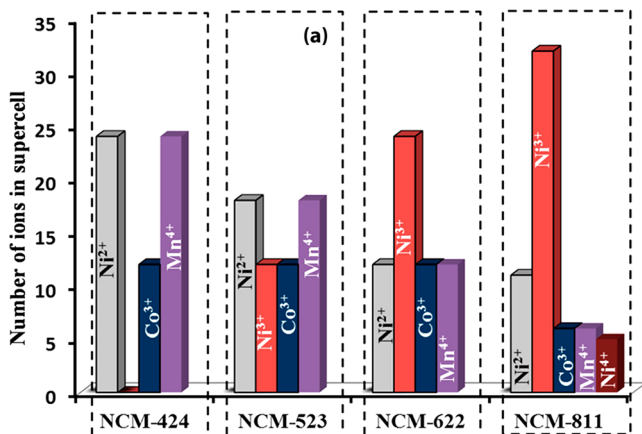


Figure 10. Oxidation states of transition metal ions in various NCMs. (Reprinted with permission from ref 86. Copyright 2017, The American Chemical Society.)

method, combined with experiments, to show that Ni^{3+} ions prefer to exchange with Li, and changed the oxidation state to 2+ to stabilize antiferromagnetic interactions with Ni^{2+} ions through superexchange interactions via oxygen. In such studies, electronic structure methods are essential to understand ion disorder, as well as the redox behavior of the TMs.

Zhang et al. also explored the role of cation disorder and reconstruction of NiO_6 octahedra in Ni-rich layered oxides.²⁰¹ They showed from experiment and theoretical calculations that symmetry breaking and reconstruction of NiO_6 dictate the Li/Ni migration pathways due to a comparable activation barrier for migration of Ni and Li ions.

2.3.3. Intercalation Voltage. The volumetric or gravimetric energy density of a battery depends on the open circuit voltage (OCV). Thus, materials that provide a high voltage along with

an electrolyte that is stable at this voltage are crucial for developing high energy density batteries. The voltage of a battery, $V(x)$, depends on the chemical potential of the cathode and anode and is defined as¹⁰⁹

$$V(x) = -\frac{\mu_{\text{cathode}}(x) - \mu_{\text{anode}}(x)}{zF} \quad (4)$$

Here, μ_{cathode} and μ_{anode} are the chemical potentials of the cathode and the anode, respectively, z is the number of charge units that are transferred, x is the chemical composition, and F is Faraday's constant. In the case of LIBs the value of z is typically 1 and the chemical potentials are the chemical potential of Li in the cathode and anode. As the chemical potential is related to the change in free energy with respect to the change in Li concentration in LIBs, the average equilibrium voltage can be written as

$$\bar{V} = \frac{-\Delta G_r}{\Delta x F} \quad (5)$$

Here, ΔG_r is the difference in free energy between the fully lithiated and delithiated states and Δx is the number of Li ions transferred. For solid-state materials the entropic contribution to ΔG_r is expected to be negligible at room temperature (<0.01 eV),^{37,100,109,114} and therefore the free energy difference, ΔG , can be approximated as the potential energy difference, ΔE . Therefore, the above equation can be written as

$$\bar{V} = \frac{-\Delta E_r}{\Delta x F} \quad (6)$$

In the case of the Li (de)intercalation reaction in LiMO_2 , $\text{Li}_{x_1}\text{MO}_2 \rightleftharpoons \text{Li}_{x_2}\text{MO}_2 + (x_1 - x_2)\text{Li}$, \bar{V} can be written as

$$\bar{V} = -\frac{(E_{\text{Li}_{x_1}\text{MO}_2} - E_{\text{Li}_{x_2}\text{MO}_2}) - (x_1 - x_2)E_{\text{Li}}}{(x_1 - x_2)F}, \quad x_1 > x_2 \quad (7)$$

The potential energies of $\text{Li}_{x_1}\text{MO}_2$ ($E_{\text{Li}_{x_1}\text{MO}_2}$), $\text{Li}_{x_2}\text{MO}_2$ ($E_{\text{Li}_{x_2}\text{MO}_2}$), and $\text{Li}(E_{\text{Li}})$ can be determined using electronic structure methods, such as DFT.

One can also compute the voltage as a continuous function of change in Li ion concentration, $V(x)$, to generate a voltage profile. The voltage profile is more important for materials having multiple transition metals such as NCM and NCA, as the oxidation state of the transition metals varies with varying x . Moreover, the nature of the voltage curve can provide vital information about phase transitions occurring in the material as x changes.²⁰² However, the voltage profile computation requires the structures of the materials at various values of x . Here, eq 6 can be used to obtain the average equilibrium voltage for different concentrations intervals, x and $x + dx$. Since the averaging is performed at each interval, the voltage profile obtained will be a step-like curve (Figure 11a). Instead

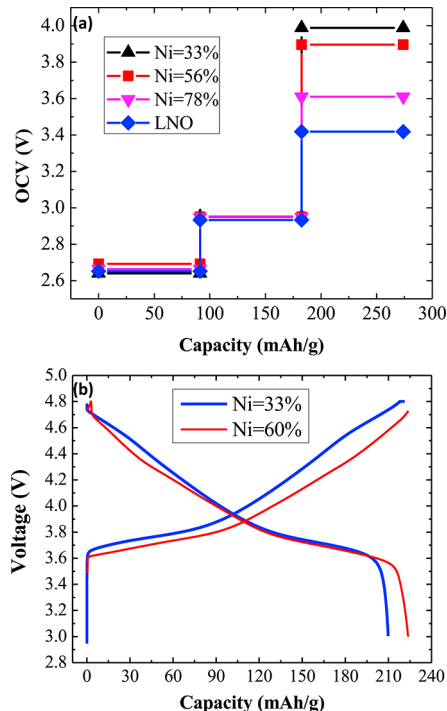


Figure 11. (a) Calculated OCV vs capacity for all $\text{Li}_{1-x}\text{MO}_2$ ($0 \leq x \leq 1$) NCM structures (Ni = 33%, 56%, 78%, and 100%). The theoretical maximum capacity of 274 mA h g^{-1} is used. (b) Experimental results of voltage vs capacity for NCM structures with Ni = 33% and 60%. (Reprinted with permission from ref 191. Copyright 2016, Elsevier.)

of computing voltages for a few selected intervals, it is also possible to obtain voltages for all the compositions by combining first-principles computations with a Monte Carlo (MC) simulation approach, which can provide chemical potential with varying x . Then, by using eq 7, the voltage profile can be computed.^{37,100}

DFT methods based on LDA and GGA were found to underestimate voltages, and this has been ascribed to the electron self-interaction error.^{37,100,203} However, in spite of the inherent self-interaction error, LDA and GGA calculations have successfully predicted voltage trends of layered oxide

materials.^{85,87,156,204,205} Adding Hubbard U correction to GGA functionals can correct for the self-interaction error and, hence, often provides absolute voltages in better agreement with experiment (see Figure 12). Nonetheless, since the oxidation

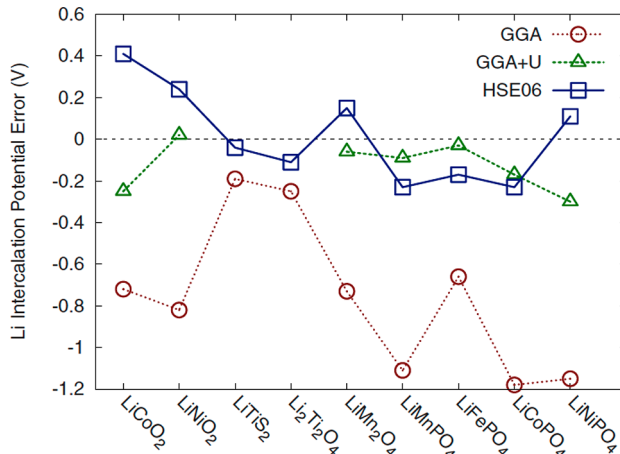


Figure 12. Difference between calculated and experimental Li intercalation potentials for GGA, GGA+U, and HSE06. (Reprinted with permission from ref 100. Copyright 2016, Springer Nature. This image is used under the Creative Commons Attribution 4.0 International License. To view a copy of this license, visit <https://creativecommons.org/licenses/by/4.0/>.)

states of TMs change during (de)intercalation, different U values might be needed, and as mentioned above (Section 2.3.2), this is problematic. Surprisingly, sometimes a U value that gives an overall correct electronic structure might not predict the average voltage correctly. As noted for LiCoO_2 , the Co U value that predicts an accurate electronic structure ($U \sim 2.9$) does not accurately reproduce the experimental average voltage value, and a higher U is often selected ($U = 4.9$) to obtain the correct average voltage of LiCoO_2 .^{206,207} Hybrid functionals, which correct for some of the self-interaction, were found to reproduce the average equilibrium voltage and voltage profiles of various battery materials rather accurately.³⁷ However, hybrid functionals, such as HSE06, are computationally expensive, and the amount of exact exchange required is system dependent.^{205,208} The recently developed SCAN meta-GGA functional can give a better result for lattice parameters, band gaps, electronic structure, and electrochemical properties for layered oxide cathode materials relative to PBE, without using the notorious U parameter since SCAN treats localized states better.^{138,209}

2.3.4. Ion-Diffusion Kinetics and Paths. The time required for a battery to fully charge and the power it can deliver are two important parameters to consider when developing new battery materials. In LIBs, the rate capacity of a material depends on the Li diffusion within electrodes and between electrodes through the electrolyte.^{37,40,100,114,173,210–212} As Li ion transport through a liquid electrolyte is considered to be much faster compared to that in a solid material, diffusion within the electrodes will often be the rate-determining step for Li shuttling between electrodes.²¹²

One of the key quantities while studying diffusion phenomena is the diffusion constant. Though experiments can determine the diffusion coefficient, it is difficult to separate the diffusion rate in solution, in solid, and through the solid–electrolyte interphase (SEI). Additionally, varying sample

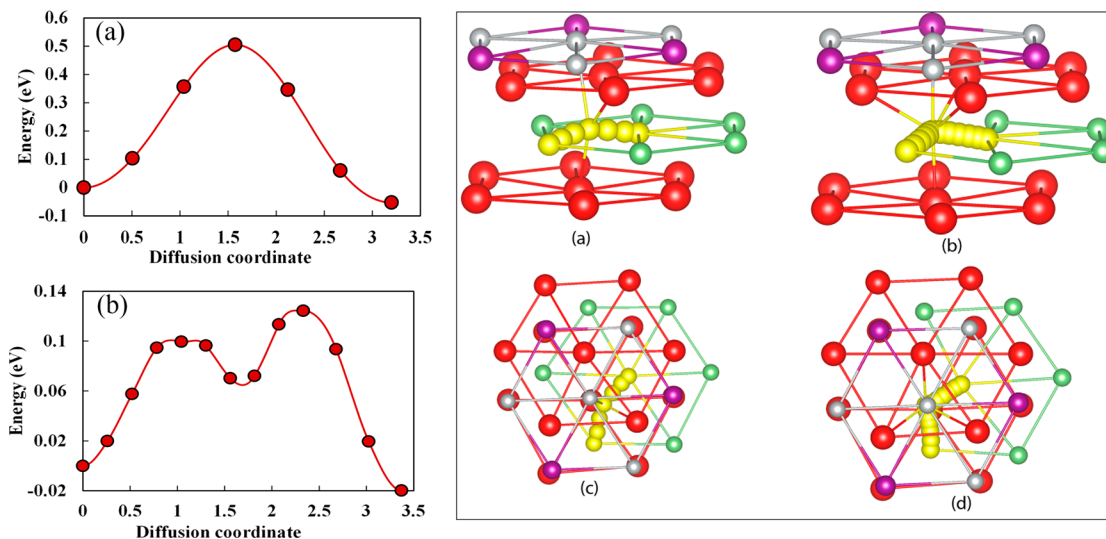


Figure 13. (left panel) Li diffusion barrier profiles for the (a) ODH path and (b) TSH path in $\text{LiNi}_{0.5}\text{Co}_{0.2}\text{Mn}_{0.3}\text{O}_2$. (right panel) Li diffusion paths for fully lithiated $\text{Li}_x\text{Ni}_{0.5}\text{Co}_{0.2}\text{Mn}_{0.3}\text{O}_2$ for the (a) ODH path and (b) TSH path, (c) top view of the ODH path, and (d) top view of the TSH path. Color code for spheres: red, oxygen atoms; green, Li atoms; gray, Ni atoms; and pink, Mn atoms. Yellow spheres indicate NEB images for the Li atoms. Only the Li migration part of the system is shown for clarity, although the calculations were performed on the full 60 formula unit systems. (Reprinted with permission from ref 85. Copyright 2016, published by the PCCP Owner Societies.)

defect concentrations in different experiments can result in different measured diffusion coefficients. Computational studies of diffusion in different types of LIB cathode materials employing classical MD, AIMD simulations, and DFT calculations combined with the NEB technique play a crucial role in our current understanding of the Li-ion diffusion pathways and kinetics, along with experimental data.^{37,100,173}

Diffusion constants of ions in solid-state materials are affected by the electrostatic and steric interactions between the ion and the host, as well as the structure of the host material. By Fick's law, the diffusion constant, D , is related to the change in particle density, ρ , as

$$\frac{\partial \rho}{\partial t} = D \nabla^2 \rho \quad (8)$$

However, this relation is for a macroscopic system. For a microscopic system the diffusion constant can be determined using Einstein's relation,¹⁰⁰ where D is related to the total displacement, $\mathbf{R}(t)$, of the particles as

$$D = \Theta \lim_{2d t \rightarrow \infty} \frac{\left\langle \frac{1}{N} \mathbf{R}(t)^2 \right\rangle}{t} \quad (9)$$

where $\mathbf{R}(t) = \sum_{I=1}^N \mathbf{R}_I(t)$ for an N particle system with individual particle displacement \mathbf{R}_I at time t . Θ is the thermodynamic coefficient, which relates the change in chemical potential of the diffusing particles with their concentration, and d is the ion diffusion dimension. For layered LIB cathode materials, the value of d is 2. In the limit of infinite dilution, where the value of Θ is unity, D can be computed from the mean square displacement (MSD) in the limit $t \rightarrow \infty$,^{100,173}

$$D \approx D_{\text{self}} = \frac{1}{2dt} \sum_{I=1}^N \frac{1}{N} \langle |\mathbf{R}_I(t) - \mathbf{R}_I(0)|^2 \rangle = \frac{\text{MSD}}{2dt} \quad (10)$$

In the above equation, $\mathbf{R}_I(t)$ is the position of particle I at time t , which can be obtained from MD or kinetic MC (KMC) simulations. Here D_{self} is the self-diffusion constant, which is

the diffusion constant in the absence of any external field. In principle, both classical MD and AIMD simulations can be used to determine the diffusion constant in the dilute and nondilute limits (using eqs 8–10). However, in the nondilute cases, where Θ is not unity, AIMD simulations are challenging. This is because the estimation of Θ requires a grand canonical ensemble simulation, as the value of Θ depends on the change in chemical potential with respect to the change in the concentration of the diffusing ion.^{100,115} In order to compute D_{self} using eq 10, it is necessary to generate long trajectories as Li diffusion in layered materials has significant energy barriers, i.e., the diffusion includes rare hopping events. Generating such a long trajectory from AIMD simulation is computationally expensive. In contrast, classical MD or KMC simulations can reach long time scales, but with lower accuracy potentials. Van der Ven et al. studied Li diffusion in the nondilute limit for LiCoO_2 using a combination of first-principles computations and KMC simulations.²¹³ Here, the configuration dependence of diffusion barriers in the nondilute limit was accounted for by employing a local CE approach, and the value of Θ was computed by performing grand canonical ensemble MC simulations.²¹³

In addition to MD and KMC simulations, where the time evolution of the system is analyzed, static computations utilizing calculation of stationary points on the PES, such as DFT, can be used to compute the diffusion coefficient. Here, one assumes diffusion along a predefined reaction path (i.e., reaction coordinate), and the activation barrier along the path is determined. In the case of Li diffusion in LIBs, a hopping mechanism may be considered, where the Li-ion crosses barriers $\gg k_B T$ (k_B is Boltzmann's constant and T is the temperature). Then, by utilizing transition state theory, the rate constant for the diffusion can be evaluated as

$$k(T) = v \exp \left[\frac{-\Delta E^\ddagger}{k_B T} \right] \quad (11)$$

Here, $\Delta E^\ddagger = E_{\text{TS}} - E_{\text{R}}$ is the difference between the energy of the transition state (E_{TS}) and reactant state (E_{R}) and v is a

temperature dependent prefactor. For a hopping process, ΔE^\ddagger is the energy barrier for hopping and v is the hopping frequency. Typically, v takes values between 10^{11} to 10^{13} s^{-1} .¹¹⁵ For a hopping mechanism, the diffusion coefficient can be computed as

$$D(T) = l^2 k(T) \quad (12)$$

where l is the hopping distance between adjacent sites.

One of the widely used approaches to compute the minimum energy pathways for the diffusion process, and hence ΔE^\ddagger , is the NEB method.^{182,214} Here, one has to provide an initial set of geometries called images that connect two states, reactant and product, that are separated by a transition state. Here, the initial set of geometries along the reaction path can be generated by a linear interpolation of the coordinates undergoing maximum change during the conversion of reactant to product. Minimization of the forces on each of these images, which are connected to the neighboring images by springs, yields the minimum energy path (MEP). This is straightforward if only one MEP is present. If multiple MEPs are present, then the NEB algorithm will lead to the nearest MEP. In such cases, methods like simulated annealing can be useful for optimization of the images. The NEB method, in conjunction with DFT, has been widely used to determine the mechanism and the activation barriers for ion diffusion in battery materials.^{37,100,173} It was found that the GGA functional performs better compared to the self-interaction corrected GGA+U functional due to overlocalization of electron density at the nuclei along the Li-diffusion pathway.¹⁰⁰

Computational studies on diffusion have suggested two hopping pathways for Li ions in cathode materials: the oxygen dumbbell hopping (ODH) and the tetrahedral site hopping mechanism (TSH) (Figure 13).^{115,117,213} Along the ODH pathway, Li ions hop to a vacancy site via the shortest path, which crosses an oxygen dumbbell. Here, immediate neighboring sites of the vacancy are occupied by Li ions. Along the TSH route, Li migrates to the vacancy site through a tetrahedral site along a curved path. Here, at least one of the two sites adjacent to the vacancy to which Li hops should be vacant. First-principles studies show that the configuration with a Li ion in the tetrahedral site has a shallow minimum, the deepness of which depends on the number of vacancies in the proximity of the hopping site.^{85,115}

The mechanism and the barrier for the diffusion depend on various factors, such as concentration and arrangement of Li ions, vacancies, and Li-slab spacing.^{115,117,213} It was found that the ODH pathway is favored at high Li concentration, whereas the TSH pathway is preferred at low Li concentration for NCM materials.¹¹⁷ Along the TSH pathway, where Li-ions transport through tetrahedral sites, the barrier was found to be lower for a divacancy mechanism compared to the monovacancy mechanism.^{115,116} Since the number of vacancies decreases with increase in Li concentration, Li migration along this pathway is less likely at high Li concentrations.¹¹⁶ The preference for the divacancy route can be attributed to the absence of repulsion between Li ions in the tetrahedral region and the transition metal ions in the face sharing octahedra, whereas there is Li-TM repulsion along a monovacancy pathway.^{40,85,115,116,215}

We also note that the diffusion coefficient increases with increasing content of Ni in NCMs, and this trend is found both from ab initio MD simulations and experiments, as reported by Wei et al.¹¹⁷ These authors showed that Li diffusion in the

vicinity of Ni^{2+} and Ni^{3+} ions (which are more abundant in Ni-rich NCMs) has a lower activation barrier compared to pathways near Ni^{4+} , Co^{3+} , and Mn^{4+} ions.

2.3.5. Surface Properties. Rate capability, stability, cycling performance, and in some cases even the capacity and energy content of LIBs are significantly affected by the surface structure and surface properties of the cathode materials.^{216–218} Since layered cathode materials used in LIBs are nucleophilic and basic by virtue of the negatively charged oxygen atoms, they undergo surface reactions with electrophilic solution species (e.g., alkyl carbonate solvents, protic contaminants) to form surface films that behave like SEI on the active mass.²¹⁹ These surface films are usually protective and, hence, enhance stability. However, the presence of surface films increases the impedance of the cathodes.²²⁰ Layered LIB cathode materials also undergo surface reconstruction during cycling, such as conversion to spinel and/or rock-salt structure.^{77,87,157,221,222} Migration of the transition metal in the LIB cathode materials to the adjacent Li layer during cycling has been suggested as being partially responsible for this surface reconstruction.^{77,87,157,221,222} Spectroscopic studies by Lin et al. on NCM ($\text{LiNi}_x\text{Co}_{1-2x}\text{Mn}_x\text{O}_2$) indicate that surface reconstruction can also occur due to reaction between electrolyte and cathode.²²³ The surface reconstruction layers thus formed increase the barrier for Li diffusion, which in turn reduces rate capability of the materials.²²⁴ Moreover, surface reconstruction can cause material degradation by extending from the surface to the interior of the material.^{224,225} Development of new synthetic methods, surface doping, and surface coating were found to be successful in improving cycling performance and rate capability by stabilizing the surfaces.^{226,227} Understanding the factors influencing the surface stability of cathode materials is crucial, and theory can contribute significantly to this.

Computational studies provide invaluable thermodynamic and atomistic information regarding the surface structure and reactivity and, along with experiments, can greatly enhance our understanding of SEI formation and reconstruction/degradation processes.^{93,197,224,228–232} In computational studies the stability of the surface may be obtained from the surface energy (γ) for slab models, using the general formula:²³³

$$\gamma = \frac{E_{\text{slab}} - NE_{\text{bulk}}}{2A} \quad (13)$$

Here, E_{slab} is the energy of the slab (neglecting entropic contributions), and E_{bulk} is the energy of the bulk system per formula unit, which is the same formula unit as the slab. Here, the number 2 appearing in the denominator accounts for the two free surfaces in typical three-dimensional slab models. N and A denote the number of formula units in the slab and the area of the slab, respectively. DFT computations, in combination with the NEB approach, have been employed to study the mechanism of SEI formation.^{228–232,234}

Surface reactivity in layered materials plays an important role in the safety and longevity of LIB.^{229,232,234} There are several theoretical studies on the reaction mechanism of electrolyte with basic layered LCO, LNO, and NCM cathode materials, and ring-opening mechanisms for ethylene carbonate (EC) at the cathode surface are found to be dominating.^{231,232,235} Giordano et al. showed from DFT+U calculations that there are four different mechanistic routes, such as nucleophilic attack, electrophilic attack, and dissociation with and without formation of oxygen vacancies when EC is reacting at the

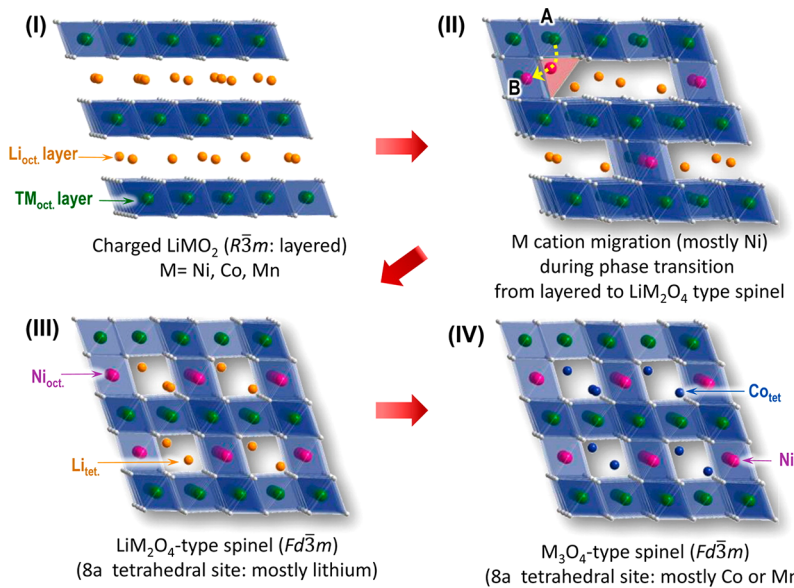


Figure 14. Schematic illustration of the phase transition and the possible TM cation migration path in charged NCM cathode materials during thermal decomposition. (Reprinted with permission from ref 239. Copyright 2014, The American Chemical Society.)

layered oxide surface.²³⁰ Further, in a recent study²³² on the reactivity of the EC at the LiMO_2 surface ($\text{M} = \text{Ni, Co, Mn}$), it was shown that oxygen sites are more reactive toward electrolyte oxidation reactions. These authors calculated the reaction energies and kinetic barriers using the climbing image NEB method and showed that the energy of hydrogen absorption relates to the distance between the Fermi and the O 2p levels. The key surface reaction steps in the EC ring opening process in NCM cathode materials were presented by Xu et al. using DFT+U.²³¹

Segregation of TMs at the surface for Ni-rich NCM/NCA is seemingly a general phenomenon. Liang et al. showed that if $x < 0.1$ in $\text{LiNi}_{1-2x}\text{Co}_x\text{Mn}_x\text{O}_2$, i.e., Ni-rich NCMs, Co and Mn, which are in the local environment of Ni, segregate at the surface.¹⁵⁷ They proposed a bond model for the calculation of bond strength between two transition metal ions in NCMs to explain the atom segregation at the surface of Ni-rich NCMs.

2.3.6. Material Stability and Phase Transition. During delithiation of layered cathode materials (LiMO_2 , $R\bar{3}m$), TM atoms rearrange due to the presence of Li or oxygen vacancies and the structure may transform to a different phase, such as spinel or spinel-like (LiM_2O_4 , $Fd\bar{3}m$), rock-salt (MO , $Fm\bar{3}m$), or monoclinic phase (LiMO_2 , $C2/m$) (Figure 14).^{40,236–238}

From a computational perspective, one can investigate phase transformation by calculating the free energy of the different phases as a function of the Li concentration (Figure 15).^{240,241} Ceder, Van der Ven, and co-workers showed that the free energy (F) can be calculated using a combined approach of first-principles calculations and statistical mechanics:^{240,241}

$$F = -k_{\text{B}}T \ln(Z) \quad (14)$$

The ground state free energy and the difference in free energy between different phases can be obtained from first-principles and used to estimate the partition function (Z).

In this phase transformation, TM atoms move to interstitial octahedral positions in LiMO_2 and Li atoms move to either an octahedra or tetrahedra interstitial position to form a spinel LiM_2O_4 phase. In general, TMs and Li ions occupy the interstitial sites along the (111) planes in the layered $R\bar{3}m$

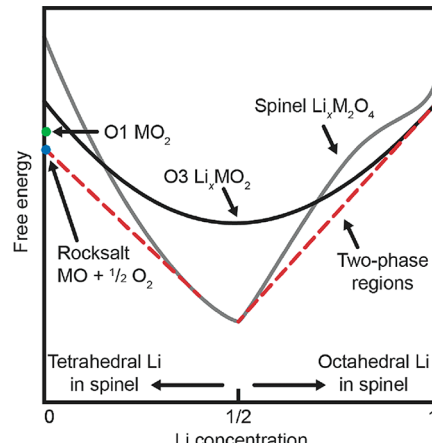


Figure 15. Schematic free energy curves for layered and spinel $\text{Li}_x\text{M}_2\text{O}_4$. (Reprinted with permission from ref 40. Copyright 2017, Wiley-VCH.)

structure, while the positions of the O-ions remain unchanged. For example, in the case of Li_xMnO_2 , Mn atoms move from the $\text{Mn}(111)$ plane to the $\text{Li}(111)$ plane.^{236,242} In situ X-ray diffraction studies by Reimers and Dahn showed that there is a phase transition from hexagonal to monoclinic symmetry in LiCoO_2 upon delithiation,²⁴³ and Van der Ven et al. subsequently showed the same transition from theoretical calculations.²⁴⁰ Layered LiNiO_2 $R\bar{3}m$ structure transforms to the monoclinic $C2/m$ phase upon cycling, as Ni ions readily occupy Li layers.^{58,244}

Beyond these basic homocationic layered materials, binary and ternary layered oxides, such as $\text{LiNi}_{1/2}\text{Mn}_{1/2}\text{O}_2$, NCM, or NCA, suffer from similar capacity fading due to phase transitions.^{239,245} In the case of binary oxides, the layered material transforms from layered to spinel due to the presence of Jahn-Teller distortion centers (e.g., Mn and Ni).²⁴⁵ In the case of NCM, the thermal stability decreases with increasing contents of Ni ions (Figure 16). In NCM, Ni ions are present in different oxidation states, and these ions affect the material's stability to different degrees: Ni^{4+} ions are highly oxidizing, and

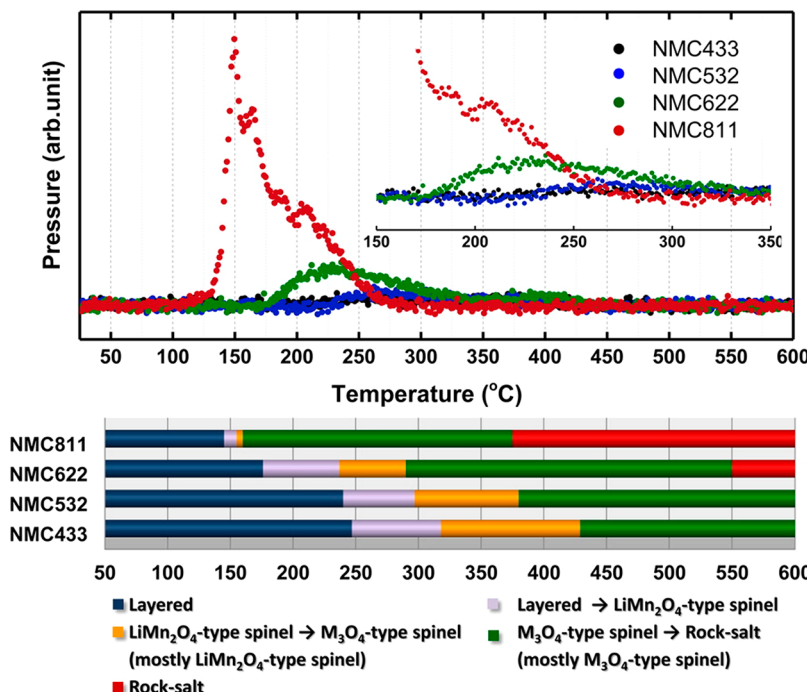
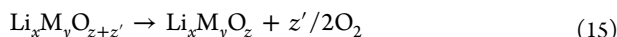


Figure 16. Mass spectroscopy profiles for oxygen (O_2 , $m/z = 32$) collected simultaneously during measurement of TR-XRD and the corresponding temperature region of the phase transitions for NCM samples (lower panel). (Reprinted with permission from ref 239. Copyright 2014, The American Chemical Society.)

it is therefore beneficial to reduce the number of ions in this oxidation state.⁸⁶ On the other hand, Ni^{2+} and Li^+ ions have similar ionic radii, making Ni^{2+} prone to cation mixing with Li^+ .⁵⁰

As mentioned above, during delithiation of layered $R\bar{3}m$ cathode materials, TM atoms rearrange due to the presence of Li or oxygen vacancies, and the structure may transform to a different phase, such as spinel, rock-salt, or monoclinic phase. There is direct correlation between such phase transitions and oxygen release in the case of LIBs, and these are also associated with material safety.²²⁷ During cycling, structural changes occur, and oxygen is released from the system and may react with electrolyte carbonic components, thus damaging the cell. In general, greater Ni content in NCMs results in greater oxygen release.²⁴⁶ Wang et al. explained the thermal stability of oxide cathode materials calculating the Gibbs free energy for the release of oxygen.²⁴⁷ The general reaction for the oxygen release from the layered cathode material was estimated as follows.



If the entropy change due to oxygen release is ΔS then the change in Gibbs free energy is²⁴⁷

$$\begin{aligned} \Delta G = \Delta H - T\Delta S &\approx -E^\circ(\text{Li}_x \text{M}_y \text{O}_{z+z'}) + E^\circ(\text{Li}_x \text{M}_y \text{O}_z) \\ &+ z'/2 \cdot E(\text{O}_2) - T\Delta S \end{aligned} \quad (16)$$

Using this free energy at different Li concentrations, one can construct the phase diagram.

It is important to note that the oxygen release due to the change in structure during delithiation occurs only at a high temperature (600 °C) in some NCMs with low nickel contents (up to 50%), and these are considered safe cathode alternatives. In Ni-rich NCM622 or NCM811, oxygen release occurs at lower temperatures (at 550 and 365 °C,

respectively), hence affecting stability, as well as the safety of the system.²³⁹

The thermal stability problem discussed above may be ascribed to Li/Ni cation mixing, which is most pronounced for Ni-rich NCMs. There are additional factors that can promote oxygen release, as discussed by Zheng et al.²⁴⁸ These authors employed PBE+U computations combined with experiments to show that the thermal stability of NCMs depends strongly on the presence of unstable oxygen, which in turn depends on the local oxygen coordination environment. It was proposed that oxygen release from unstable sites can be avoided by controlling the Li content, oxidation state of Ni ions (i.e., presence of Ni^{2+} and Ni^{3+}), content of Ni, Co, and Mn, and Li/Ni mixing. Oxygen vacancy formation energy calculations suggested that NCMs with equal proportions of Ni and Mn are more thermally stable than Ni-rich NCMs.

In a recent report by Li et al., it was shown from in situ XRD and DFT calculations that lattice collapse resulting in capacity fading during cycling in NCMs occurs at a deep charge limit irrespective of Ni content, and it depends on Li utilization.²⁴⁹

Recently, it was shown that oxygen loss in layered materials is a two-step process in the case of NCA801505 layered cathode materials.²⁵⁰ In the first step loss of oxygen is very fast, forming an amorphized rock-salt structure in the layered cathode surface, and in the subsequent step loss of oxygen slows down by the formation of crystalline rock-salt at the subsurface.²⁵⁰

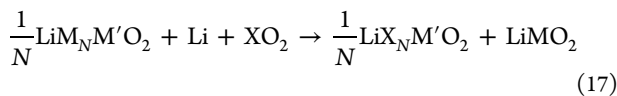
Doping with high-valent metal ions can improve the stability in layered materials, as it increases the number of Ni^{2+} ions, while decreasing the number of Ni^{3+} and Ni^{4+} ions, as a result of charge compensation.⁸⁷ We will discuss the advantages of doping in greater detail below.

2.3.7. Doping in Layered Cathode Materials. Lattice doping is an effective strategy to enhance the structural stability and electrochemical properties in cathode materi-

als.^{87,94} An assortment of studies of the effect of doping on NCM and NCA materials have shown that this is a promising strategy to improve properties, such as capacity, capacity retention, and kinetics. For example, doping with elements such as Fe,²⁵¹ Cr,²⁵² Mg,^{252–254} Al,^{252,255–257} Nb,²⁵⁸ Zr,^{87,259} Sn,²⁶⁰ Zn,⁹³ W,²⁶¹ Mo,²⁶² and rare earth elements, such as La, Ce, and Pr,²⁶² was explored for various NCM-cathode materials. Yoshida et al. further showed that Nb doping in LNO is preferable over other dopant such as B, Mo, Os, Bi, and Tc through high throughput screening using DFT with optB86b-vdW-XC.¹⁹⁶ A recent computational study by Kim on Zr-doped LNO showed that the Li-ion diffusion barrier along the (012) surface plane is lower than that along the (003) surface plane.²⁶³ The doping concentration of Zr is higher near the (012) surface compared to the (003) surface plane, and it decreases with distance from the surface for (012). This work also showed that Zr doping in LNO suppresses oxygen release because of enhanced covalent and electrostatic interaction of TMs with O ions. Using first-principles DFT calculations, Dixit et al. suggested that the oxidation state of Ni ions is central to both the electrochemical activity and the stability of NCMs, and the Ni²⁺ oxidation state is desirable due to ionic Ni–O interactions and availability of redox-active electrons.^{85–87} On the other hand, Ni⁴⁺ is undesirable as it leads to Ni–O covalency, as it tends to reduce to Ni²⁺. Based on these findings, they suggested a high-valent cation doping strategy, which can be employed to reduce the oxidation state of Ni ions (in Ni-rich materials) through charge compensation.

These doped systems can be handled by first-principles supercell approaches by replacing a TM or Li with the dopant. A challenge arises when dealing with a very low doping concentration, as there is a need to employ very large supercells, and these calculations can be very expensive. Finite-sized supercell errors can result from interactions between impurities (i.e., dopants) and their periodic images. Correction schemes to alleviate this error have been proposed by several researchers.^{264,265}

To determine an optimal dopant for a particular material it is vital to have an atomistic understanding of the effect of dopant on the host material. Computational studies have been employed to understand the effect of doping on structural and electrochemical properties of NCM materials.⁸⁷ In computations, the optimal dopant sites may be determined by comparing different substitution energies, E_{Sub} . For example, a substitution reaction that dopes an element X at the M site of LiMM' O₂ may be written as



and the corresponding substitution energy, E_{Sub} , is given by

$$E_{\text{Sub}} = \frac{1}{N} [(E_{\text{LiX}_N \text{M}' \text{O}_2} + N \cdot E_{\text{LiMO}_2}) - (E_{\text{LiM}_N \text{M}' \text{O}_2} + N \cdot E_{\text{Li}} + N \cdot E_{\text{XO}_2})] \quad (18)$$

where $E_{\text{LiX}_N \text{M}' \text{O}_2}$ and $E_{\text{LiM}_N \text{M}' \text{O}_2}$ are the total energies of the doped and undoped materials, respectively, E_{LiMO_2} and E_{XO_2} are the total energies of the lithiated material and the oxide of the dopant metal, respectively, E_{Li} the energy of Li, and N is a constant to maintain the stoichiometry. Once the optimal dopant sites have been obtained from the substitution energy computations, the electrochemical properties of the doped

material can be studied in the same way as those for the pristine material. In general, this approach has been used for different dopants in different NCM materials.⁸⁷ In the above description, the ground state lithiated oxide, LiMO₂, is taken as the reference for the TM removed on doping.

2.3.8. Studies Using Nuclear Magnetic Resonance (NMR) Spectroscopy. **2.3.8.1. Chemical Shifts.** Solid-state NMR has been used extensively to investigate cathode materials for LIBs.^{185,186,266–269} Theoretically, one may compute the chemical shielding tensors and electric field gradient for layered cathode and anode materials using DFT approaches.^{270,271} These calculations rely on theoretical advances, such as the GIPAW (Gauge Including Projector Augmented Wave) method,²⁷² which is implemented in the VASP^{152–154} and WIEN2k²⁷³ codes, making it possible to calculate the NMR chemical shifts and electric field gradients in periodic systems.^{272,274,275} Recently, large-scale paramagnetic NMR on extended solids was reported using the computationally efficient Gaussian augmented plane-wave method implemented in the CP2K code.²⁷⁶ First-principles GIPAW calculations can yield the absolute chemical shielding tensors for each nucleus, $\hat{\sigma}(R)$, and the chemical shielding tensor $\hat{\sigma}$ determines the total magnetic field at the atomic nucleus,

$$\mathbf{B} = (1 - \hat{\sigma}) \mathbf{B}_{\text{ext}} \quad (19)$$

where \mathbf{B}_{ext} is the external magnetic field. The isotropic chemical shielding $\sigma_{\text{iso}} = \frac{1}{3} \text{Tr}[\sigma_x + \sigma_y + \sigma_z] = \frac{1}{3} \text{Tr}[\sigma]$ is compared to the experimental isotropic chemical shifts by using

$$\delta_{\text{iso}} = \sigma_{\text{ref}} - \sigma_{\text{iso}} \quad (20)$$

where σ_{ref} is the isotropic chemical shielding for a reference material.

2.3.8.2. Electric Field Gradients (EFGs). A nucleus will be NMR active or inactive, depending on the nuclear spin, I . If a nucleus has spin quantum number $I > 1/2$, it has an electrical quadrupole moment, Q , due to the nonspherical distribution of charge in the nucleus. Therefore, NMR spectra are additionally broadened by quadrupolar interactions, i.e., interactions with the electric field gradient (EFG) at the nucleus. This is termed the nuclear quadrupole interaction (NQI), and the NQI affects both the line shape and line intensity. Due to these effects, it can be difficult to interpret NMR spectra, and theory can be a valuable tool to estimate the contribution of quadrupolar interactions.²⁷⁷

When the magnitude of the quadrupolar interaction is nonzero, the NMR line shape of a quadrupolar nucleus possesses characteristic features and broadening, which impact the NMR line width. The total isotropic shift is the sum of two isotropic components and can be written as

$$\delta_{\text{tot}} = \delta_{\text{iso}}^{(\text{CS})} + \delta_{\text{iso}}^{(2Q)} \quad (21)$$

where the first term is the isotropic chemical shift (CS) and the second term is the isotropic second-order quadrupolar shift. For a nucleus with spin I , the isotropic quadrupolar shift (in ppm) of the central transition can be obtained using the below expression:

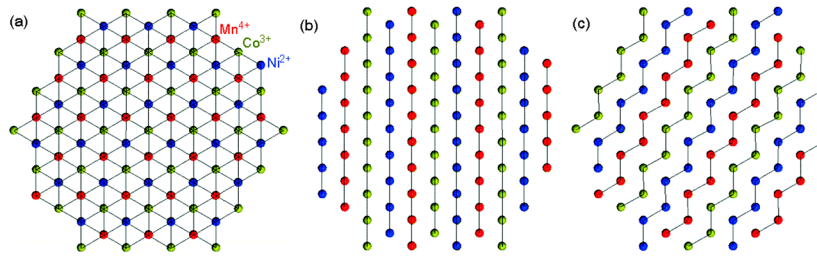


Figure 17. Schematic illustrations of the three ordered models proposed in the text for one TM layer in $\text{Li}[\text{Ni}_{1/3}\text{Mn}_{1/3}\text{Co}_{1/3}] \text{O}_2$: (a) $[\sqrt{3} \times \sqrt{3}]$ $\text{R}30^\circ$ -type superlattice, (b) parallel, and (c) zigzag arrangements. (Reprinted with permission from ref 186. Copyright 2007, The American Chemical Society.)

$$\delta_{\text{iso}}^{(2Q)} = -\frac{3}{40} \left(\frac{C_q}{\omega}\right)^2 \left(\frac{I(I+1) - \frac{3}{4}}{I^2(2I-1)^2}\right) \left(1 + \frac{\eta^2}{3}\right) \times 10^6 \quad (22)$$

where ω is the Larmor frequency of the nucleus, C_q is the quadrupole coupling constant, and η is the quadrupolar asymmetry parameter.

To provide additional insights into NMR spectra, the Bader charge approach may be helpful, as one can readily distinguish between the shielded and deshielded atoms and, hence, aid in assigning the NMR peaks.

3. THEORETICAL STUDIES OF LAYERED NCM AND NCA MATERIALS

In this section, we discuss reported calculations of a wide range of properties for NCM and NCA materials using the methods described in the previous section.

3.1. NCM Materials. NCM materials are generally found as layered structures, with $\text{R}\bar{3}m$ symmetry, as mentioned above. In these layered structures, a multitude of Ni, Co, and Mn configurations that influence material properties are possible. In this section, we first elaborate on the most common NCMs, such as NCM333, NCM523, NCM622, and NCM811, followed by a discussion of other available NCMs, like NCM424, NCM71515, and NCM, with more than 80% Ni.

3.1.1. NCM333. $\text{Li}[\text{Ni}_{1/3}\text{Co}_{1/3}\text{Mn}_{1/3}] \text{O}_2$ (NCM333) was reported in the literature in 2001 by Ohzuku and Makimura.⁷¹ This is a widely studied LIB cathode material that has been commercialized,²⁰ due to its high capacity and good thermal and structural stability.^{50,72,78} Indeed, among various $\text{LiNi}_{1-x-y}\text{Co}_x\text{Mn}_y\text{O}_2$, NCM333 was found to possess superior capacity retention, thermal stability, and structural stability.^{50,72,76} These favorable properties are attributed to the combination of Ni (capacity), Co (kinetics), and Mn (stability),^{50,72,76} and low Ni content prevents cation disorder²⁷⁸ and oxygen release.^{50,239,279} Indeed, capacity retention, along with stable cycling, was found to be possible at voltages up to 4.4 V for NCM333.⁷⁶ However, low Ni content also results in low initial discharge capacity and electronic conductivity for this material compared to other layered TM oxides (e.g., Ni-rich materials).^{50,72} The rechargeable capacity of this material was found to be 200 mAh g⁻¹ in a voltage window of 3.5–5.0 V.⁷¹

3.1.1.1. NCM333 Structure. NCM333 has a distorted rock-salt or $\alpha\text{-NaFeO}_2$ structure (space group: $\text{R}\bar{3}m$).^{71,156,278,280,40,184} Computational studies by Koyama et al.¹⁸⁴ using the local spin density approximation (LSDA) approach and electron diffraction experiments by Yabuuchi et al. indicated that the TM layers consist of a $[\sqrt{3} \times \sqrt{3}]$ $\text{R}30^\circ$

superlattice structure.^{184,281,282} First-principles studies by Karino using the Hartree–Fock–Slater based discrete variational– $X\alpha$ method also suggested the $[\sqrt{3} \times \sqrt{3}]$ $\text{R}30^\circ$ superlattice structure.²⁸² Li NMR studies^{185,186} and a combination of Li NMR and simulated annealing computations²⁸³ also suggest the presence of such a $\sqrt{3}$ TM ordering. In particular, pioneering detailed studies on the local environment and cation ordering in NCM333 using Li-solid-state NMR were presented by the groups of Goward and Grey (see Figure 17).^{185,186,283} Goward and co-workers brought the first experimental evidence for local TM $\sqrt{3}$ -ordering using ⁶Li NMR and showed a correlation between the degree of cation disorder and the magnitude of the chemical shift.¹⁶⁹ No calculations were performed in this work. A subsequent study by Grey and co-workers showed, using a combination of ⁶Li NMR measurements, neutron pair distribution function analysis, and reverse MC calculations, that NCM333 has nonrandom distribution of Ni/Mn cations in the TM layers. Here, Ni ions were found to be closer to Mn cations, forming a $[\sqrt{3} \times \sqrt{3}]$ $\text{R}30^\circ$ structure.¹⁸⁶ Goward and co-workers also showed in a more recent study²⁸³ from a combined approach of ⁷Li NMR measurement and simulated annealing MC that there is a tendency to form Ni–Mn clusters in otherwise heavily disordered NCM333 and related structures. In this work, the concept of regional electric charge neutrality in the system was assumed, and considering that this is a generic property, the method is expected to be widely applicable.

X-ray diffraction studies by Yang et al. indicated that the a and c lattice parameters for this material are 2.8653 and 14.2608 Å, respectively,²⁸⁴ and Zhang et al. also reported similar values for a and c lattice parameters (2.866 and 14.26 Å for a and c , respectively).²⁸⁵ DFT computations with the LSDA approach underestimated the lattice parameters,¹⁸⁴ whereas computations employing a GGA functional^{156,286,287} and the HSE06 hybrid functional²⁸⁸ produced lattice constants close to the experimental values (see Table 3). From Table 3, we see that the c lattice parameter obtained using the PBE

Table 3. a and c Lattice Parameters (Å) for NCM333 Using Different Levels of Theory

level of theory	a	c	ref
LSDA with ultrasoft pseudopotentials	2.831	13.88	ref 184
PBE with PAW	2.897	14.154	ref 286
GGA with ultrasoft pseudopotentials	2.892	14.251	ref 156
PBE with ultrasoft GBRV-type pseudopotentials	2.883	14.232	ref 287
HSE06 with PAW	2.85	14.23	ref 288
experiment	2.8653	14.2608	ref 284

functional in combination with GBRV-type ultrasoft pseudo-potentials²⁸⁹ is comparable with that obtained using the HSE06 hybrid functional.²⁹⁰ GGA¹⁵⁶ and LSDA¹⁸⁴ studies also showed that the lattice parameter a decreases with decrease in Li concentration until half-lithiation and then increases with further decrease in Li concentration, whereas the c lattice parameter was found to follow an opposite trend. This is also in agreement with the combined experimental and PBE+ U studies by Markus et al.²⁰⁴ and X-ray and neutron diffraction studies by Yin et al.²⁹¹

3.1.1.2. NCM333 Electronic Structure. LSDA,¹⁸⁴ GGA,^{156,190} and GGA+ U ^{157,204} functionals have been employed by different groups to probe the electronic structure of NCM333. The main characteristics of the electronic structure, as reflected in the DOS, were found to be the same irrespective of the DFT functional used. Analysis of the distance between various transition metal ions and electronic structure using LSDA¹⁸⁴ and GGA calculations^{156,190} indicates that the oxidation states of the TM ions are 2+, 3+, and 4+ for Ni, Co, and Mn, respectively, for the pristine material. Electronic structure calculations employing the PW91+ U functional also support this.²⁹² The above-mentioned DFT studies employing both LSDA¹⁸⁴ and GGA¹⁵⁶ show that, as the Li concentration decreases, Ni ions adopt the 3+ and 4+ oxidation states and Co is found in a 4+ oxidation state, whereas the oxidation state of Mn is unchanged. This is also in agreement with the combined experimental and PBE+ U studies by Markus et al.²⁰⁴ and X-ray absorption spectroscopy studies by Yoon et al.²⁹³ The total moment of each TM, obtained by integrating the GGA spin density in the valence states, indicates that Ni is in a high spin (HS) state for the 2+ oxidation state, whereas Ni in 3+ and 4+ is in a low spin (LS) state.¹⁵⁶ Co(+3) was found to exist in an LS state, whereas Mn(+4) was found to be in an HS state.^{40,156} GGA based computations indicate that the spin arrangement for the minimum energy structure of NCM333 is antiferromagnetic.¹⁵⁶ Analysis of the DOS obtained from both LSDA¹⁸⁴ and GGA computations¹⁵⁶ for various Li concentrations indicates that the band gap decreases with a decrease in Li concentration. The Fermi level of NCM333 was found to consist of Ni e_g states and the conduction band consists of Mn t_{2g} states using either LSDA or GGA.^{156,184} It was also observed that the overlap between 2p oxygen orbitals and the TM d orbitals increased with decreasing Li concentration.¹⁵⁶

3.1.1.3. NCM333 Voltage Profile. NCM333 was found to have initial discharge capacities of 150 mAh g⁻¹ and 220 mAh g⁻¹ in the voltage windows 2.5–4.2 V and 2.5–5.0 V, respectively, with a 0.17 mA cm⁻² current density. The rechargeable capacities were 150 mAh g⁻¹ and 200 mAh g⁻¹ in the voltage windows 3.5–4.2 V and 3.5–5.0 V, respectively, with the same current density.⁷¹ Noh et al. reported an initial discharge capacity of 163 mAh g⁻¹ in the 3.0–4.3 V range with 0.1C current in NCM333.⁷² Capacity fading was observed for this material when cycled above 4.4 V, and this can be ascribed to oxygen release from the surface of the material at high voltages.⁷⁶ Electrochemical studies by Zhao et al. on NCM333 indicated that an increase in cation mixing between Li and Ni can result in reduced rate capacity and discharge capacity.²⁸⁶ This is also in agreement with the higher specific capacity and initial discharge capacity of carbon coated NCM333 compared to uncoated NCM333, as carbon coating reduces cation exchange.²⁸⁵ DFT studies of Koyama et al. employing the LSDA approach,¹⁸⁴ and GGA studies by Hwang et al.¹⁵⁶

showed that the average voltages for three Li-concentration (x) ranges, $1 \geq x \geq 2/3$, $2/3 \geq x \geq 1/3$, and $1/3 \geq x \geq 0$, are in good agreement with experiments.^{284,294} In the former two concentration ranges, i.e., $1 \geq x \geq 1/3$, the redox couples involved are Ni²⁺/Ni³⁺ and Ni³⁺/Ni⁴⁺, respectively, whereas for the $1/3 \geq x \geq 0$ range, the redox couple is Co³⁺/Co⁴⁺.^{156,184,284,294}

Markus et al.²⁰⁴ studied the voltage profile of NCM333 using GGA and GGA+ U in order to optimize U values adopted from those of the lithiated single metal oxide. The authors noted that the lithium intercalation voltage for pure GGA was found to be underestimated by ca. 1 V. These authors fine-tuned the U parameters to match the experimental voltage profile but noted that this yields incorrect redox behavior, i.e., Co oxidizes before Ni.

3.1.1.4. Ion Diffusion in NCM333. As discussed above in Section 2.3.4, Li ions can diffuse via ODH and TSH pathways. Generally, Li ions are presumed to migrate via ODH paths in the early stages of delithiation, while TSH dominates as the delithiation process progresses. Specifically, the ODH pathway is preferred when there is a local monovacancy, while TSH is dominant when there is di- or higher vacancies.

Li diffusion along various paths, via mono- or divacancy mechanisms, was studied by Hoang and Johannes using the HSE06 functional in combination with the NEB method. Li diffusion is expected to follow the monovacancy mechanism in the fully lithiated limit, due to the low concentration of the vacancies, whereas upon extensive delithiation the divacancy mechanism is preferred.^{117,295} The activation barriers using HSE06 for the Li migration were found to be 0.64–0.75 eV and 0.26–0.28 eV for the mono- and divacancy mechanisms, respectively.²⁸⁸ PBE computations in combination with neutron diffraction and electrochemical kinetic experiments by Zhao et al. indicated that Li diffusion barriers increase with greater cation exchange,²⁸⁶ and this increase can be attributed to a decrease in interslab spacing due to cation exchange.^{118,286,296}

3.1.1.5. NCM333 Surface Studies. Structural layered to rock-salt phase transformation of the surface region during cycling of NCM333 was found in EELS and scanning transmission electron microscopy (STEM) studies by Liu et al.²⁹⁷ It was found that the poor electron and ion conducting nature of the rock-salt structure affects the capacity of the material.²⁹⁷ Atom probe tomography and transmission electron microscopy (TEM) studies of Lee et al. identified the presence of a spinel structure, which could be a transformation bridge between the layered and rock-salt structures.^{298,299} According to this study, Ni migration from the transition metal layer to vacant sites in the Li layer, with a concomitant Ni migration from the bulk to the surface, is responsible for the layered to spinel or rock-salt transformation near the surface. PBE+ U computations performed by the same authors, combined with the NEB approach, showed that Ni migrates from the octahedral TM site of the transition metal layer to the octahedral sites of the Li layer along a tetrahedral site (i.e., TSH mechanism). Subsequently, Ni migrates from the material bulk to the surface by hopping between octahedral Li sites.²⁹⁸ Garcia et al. analyzed the stability of various low index polar and nonpolar surfaces of NCM333 by comparing the surface energies computed using PBE+ U , as well as the HSE06 level of theory.³⁰⁰ This study identified the nonpolar (104) and the polar (012), (001), and (110) surfaces as the most stable ones. In this study, the Co³⁺ ion of the (104)

surface was identified to be in its HS configuration, in contrast to its LS configuration in the bulk material. The stabilization of the surface due to this high spin configuration of Co at the (104) surface can lead to Co segregation on this particular surface. Oxygen vacancy creation on the polar (012) surface was found to be more likely than at the nonpolar (104) surface. This suggests that the (012) surface is more reactive than the (104) surface toward oxidation reactions, such as electrolyte decomposition.³⁰⁰

3.1.1.6. Surface Coating and Lattice Doping Studies of NCM333. Surface coating and doping of NCM333 were found to improve the electrochemical performance of this material.^{50,257,258,260,262} Coating with materials such as carbon,²⁸⁴ metal oxides and fluorides (e.g., Al_2O_3 ,³⁰¹ ZrO_2 ,³⁰² TiO_2 ,³⁰³ Li_2TiO_3 ,³⁰⁴ CeO_2 ,³⁰⁵ and AlF_3 ,³⁰⁶)³⁰⁷ and phosphates such as AlPO_4 ³⁰⁷ and $\text{LiTi}_2(\text{PO}_4)_3$ ²⁸⁵ has been successfully employed by various groups to improve the electrochemical properties of NCM333. Conductive additives such as graphene, which can reduce the charge transfer resistance, were also reported to improve electrochemical properties for this material.³⁰⁸

Doping with elements such as Sn,²⁶⁰ Zn,³⁰⁹ Al,²⁵⁷ and Nb²⁵⁸ and rare earth elements such as La, Ce, and Pr²⁶² was found to improve the electrochemical properties of NCM333. Lee and Park reported atomistic simulations using empirical force fields, along with a classical core–shell (polarization) model, targeting the effect of dopants on NCM333. These studies indicated that doping with ions such as Na^+ , K^+ , and Ga^{3+} , which are isovalent with Li^+ and Co^{3+} , is energetically favorable.⁹⁷

3.1.2. NCM523. NCM523 was reported in the literature in 1999 by Z. Liu et al.³¹⁰ and is a promising material as it maintains a useful balance between capacity (50% Ni), rate (20% Co) and stability (30% Mn). Yet, capacity fading remains a problem. In general, NCM523 provides a specific capacity of 217 mAh g⁻¹ in a voltage range of 3.0–4.4 V.⁷⁹

3.1.2.1. NCM523 Structure. Dixit et al. used GGA-based computations to show that the metal ions in the layered $R\bar{3}m$ structure prefer a $(\sqrt{3} \times \sqrt{3})$ $R30^\circ$ arrangement in the TM-layer, and this type of ordering is significantly more stable than linear or random TM ordering.⁸⁵ On delithiation, the *c* lattice parameter initially increases followed by contraction, which is typical for layered materials. It was found that dispersion corrections to the PBE functional were necessary in order to reproduce this *c* lattice parameter trend.⁸⁵ Breuer et al. reported the lattice parameters for NCM523 from a combined experimental and theoretical approach.⁷⁸ In their theoretical study, which used PBE+U+D3, the calculated lattice parameters are *a* = 2.870 Å (2.870 Å from experiment) and *c* = 14.215 Å (14.230 Å from experiment).

3.1.2.2. NCM523 Electronic Structure. NCM523 is a small gap insulator as shown, with greater metallic character than NCM333 due to the increased Ni content.^{72,190} DFT calculations using the GGA and GGA+U approximations suggested that Ni ions are electrochemically more active than Co and Mn, with d states appearing near the Fermi energy.^{85,86,190} Further, Ni ions were shown to exist in different oxidation states, such as 2+, 3+, and 4+. In NCM523, the amount of Ni^{2+} is reduced compared to NCM333, hence reducing the probability for cation mixing between Ni and Li.⁸⁵ From analyses of the DOS and the electronic structure of NCM523, it is clear that Ni^{2+} is in a HS state, whereas Ni^{3+} is in a LS state. Co^{3+} and Mn^{4+} are in LS and HS states, respectively.⁸⁵

3.1.2.3. NCM523 Voltage Profile. The charge and discharge capacities of NCM523 were reported to be 217.6 mAh g⁻¹ and 189.2 mAh g⁻¹ in the voltage range 3.0–4.4 V (30 °C), respectively, during the first cycle.⁷⁹ Breuer et al. recently reported an initial discharge capacity of 160 mAh g⁻¹ for NCM523 at 4.3 V with a C/3 rate.⁷⁸ Jung et al. showed that the initial discharge capacity is 150 mAh g⁻¹ in a 3.0–4.3 V window, with 95% capacity retention after 50 cycles. However, the capacity retention decreases to 61% in a voltage range of 3.0–4.8 V, though the initial discharge capacity increases to 200 mAh g⁻¹.⁷⁷ Noh et al. measured an initial discharge capacity of 175 mAh g⁻¹ in a 3.0–4.3 V range with 0.1C current in NCM523.⁷² Computations reproduce the voltage profiles well using the PBE functional, although the absolute values are predicted to be too low (by ~1 eV), and hence a rigid shift approach was used.⁸⁵ It was demonstrated that the GGA+U method (with the average *U* values adopted from the literature for metals with different oxidation states) did not accurately predict the voltage profile, although the absolute values are closer to experiment than pure PBE.⁸⁵ Ni ions were found to be the main redox active ions in NCM523.⁸⁵ Wei et al.¹¹⁷ and Dixit et al.⁸⁵ showed that $\text{Ni}^{2+}/\text{Ni}^{3+}$ is the redox couple for the pristine system, i.e., in the intercalation range $1 \geq x \geq 3/4$. Further, $\text{Ni}^{2+}/\text{Ni}^{3+}$ and $\text{Ni}^{3+}/\text{Ni}^{4+}$ are redox active in the range $3/4 \geq x \geq 1/2$. All Ni^{2+} are oxidized beyond the limit $1/4 \geq x$, where $\text{Ni}^{3+}/\text{Ni}^{4+}$ is the main redox pair, together with $\text{Co}^{3+}/\text{Co}^{4+}$, in the high voltage range.^{85,117}

3.1.2.4. Ion Diffusion in NCM523. Dixit et al. studied Li diffusion in NCM523 along both ODH and TSH pathways employing the PBE functional in combination with the NEB method.⁸⁵ According to this study, the diffusion barriers of the ODH and TSH pathways are 0.5 and 0.12 eV, respectively. These authors also noted that the Li diffusion barriers obtained for NCM523 are lower than for LiCoO_2 . This difference was suggested to be due to the weaker $\text{Li}^+/\text{Ni}^{2+}$ repulsive interactions in NCM523 relative to $\text{Li}^+/\text{Co}^{3+}$ interactions in LiCoO_2 , as well as the higher *c* lattice parameter in NCM523 than in LiCoO_2 . The calculated diffusion rates for the ODH and TSH pathways in NCM523 were $3.6 \times 10^{-11} \text{ cm}^2 \text{ s}^{-1}$ and $8.6 \times 10^{-5} \text{ cm}^2 \text{ s}^{-1}$, respectively, for fully lithiated states.⁸⁵ The NCM523 Li-ion diffusion rates reported from experiments are $1.55 \times 10^{-12} \text{ cm}^2 \text{ s}^{-1}$ ³¹¹ and $4.64 \times 10^{-11} \text{ cm}^2 \text{ s}^{-1}$.³¹² Thus, the experimental value agrees with the one computed for the ODH pathway, suggesting that the ODH pathway is rate limiting, although the TSH pathway is also likely populated.⁸⁵ Wei et al. reported similar findings for ODH and TSH pathways for Li-ion diffusion in NCM523 from a combined theoretical and experimental approach, and the experimental diffusion rate was found to be around $4 \times 10^{-11} \text{ cm}^2 \text{ s}^{-1}$.¹¹⁷

3.1.2.5. NCM523 Surface Studies. The lattice structure of the surface of NCM523 changes upon cycling from rhombohedral to spinel and rock-salt phase.⁷⁷ This reduces the capacity retention at higher voltages (~4.8 V), and hence, it is important to prevent surface degradation by doping or coating the surfaces.⁷⁷ Recently, it has been shown that capacity retention improves if NCM523 is synthesized in hollow microsphere structures, as opposed to a coprecipitation method.³¹³ To the best of our knowledge extensive calculations of NCM523 surface properties have not yet been published.

3.1.2.6. Surface Coating and Lattice Doping Studies of NCM523. Some studies have focused on doping multivalent metal ions into NCM523 to improve the electrochemical

performance and specifically to reduce the capacity fading. Wang et al. showed improved performance upon Zr⁴⁺ doping into NCM523.³¹⁴ These authors showed capacity retention of 83.78% for the Zr-doped sample, whereas the capacity retention for the undoped material is 69.35%. A series of combined experimental and theoretical DFT studies showed that Al³⁺ doped NCM523 is stabilized via strong Al–O covalent bonding, likely due Al(s)–O(p) overlap, but found little change in the voltage profiles.⁹¹ These studies employed DFT to calculate the oxygen binding energy, crystal orbital Hamilton populations, and Bader charge analysis. Additionally, these authors used GGA-based NEB calculations to show that the Li diffusion barriers are slightly increased in the Al-doped material. Further, recent work on high-valent Mo⁶⁺ doping and coating of NCM523 showed an improved capacity retention ratio up to 89.7%, even after 500 cycles.³¹⁵ Han et al. also showed that alumina oxide-coated NCM523 have more homogeneous and closely attached cathode coatings at higher annealing temperatures. This leads to a better electrochemical performance, whereas a lower amount of alumina oxide coating improves the initial capacity and cyclability.³¹⁶ In this study, the authors used ²⁷Al MAS NMR spectroscopy, along with other structural characterization techniques, to understand the homogeneity and morphology of the coating layer and bulk cathode. The authors concluded that the alumina coating is homogeneous, and Al is present only at the surface, but not in the bulk (i.e., not doped), even upon annealing at high temperatures. In a follow-up combined NMR and DFT paper, the same group showed that Al insertion into the bulk material, which does not happen in NCM523, depends on the TM composition of the bulk cathode.³¹⁵ PBE+U calculations were employed to understand the interface formed and the distribution of different LiAlO₂ phases (e.g., α - and γ -phases) on the surface. The authors found that several α -LiAlO₂ layers may form a buffer between the surface γ -LiAlO₂ layer and the bulk, in agreement with diamagnetic (surface) peaks and relaxation times observed from ²⁷Al NMR.

It was further shown by two independent groups that Mg–Al–B and Mg–Ti cosubstitution in NCM523 resulted in improved capacity retention compared to the untreated material and reduced cation mixing.^{317,318} Na-doped NCM523 was synthesized by Hua et al., wherein Na replaced some Li ions.³¹¹ This Na doping reduced cation mixing, possibly by enlarging the Li-layer spacing and hence improving the structural stability.³¹¹ Vanadium substitution in NCM523 is also a promising direction to improve the electrochemical performance, as well as the stability.³⁰¹

Breuer et al. studied Mo-doping in NCM523, adopting a combined experimental and theoretical approach.⁷⁸ Using DFT calculations, these authors showed that Mo⁶⁺ ions are preferably incorporated at Ni sites and that the doping increases the amount of Ni²⁺ ions at the expense of Ni³⁺ ions, due to charge compensation, in accord with X-ray absorption fine structure (XAFS) spectroscopy measurements.

Wu et al. showed that a composite of NCM523 and carbon nanotubes (CNT) can reach the theoretically proposed capacity of 280 mAh g⁻¹, but this was limited to a few cycles due to Mn dissolution and side reactions involving TMs.³¹⁹ Further, these authors showed in a follow-up work that the limitation can be overcome covering the complete cathode surface with CNT (40 nm thick layer), where the prelithiation process starts before cycling. They showed from XRD and PBE + U studies that, near the surface of NCM523, two Li layers

exist between TM layers, and this prevents Mn dissolution and TM side reactions at the interface during cycling.³²⁰

Further, Mo et al. recently showed that Nd-doped NCM523 stabilizes the structure during Li extraction and improves cycling stability.³²¹ In pristine NCM523, the material transforms from hexagonal H1 to H2 to H3 phases. H3 phases in the high voltage region create microcracks in the particle, forming material stress. The bulky Nd-ion substitution suppresses the H2 to H3 phase transition, thereby stabilizing the structure.

3.1.3. NCM622. Li[Ni_{0.6}Co_{0.2}Mn_{0.2}]O₂ (NCM622) was reported in the literature in 1999 by Liu et al.³¹⁰ This cathode material has been shown to give an initial discharge capacity of 187 mAh g⁻¹, which is higher than NCM materials with lower Ni content, such as NCM333 (163 mAh g⁻¹) and NCM523 (175 mAh g⁻¹) (Table 1).^{50,72,322,323}

3.1.3.1. NCM622 Structure. NCM622 has an α -NaFeO₂ structure (space group: R $\bar{3}m$).^{222,323} The experimentally determined a and c lattice parameters for this material are 2.8683 and 14.2241 Å, respectively.²²² GGA computations showed that the PBE functional can reproduce the lattice parameters quite well in the fully lithiated limit, with values of 2.89 and 14.25 Å, respectively.⁸⁷ However, the GGA computed lattice parameters were found to deviate from the expected experimental values in the fully delithiated limit.⁸⁷ This can be ascribed to the failure of the PBE functional to account for dispersion interactions, which are crucial in the fully delithiated limit.⁸⁷ Sun and Zhao analyzed the lattice parameters of various NCM materials as a function of Ni content using the PBE+U level of theory.¹⁹⁰ This study found that the lattice parameters for the pristine materials increase initially, reach a maximum for 40% Ni (NCM442), and then decrease with further increase in Ni content. This study suggested lower a and c parameters for NCM622 compared to NCM523. Interestingly, based on X-ray diffraction and cycling studies, the changes in lattice constants after 100 cycles for various NCM materials were found to increase as a function of Ni content.⁷² This indicates a larger volume change during cycling for this material compared to NCM materials with lower Ni content. The cell volume change is believed to be due to the phase transition, which is associated with oxygen release, especially at high voltage.^{72,76}

3.1.3.2. NCM622 Electronic Structure. Though Ni²⁺ ions are predominant in NCM materials with low Ni content (e.g., NCM333), the increased percentage of Ni in NCM622 results in an increase of the number of Ni³⁺ ions at the expense of Ni²⁺ ions.¹⁹⁰ DOS analysis indicates that the band gap of this material is smaller, and the Fermi level is shifted to higher energy levels compared to NCM333 and NCM523, due to the increased Ni content in NCM622.¹⁹⁰ First-principles computations with the PBE approach showed that the valence band maximum of NCM622 consists of e_g states of Ni (Ni²⁺ and Ni³⁺) and t_{2g} states of Co (Co³⁺), whereas the major component of the conduction band minimum are Ni³⁺ e_g levels.⁸⁷

3.1.3.3. NCM622 Voltage Profile. The initial discharge capacity of NCM622 was found to be 187 mAh g⁻¹ in the voltage range 3.0 to 4.3 V which is higher than those of NCM333 and NCM523.^{72,324} There is also a report that the initial discharge capacity is 178 mAh g⁻¹ in the same voltage window.⁸⁰

Jung et al. showed a capacity retention of 95% between the 5th and 300th cycles, with an initial discharge capacity of ~156

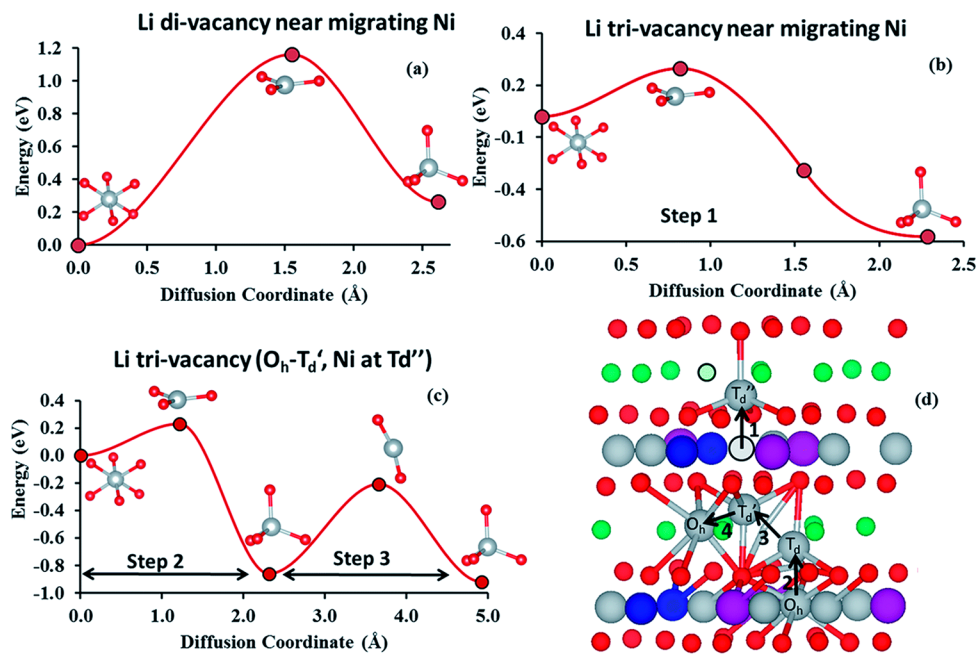


Figure 18. Energy profiles for Ni migration obtained using PBE. O_h to T_d Ni migration barrier in undoped NCM622 with Li (a) divacancy near a Ni T_d site and (b) trivacancy near the Ni T_d site. (c) O_h – T_d' – T_d'' Ni migration barrier in undoped NCM622 with Li trivacancy with one Ni at the T_d'' site (above the migrating ion layer). (d) Suggested mechanism for Ni^{2+} migration leading to a partial spinel nucleus. Color codes for spheres: red, O atoms; gray, Ni atoms; violet, Mn atoms; blue, Co atoms; and green, Ni atoms. (Reprinted with permission from ref 87. Copyright 2016, published by the Royal Society of Chemistry.)

mAh g⁻¹.⁷⁶ The cycling stability and upper cutoff voltage prior to capacity fading was found to be the same as that of NCM333, although it was found to suffer from capacity fading after 4.4 V.⁷⁶ This capacity fading observed above 4.4 V was ascribed to surface degradation caused by reaction of surface Ni^{4+} ions with the electrolyte.⁷⁶ Here, the penetration of electrolytes to the surface occurs through microcracks, which are formed as a result of anisotropic volume changes due to phase transitions occurring on prolonged cycling at high voltage, as indicated by X-ray diffraction (XRD), transmission electron microscopy (TEM), and scanning electron microscopy (SEM) experiments.^{222,323} We note that, when cycled up to 4.3 V only, no phase transitions are observed.⁷² Electrochemical studies indicate that the redox couples between 2.5 to 4.6 V are Ni^{2+}/Ni^{3+} and Ni^{3+}/Ni^{4+} .^{325–328} Schipper et al. compared the voltage profile (as a function of Li concentration) obtained from computations with experiments.⁸⁷ In this study, PBE and dispersion corrected PBE (optPBE-vdW) were found to successfully reproduce the experimental voltage trends, whereas the PBE+ U functional could not predict it correctly. The failure of PBE+ U in reproducing the experimental voltage trend was ascribed to the use of the same U parameter for different Li-intercalation limits, as the same U parameter is not necessarily suitable for a TM ion in different oxidation states.⁸⁷

3.1.3.4. Ion Diffusion in NCM622. Schipper et al. studied the migration of Ni ions in an attempt to understand the layered to spinel transformation.⁸⁷ Based on simulations employing the NEB method in conjunction with the PBE functional the authors suggested the following mechanism: Initially, Ni^{2+} from one TM layer rapidly migrates from an octahedral (O_h) site to a corresponding tetrahedral (T_d) site, followed by an O_h to T_d migration of a second Ni^{2+} from an adjacent layer (see Figure 18). This Ni can further migrate to a

corresponding T_d' site (T_d – T_d'), with a barrier of ~0.7 eV. To avoid layered-to-spinel transformations, the authors suggested doping the NCM lattice with a high-charge state cation, such as Zr^{4+} .

3.1.3.5. NCM622 Surface Studies. TEM experiments indicated a transformation from a layered to rock-salt structure at the surface layer on prolonged cycling, especially at voltages above 4.3 V.^{222,323} Schipper et al. suggested based on PBE computations in conjunction with NEB that the experimentally observed layered to spinel phase transition involves migration of Ni from an O_h site in the TM layer to an O_h site in the Li layer along a tetrahedral site.⁸⁷ According to this study, a TDH pathway involving a trivacancy was found to be the most preferred path for Ni migration.

3.1.3.6. Surface Coating and Lattice Doping Studies of NCM622. Though NCM622 has advantages in terms of enhanced capacity and lower cost, poor cycling performance and thermal stability of this material are issues of concern.³²⁹ Doping with elements such as Zr^{4+} ^{87,259} and coating with Li_3NbO_4 ,³³⁰ Li_2ZrO_3 ,³³¹ Al_2O_3 ,³¹⁵ and Li_2SiO_3 ³³² were found to improve the electrochemical performance of this material. Liu et al. carried out a comparative study on the effect of doping and coating on NCM622 by analyzing the electrochemical performance of this material with and without doping and coating.²⁵⁹ This study showed that lattice doping is a more effective strategy to improve cycling stability than coating at slightly elevated temperatures (55 °C). Modification of the surface^{330,333,334} and the electrode–electrolyte interface³²⁴ and addition of electrolyte additives³³⁵ were also found to improve the electrochemical performance of NCM622. Schipper et al. performed a combined experimental and computational study on Zr-doped NCM622.⁸⁷ Energy dispersive analysis spectroscopy (EDAS) studies and PBE computations performed in this study showed a preference for Zr doping at Ni sites. Dispersion

corrected PBE based computations performed in this study showed that Zr-doped materials undergo less change in the *c* lattice parameter compared to the undoped material during Li intercalation/deintercalation. A reduction of the band gap, an increase in the number of Ni²⁺ ions, and a decrease in the number of Ni³⁺ ions were observed by the authors as a result of Zr doping. They demonstrated that both experiments and PBE and dispersion corrected PBE (optPBE-vdW) computations give similar voltage profiles for the material. It was suggested that the higher discharge capacity of the Zr-doped material relative to the undoped material can be ascribed to an increase in Ni²⁺/Ni³⁺ ions. The improved structural stability of the Zr-doped NCM622 observed in experiments was found to be due to inhibition of layered to spinel transitions, which presumably involve migration of TM ions from the TM layer to the Li layer.⁸⁷ PBE based computations in combination with the NEB approach indicated that repulsive interaction of the migrating Ni²⁺ with the Zr⁴⁺ ions near the tetrahedral sites make the TDH pathway less feasible, and therefore the migration is forced to take place via the high energy ODH pathway (see Section 3.1.3.4 and Figure 18).⁸⁷ This dopant-induced barrier increase possibly reduces the probability of Ni-migration between TM and Li layers and hence inhibits the layered to spinel phase transition. It has also been shown that substituting Mn⁴⁺ with Nb⁵⁺ and Mo⁶⁺ in NCMs increases the concentration of Ni²⁺.^{85,86}

The SEI may be negatively affected by detrimental side reactions but can be protected via surface coating of the active mass. Han et al.³¹⁶ showed improved electrochemical performance for aluminum oxide-coated NCM622, along with other NCMs. ⁶Li NMR and high-resolution X-ray diffraction and SEM studies by Han et al. suggested that Co segregation assists diffusion of Al from the Al₂O₃ coating to the bulk on high temperature annealing in alumina oxide coated NCM622. The facilitation of Al diffusion to the bulk by Co segregation can be ascribed to the reduction of Mn content at the Co-segregated surface.³¹⁶ This was supported by PBE+U studies, which indicated that configurations with Al ions surrounded by Ni and Co are more favorable compared to Al configurations containing a Mn-rich local environment.³¹⁶

3.1.4. NCM811. NCM811 was reported in the literature in 2012 by Kim et al.³³⁶ This Ni-rich material can provide high reversible capacities of up to 200 mAh g⁻¹ at 4.6 V.^{56,337} Noh et al. reported an initial discharge capacity of 203 mAh g⁻¹ in the 3.0–4.3 V range, with 0.1C current.⁷² Neudeck et al. showed capacity retention of 80% for up to 600 cycles without coating for this material.⁸² Although the high Ni content produces good capacity, capacity fading is a serious concern, and much work on this and related Ni-rich materials focuses on stabilizing the cathodes.

3.1.4.1. NCM811 Structure. NCM811 has a $R\bar{3}m$ layered oxide structure, like other NCMs.³³⁸ In operando XRD found that the *c* lattice parameter initially increases on delithiation up to $x \sim 0.5$, followed by a decrease, whereas the *a* lattice parameter showed a monotonous decrease.³³⁷ The lattice parameters *a* and *c* and volume for the pristine material were determined by XRD to be 2.8661 Å, 14.249 Å, and 101.38 Å³, respectively, and may be compared to 2.91 Å, 13.63 Å, and 99.96 Å³, respectively, from dispersion-corrected PBE calculations.³³⁷ Clearly, PBE overestimates the *a* lattice parameter and underestimates the *c* lattice parameter and volume, although the correct trend on (de)lithiation was observed when compared with in operando XRD.³³⁷ Similar lattice

parameter trends were observed employing the PW91 XC functional, although using this functional the *a* lattice parameter was underestimated, while the *c* lattice parameter was overestimated.³³⁸

In operando synchrotron XRD and ex situ solid-state NMR studies by Grey and co-workers identified that, at a high state of charge, an increase in both Li mobility and interlayer spacing are responsible for the structural changes in NCM811, rather than an O₃ to O₁ phase transition.³³⁹

3.1.4.2. NCM811 Electronic Structure. DOS analysis of pristine NCM811 by Dixit et al.⁸⁶ indicates that Co is found to be in a 3+ LS state and Mn is in a 4+ HS state, whereas Ni was found to exist in a mixture of 2+ (HS), 3+ (LS), and 4+ (LS) oxidation states. According to this study, Ni in its 3+ oxidation state is most abundant in NCM811. The electronic valence states near the Fermi level are dominated by Ni²⁺ ion e_g and t_{2g} orbitals, whereas e_g of Ni³⁺ and Ni⁴⁺ are located at the conduction band edge.⁸⁶ Hence, Ni 3d states are located near the Fermi level, indicating the prominent role played by Ni ions in electrochemistry. Based on COHP bonding analysis and Bader charges, Dixit et al. suggested that the covalency of the Ni–O bond increases with increase in the oxidation states of Ni.⁸⁶ A comparative study of several Ni-rich NCMs performed by these authors demonstrated that, as the concentration of Ni increases in the NCM material, the concentration of Ni ions with high valence state increases (i.e., Ni³⁺, Ni⁴⁺). Ni⁴⁺, which has low-lying LUMO states, is easily reduced, and as a result oxygen binding energy decreases. We note that using the PW91+U approach did not predict significant Ni states near the Fermi level.³³⁸

3.1.4.3. NCM811 Voltage Profile. Due to the high Ni content, NCM811 provides good capacity.³⁴⁰ Jung et al. measured a capacity retention of 66% from the 5th to 300th cycles with an initial discharge capacity of 172.5 mAh g⁻¹ in a voltage range of 4.0 V.⁷⁶ Kim et al. found a discharge capacity of 197–202 mAh g⁻¹ in a voltage range of 3.0–4.2 V with 0.1C rate.⁸¹ The PW91+U computed voltage profile for this Ni-rich NCM material is in the range 3.5–4.2 V, in agreement with experiment.³³⁸

3.1.4.4. Ion Diffusion in NCM811. Noh et al. showed that Li diffusivity increases with increasing content of Ni in NCM systems, and the diffusivity of NCM811 is 10⁻⁸ cm² s⁻¹, which is 3 orders of magnitude greater than in NCM333.⁷² As mentioned before, Li ions follow an ODH pathway in the early stages of delithiation, while following a TSH pathway after delithiation of one-third of the Li ions in most NCM materials. This is the case for NCM811 as well, as reported by Wei et al.¹¹⁷ These authors calculated a diffusion constant of nearly 10⁻⁸ cm² s⁻¹ from AIMD simulations for NCM811, which is higher than that for NCMs with less Ni content.

3.1.4.5. NCM811 Surface Studies. Liang et al. reported a computational study addressing surface segregation in NCM811 using PBE+U.²²⁴ These authors showed that Ni ions segregate at nonpolar surfaces (see Figure 19), such as (100), (104), and (110), where the (104) surface plane is energetically the most stable one. Further, these authors suggested, based on the calculated surface formation energies in the absence and the presence of Li and Ni exchange, that the surface lattice structure transforms into different phases, like rock-salt. This segregation of Ni ions and the subsequent rock-salt formation phenomenon were suggested to cause deterioration in the electrochemical performance by blocking Li-ion diffusion paths.²²⁴

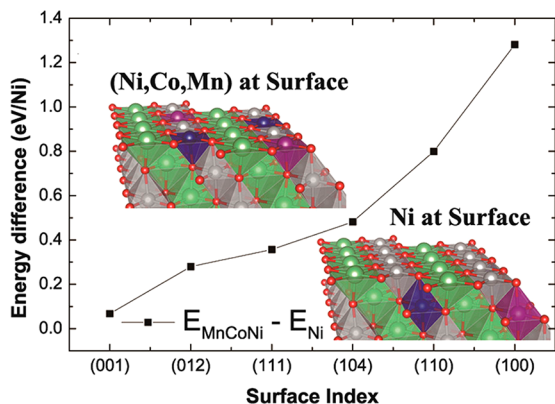


Figure 19. Energy difference between Mn–Co–Ni- and Ni-terminated surfaces. The inset shows a structural model of the NCM811 (104) surface. (Reprinted with permission from ref 224. Copyright 2018, The American Chemical Society.)

Xiong et al. reported experiments suggesting that Li ions at the surface reduce the performance of NCM811, although this can be prevented by adding $(\text{NH}_4)_2\text{HPO}_4$, which reduces side reactions and results in good capacity retention (66.9%) after 100 cycles at 2C, compared to the pristine material (48.1%).^{341,342} Li et al. synthesized Ni-rich core and Mn-rich shell NCM811 materials and showed that the capacity retention for the core–shell is 65.1%, whereas it is 49.2% after 105 cycles.³⁴³

3.1.4.6. Surface Coating and Lattice Doping Studies of NCM811. The major drawback of the Ni-rich family of NCM materials, such as NCM811, is the lack of stability of the materials upon cycling, but surface coating can improve stability. Recently, Neudeck et al. showed capacity retention of 80% up to 600 cycles and 1200 cycles for uncoated and alumina coated NCM811, respectively.⁸² Schipper et al. also showed that the surface coating and lattice doping of NCM811 with ZrO_2 and Zr, respectively, improve the cycling stability and lower the impedance of the systems.⁹² These authors used DFT calculations to show that doped Zr ions preferably occupy Ni sites. Additionally, using the coincident site lattice method,³⁴⁴ they found that the interface of the (110) plane of NCM811 and (001) plane of ZrO_2 in the coated material has less strain compared to other possible interfaces, and this interface does not block Li-diffusion channels.⁹² Further, Han et al. found that aluminum oxide coated NCM811 performs well. The authors observed that some Al transports to the cathode bulk, in the form of dopant atoms, at high annealing temperatures, and this is thought to improve the electrochemical cyclability.³¹⁶ Han et al. used ^{27}Al NMR, the PBE+U method, and other structural characterization techniques to show that the electrochemical performance improves for alumina oxide coated NCM523, NCM622 (as discussed in Sections 3.1.2 and 3.1.3), and NCM811.³¹⁶ These authors showed that reducing the amount of Mn in the NCM facilitates diffusion of Al from the surface to the bulk, and hence coating transforms to doping. PBE+U calculations suggested that Mn–Al repulsion is responsible for the inability of Al to penetrate into the bulk in Mn-rich materials, and hence reducing the amount of Mn is desirable if one is interested in Al lattice doping via annealing of the coated NCM material.

Experimentally, Zhang et al. reported that 0.5% doping of Rb into NCM811 improves the electrochemical performance of

the material by increasing the discharge capacity by 13.52%.³⁴⁵ In this Rb-doped NCM811, Rb replaces Li ions, thereby reducing the cation mixing. This study also showed that Rb doping results in an increase in the *c* lattice parameter, which improves the electrochemical performance of the material by accelerating Li-ion transportation. There are also reports on improved electrochemical performance for Cr-doped NCM811.³⁴⁶

3.1.5. NCM with >80% Ni. NCM cathode materials with Ni contents of 85%, 90%, and 95% have also been reported and characterized experimentally.^{72,93,312,315} These systems are prepared as layered $\text{R}\bar{3}m$ structures and can provide charge capacities up to 245 mAh g^{-1} during the first cycle. However, significant capacity fading is observed due to transformation to spinel or rock-salt phases, with concomitant oxygen release upon cycling.⁷² In the case of NCM with 85% Ni, the discharge capacities are 206 mAh g^{-1} at room temperature and 213.8 mAh g^{-1} at 55 °C in the voltage range 2.7–4.3 V.³⁴⁷ This study shows that the Co-to-Mn ratio can affect optimal stability and capacity, and a ratio of Co:Mn = 0.05:0.10 provided the best result. Further, spherical core–shell NCM particles with 95% Ni improved capacity retention up to 90% after 100 cycles compared to 74.2% LiNiO_2 , and this is due to the highly reactive surface in core–shell particles.³¹⁵

Li et al. showed that Co-free Ni-rich layered oxides such as $\text{Li}_x\text{Ni}_{0.95}\text{M}_{0.05}\text{O}_2$ ($\text{M} = \text{Al}, \text{Mn}, \text{or Mg}$) are able to suppress multiple phase transitions that occur in Co-containing $\text{LiNi}_{0.95}\text{Co}_{0.05}\text{O}_2$.³⁴⁸

Kim et al. showed that low-level tungsten (W) doping in LNO and NCM with more than 80% Ni can provide high specific capacity (247 mAh g^{-1} at 4.3 V).⁹³ These authors used surface slab calculations to show that W-doped rock-salt surfaces are energetically more favorable than undoped rock-salt surfaces in LNO, whereas W-doped layered surfaces are less stable than the undoped surface. These results were used to rationalize the experimentally observed segregation of the rock-salt phase at the surface in W-doped LNO. In this particular study, W was doped at Li sites in the *in silico* studies.

Further, Park et al. recently showed a discharge capacity of 237 mAh g^{-1} at 4.3 V for 1 mol % B doped NCM9055 with 91% capacity retention after 100 cycles.³⁴⁹

3.1.6. Additional NCMs. Additional NCMs have been studied, such as NCM424 and NCM71515. We briefly discuss these NCMs below.

3.1.6.1. NCM424. Layered NCM424 was synthesized with $\text{R}\bar{3}m$ structure having lattice parameters $a = 2.866 \text{ \AA}$ and $c = 14.254 \text{ \AA}$ and 4.4% Li/Ni mixing, as determined from XRD measurements.³⁵⁰ These authors reported a discharge capacity of 180 mAh g^{-1} within a 2.5–4.4 V window. Magnetic measurement revealed that the presence of Ni ions in the Li layers decreases with increasing amounts of Co, hence stabilizing the structure upon cycling.

Theoretical studies using PBE+U with dispersion corrections compared the cycling behavior of NCM424 relative to other NCMs.⁸⁶ In this study, Dixit et al. found that the *c* parameter of NCM424 is greater than Ni-rich NCMs, like NCM811, and on delithiation the *c* parameter initially increases and then decreases toward the delithiation limit. The lattice parameter *a* decreases from 2.90 to 2.84 \AA from the fully lithiated to the delithiated state. Further, the Ni ions were found to be in a 2+ oxidation state, and the band gap is higher than for other Ni-rich materials, like NCM811. NCM424 also has greater oxygen binding energy than NCM811, as it has

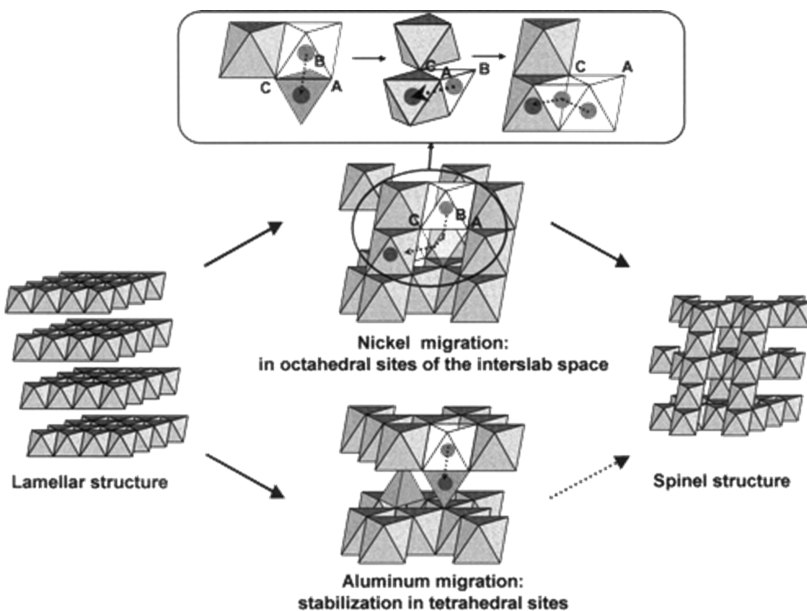


Figure 20. Theoretical path for the nickel or aluminum ions during the lamellar to spinel transition. In the case of aluminum migration, the intermediate structures with aluminum in tetrahedral sites are stabilized, thereby pushing the formation of the pseudospinell-type phase to higher temperatures. (Reprinted with permission from ref 90. Copyright 2003, The American Chemical Society.)

more electronegative oxygens, as revealed from Bader charge analyses.⁸⁶

In another theoretical study, Sun et al. used PBE+U to obtain an electronic structure for NCM424 that is similar to that found by Dixit et al., with almost all Ni ions in a 2+ state and a bigger band gap than Ni-rich materials.¹⁹⁰ Sun et al. also showed that the relative mechanical and thermal stability follows the expected trend NCM333 > NCM424 > NCM811. Wei et al. discussed the kinetics of Li diffusion in NCM424 based on calculations using the climbing image NEB method in comparison with other NCMs discussed above.¹¹⁷ They showed that NCM424 also follows an ODH pathway during initial delithiation and a TSH pathway after one-third Li removal, like other NCMs. The calculated diffusion coefficient ($\sim 10^{-8}$ cm²/s) is lower compared to those of other Ni-rich NCMs.

3.1.6.2. NCM71515. Noh et al. reported structural and electrochemical properties of NCM71515 ($\text{Li}_{0.7}\text{Co}_{0.15}\text{Mn}_{0.15}\text{O}_2$).⁷² This NCM also possesses an $R\bar{3}m$ structure, with an initial discharge capacity of 194 mAh g⁻¹ between 3.0 and 4.3 V (see Figure 3). These authors showed the reduced stability of this Ni-rich NCM compared to NCM333, NCM523, and NCM622.⁷²

Similar to other NCMs, Li-ion diffusion follows ODH and TSH pathways for initial and late-stage Li-ion extraction, as reported by Wei et al.¹¹⁷ Wei et al. showed that the diffusion coefficient of NCM71515 is ca. 10^{-8} cm² s⁻¹, which is higher than those of NCM333 and NCM523. The experimental conductivity reported by Noh et al. is 9.3×10^{-6} S cm⁻¹.⁷² The calculated ratio of $\text{Ni}^{3+}/\text{Ni}^{4+}$ ions at different states of charge (SOC) are as follows: at SOC = 0.33, the ratio is 0.52/0.18, and at SOC = 0.5, the ratio is 0.35/0.35.¹¹⁷

3.2. NCA Materials. NCA is a family of promising cathode materials that has been commercialized by Panasonic for Tesla electric vehicles. NCA materials are found to have higher capacity (~ 200 mAh g⁻¹) and specific energy (680–760 Wh/kg) than corresponding NCMs, as well as lower cost. The presence of Al improves thermal stability of NCAs by

preventing phase transitions, which are believed to be responsible for the instability of layered materials at high temperatures. The prevention of phase transitions in NCAs is due to Al^{3+} ions occupying stable tetrahedral sites, which inhibit cation migrations.⁸⁸ Guilmarc et al.⁹⁰ proposed a migration path for the Al^{3+} ions that prevents phase transition in NCA, as shown in Figure 20. In NCA materials, Ni ions are in a 3+ oxidation state, which are Jahn–Teller (JT) active, and this JT behavior strains the Ni octahedra. However, the presence of Al reduces this strain due to preferential ordering of long JT Ni^{3+} –O bonds near the Al^{3+} ion, instead of a preference for Al^{3+} to be coordinated by Ni^{3+} , and as a result improves the ordering of atoms in the TM layers.¹⁶⁹ The local JT ordering increases the number of long JT Ni^{3+} –O bonds directed toward Al, thereby accommodating the strain of the dynamic JT distortion. The presence of Al in NCA has also been observed to reduce the variation of the *c* lattice parameter on cycling compared to Al-free analogous materials.³⁵¹ It is also important to note that the presence of Al in NCA also reduces oxygen release by reducing the probability of an exothermic reaction with the cathode and electrolyte.^{351,352}

3.2.1. NCA333. $\text{Li}[\text{Ni}_{0.33}\text{Co}_{0.33}\text{Al}_{0.33}\text{O}_2$ (NCA333) was reported by Lin et al. in 2005.³⁵³

3.2.1.1. NCA333 Structure. NCA333 has a $R\bar{3}m$ layered oxide structure like NCMs.²⁸⁸ The optimized *a* and *c* lattice parameters of NCA333 computed using the HSE06 functional²⁸⁸ were found to be 2.843 and 14.23 Å, respectively,³⁵⁴ in good agreement with the experimental *a* and *c* lattice parameters reported by Swider-Lyons et al. (2.83 and 14.15 Å, respectively).^{353,354} A comparison of *a* and *c* lattice parameters obtained from HSE06 computations for NCM333 and NCA333 indicates a slight reduction in the values of these lattice parameters, which in turn results in a contraction of the volume of NCA333 compared to NCM333. This contraction along the *c*-axis may be ascribed to the radius of Al^{3+} (0.51 Å), which is smaller than that of Mn^{4+} (0.53 Å). Additionally, the radius of Ni^{3+} (0.60 Å), which is present in NCA333, is smaller than that of Ni^{2+} (0.69 Å), which predominates in

NCM333.^{288,353,354} In NCA333, the JT active Ni³⁺ sits in an octahedral site with two Ni–O bonds with lengths of 2.06 Å and four Ni–O bonds with lengths of 1.89 Å.²⁸⁸ There is no long-range order between Ni–Co–Al TMs in NCA333, whereas NCM333 (note that Ni ions are in 2+ state) has long-range order for Ni–Co–Mn in the TM layers, as shown from the calculation of energies for site exchange between different TMs site.²⁸⁸

3.2.1.2. NCA333 Electronic Structure. DOS and PDOS computed by Hoang and Johannes employing the HSE06 functional indicates that Ni and Co atoms of NCA333 are in their low spin 3+ oxidation state.²⁸⁸ Ni 3d states were found to contribute significantly to the valence band (28% contribution) and conduction band (60% contribution), similar to LiNiO₂.²⁸⁸ The computed band gaps for this material (2.22 eV) were found to be lower than those of NCM333 (2.88 V) using HSE06.²⁸⁸

3.2.1.3. NCA333 Voltage Profile. Love et al. reported a specific capacity for NCA333 of 115 mAh g⁻¹ within the voltage range 2.5–4.5 V.³⁵⁴ Further, Hoang and Johannes reported the computed voltage range for NCA333 to be between 3.8 and 5.8 V using HSE06, which is significantly higher than for NCM333 using the same method.²⁸⁸

3.2.1.4. Ion Diffusion in NCA333. Hoang and Johannes also studied lithium migration in NCA333 using the HSE06 functional in combination with the NEB approach.²⁸⁸ Analysis of lithium diffusion along various possible paths via mono- and divacancy mechanisms indicated migration barriers of 0.64–0.95 eV and 0.35–0.40 eV for mono- and divacancy mechanisms, respectively. The mono- and divacancy mechanisms are expected to be favored in the fully lithiated and partially delithiated limits, respectively.²⁸⁸ The Li migration barrier computed for NCA333 was found to be higher than that obtained for NCM333, and this was ascribed to the shrinking of the lattice parameter *c* of NCA333 due to the presence of Al ions, as well as Ni³⁺ ions, with smaller ionic radii compared to the TM ions in NCM333.²⁸⁸

3.2.1.5. Surface Coating and Lattice Doping Studies of NCA333. Electrochemical properties of NCA333 were found to improve on surface coating with materials such as metal oxides, metal phosphates, metal fluorides, metal oxyfluorides, and metal hydroxides.^{50,355–357} To the best of our knowledge, no computational work has addressed coating or doping in NCA333.

3.2.2. NCA8155. LiNi_{0.8}Co_{0.15}Al_{0.05}O₂ (NCA8155) was reported by Cao et al. in 2004.³⁵⁸ Considering that Al³⁺ is electrochemically inactive, it is advantageous to reduce the amount of this metal to a minimum. In NCA8155, a small amount of Al improves the capacity retention, yet the capacity remains high due to the increased amount of Ni ions. Indeed, this Ni-rich NCA material delivers a high discharge capacity of about 200 mAh g⁻¹, and the specific energy of this material was found to be in the range of 680–760 Wh/kh.³⁵⁹

3.2.2.1. NCA8155 Structure. X-ray and neutron diffraction studies by Trease et al. showed that NCM8155 has a $\bar{R}\bar{3}m$ layered oxide structure, with *a* and *c* lattice parameters 2.864 and 14.180 Å, respectively.¹⁶⁹ Identical values for *a* and *c* lattice parameters (*a* = 2.864 Å and *c* = 14.180 Å) were also observed in the experimental studies of Kondu et al.³⁶⁰ Trease et al. further showed from theoretical calculations and experimental ²⁷Al and ⁷Li NMR, atom probe tomography, XRD, and neutron measurements that Al ions are uniformly distributed in NCA8155.¹⁶⁹ The theoretical approach

combined the cluster expansion method and DFT using the B3LYP hybrid functional. These authors also used DFT to show that a single, layered phase exists for NCA with Al doping up to 80% in agreement with experiment, whereas above this Al concentration phase separation occurs. They observed that Ni³⁺ is JT active in this NCA and the Al³⁺ site is coordinated by Ni³⁺ ions where there are three different interaction pathways; one is Al–O–Ni 90° interactions along the short JT axis, and the remaining two are Al–O–Ni pathways along the short and long JT axis; these findings are consistent with NMR. Further, Leifer et al. showed changes of the structure during charging and discharging in this NCA material from ²⁷Al and ⁷Li NMR measurement where the Al nuclei served as static reporters, while the Li nuclei are dynamic reporters.³⁵¹ Both nuclei show an increase in the oxidation state of Ni ions during cycling. They reported that Al ions are surrounded by at least two different Ni ions from ²⁷Al NMR. These two different configurations were attributed to the segregation of Co ions and the presence of Ni²⁺ ions. Calculations were not performed in this study.

Eremin et al. predicted multiple configurations for LiNiO₂ and NCA8155 for a wide range of delithiated cases, using a topological approach and DFT modeling.³⁶¹ Using these techniques the authors were able to predict structural changes in NCA during cycling and identify inhomogeneity of the charge in cationic and anionic sublattices due to the presence of Al. They also showed from a machine learning method that most unfavorable configurations are those that have nonuniform Li distribution, and that the polyhedra of Li shares a maximum number of vertices of Al polyhedra for all favorable configurations.

Flores et al. explored the local structure evolution of NCA8155 using operando Raman spectroscopy and DFT (PBE+U).³⁶² They found that the vibrational motion of lattice oxygen solely depends on the TM–O bond strength and limit of lithiation.

3.2.2.2. NCA8155 Electronic Structure. Trease et al. performed first-principles calculations for this NCA material using several methods, such as dispersion corrected PBE+U and cluster expansion.¹⁶⁹ Eremin et al. also reported a first-principles PBE study of this cathode compound using DFT³⁶¹ and concluded that, in the pristine material, Ni, Co, and Al are all in a 3+ oxidation state.

3.2.2.3. NCA8155 Voltage Profile. The specific capacity of this material was found to be 200 mAh g⁻¹ in the voltage window 3.0–4.2 V.^{50,363} Song et al. reported the initial discharge capacity of 183.1 in the range of 3.0–4.3 V with a 0.2C rate and a capacity retention of 89.31% after 110 cycles.⁸³ We note that Co reduction does not have a major impact on its intercalation potential and specific capacity as indicated by DFT studies using PBE+U and opt-PBE functionals by Ghatak et al.³⁶⁴

3.2.2.4. Ion Diffusion in NCA8155. The transport properties of Li ions in this NCA material based on measurements of ion and electron blocking configurations were reported by Amin et al.³⁶⁵ The lithium ion diffusion barrier was determined to be 1.25 eV based on temperature dependent kinetic studies. These authors showed that electronic conductivity increases from a fully lithiated to a partially lithiated state, and it increases sharply after some limit (beyond 60%) due to the presence of multivalent Co ions. Further, these authors measured the diffusivity of Li ions and observed that diffusivity adopts a V-shaped curve as a function of the Li contents (i.e.,

first decreases to a minimum at $x = 0.5$ and subsequently increases). To the best of our knowledge, diffusion in this material has not been studied theoretically.

3.2.2.5. NCA8155 Surface Studies. Zhang et al. reported the cycling behavior of AlF₃-coated NCA8155 and found the material to be quite stable, showing good capacity retention (96.3% of its initial capacity after 30 cycles).³⁶⁶ Karki et al. observed oxygen loss at the NCA8155 surface, and a phase transformation occurs for overcharged NCA8155. This is a serious safety issue, but the authors showed that if these NCA8155 particles are embedded in an oxygen-rich environment, this problem can be reduced.³⁶⁷ Using STEM, Zhang et al. showed two types of rock-salt induced surface reconstruction in layered NCA8150S, (002) and (111) type rock-salt surfaces. In the (002) type rock-salt structure, TMs migrate to Li sites and form a flatter surface compared to that of (111) which forms a hill and valley-like rock-salt structure.³⁶⁸ Further, the same group recently described the phase transition at the surface of NCA8150S due to loss of oxygen.²⁵⁰ They showed initial formation of amorphized rock-salt, followed by crystalline rock-salt formation at the subsurface during the process of oxygen loss, as we discussed in Section 2.3.6.

3.2.2.6. Surface Coating and Lattice Doping Studies of NCA8155. Kondo et al. reported the effect of doping Mg in LiNi_{0.8}Co_{0.15}Al_{0.05}O₂ and found improved battery performance.³⁶⁰ Mg doping into NCA8155 reduces the amount of Ni²⁺ ion in the Li layer that appears upon cycling of the material. Zhang et al. studied the effect of AlF₃ coating on NCA8155 and found that the AlF₃ and AlPO₄ coated material has improved cycling stability and good capacity retention.³⁶⁶ An experimental study by Srur-Lavi et al. showed that LiAlO₂ coated NCA8155 shows three times less capacity fading compared to the bare NCA8155 because coating lowers the side reaction of the electrodes with the electrolyte.³⁶³ These authors also showed that there is no structural change from R̄3m for bare or coated NCA8155 after some cycling. To the best of our knowledge, surface coating or lattice doping in this material has not been studied theoretically.

3.2.3. NCA with >80% Ni. A NCA cathode material, Li[Ni_{0.865}Co_{0.120}Al_{0.015}]O₂, with a Ni-rich concentration gradient, where the core is Ni-rich, has been reported. The effect of this Ni concentration gradient is to enhance the thermal stability and capacity retention, since the surface is Co-rich.^{369,370} Calculations were not performed in this study.

A comparison on the performance of NCA and NCM with more than 80% Ni is shown in Figure 21, as reported by Myung et al.⁵⁰ These authors showed that Ni-rich NCM and NCA can both provide good capacity, but there are issues of thermal stability and cyclability.

Park et al. recently proposed a rationale for the degradation in electrochemical performance in different Ni-rich NCAs with increasing Ni content.³⁷¹ They reported discharge capacities of 202.5 mAh g⁻¹ for NCA80, 219.8 mAh g⁻¹ for NCA88, and 236.8 mAh g⁻¹ for NCA95 and corresponding capacity retentions of 95.7%, 88.7%, and 85.5%, respectively, after 100 cycles. They showed that capacity fading in these materials is related to the formation of microcracks within the cathode particle, and this is attributed to the presence of unstable Ni⁴⁺ on the crack faces, which may react with electrolyte species. Further, the electrolyte permeates the cracks and causes structural damage.

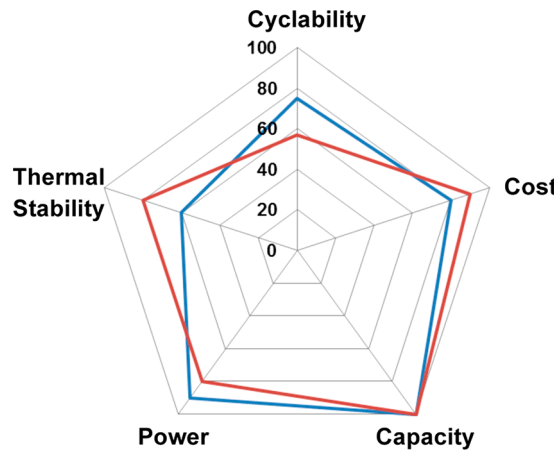


Figure 21. Radar chart comparing the performances of NCA (Ni 80%), blue line, and NCM (Ni 80%), red line. (Reprinted with permission from ref 50. Copyright 2017, The American Chemical Society.)

4. SUMMARY AND CONCLUDING REMARKS

First-principles and empirical computational methods have become an invaluable tool in the study of Li-ion batteries. In this review, we provided an overview of theoretical work performed on layered cathode materials, using a range of theoretical methods. Such methods can provide significant microscopic details of layered cathode properties, such as ionic positions, crystal cell parameters, stability, electronic structure, preferred doping sites, chemical activities of the elements, intercalation potentials, possible diffusion path of Li ions, surface segregation, reaction between the surface of the electrodes and the electrolyte, oxygen release, and NMR spectra. In this review we focused particularly on work targeting LiNi_{1-x-y}Co_xMn_yO₂ and LiNi_{1-x-y}Co_xAl_yO₂ cathode materials. A number of general conclusions may be drawn based on the myriad of theoretical work performed in this area, and we summarize some of these here:

- (1) Next-generation DFT approaches, like the SCAN meta-GGA functional, are well suited to treat problems in computational electrochemistry, like NCM and NCA materials.
- (2) Classical simulation methods, in conjunction with DFT, can be very useful in identifying the correct cation distribution in NCM and NCA materials.
- (3) The *c* lattice parameter of layered NCM and NCA materials is important for its stability and Li-ion diffusivity. The *c* parameter displays a complex behavior on Li deintercalation, first increasing up to a certain delithiation limit and then decreasing toward the fully delithiated limit. Dispersion interactions play a key role in this behavior, as revealed by dispersion corrected DFT calculations.
- (4) The population of different oxidation states of the TMs varies greatly for different NCM and NCA materials, and theory can be useful in predicting such populations. Most DFT studies identify electronic d states of Ni ions near the Fermi level for pristine NCM and NCA materials, suggesting that Ni plays a key role in electrochemistry.
- (5) DFT studies find that the band gap in NCM and NCA materials is reduced with increasing Ni content.
- (6) DFT studies suggest that high-valence doping can suppress highly oxidizing ions, like Ni⁴⁺, and hence have a positive effect on capacity retention.
- (7) Oxygen binding is found to be lower in Ni-rich layered materials, though these materials provide a good capacity, and hence oxygen release is predicted to be more rapid with

increasing Ni content. (8) Dopants have been found to affect oxygen binding energies as computed using DFT and hence influence oxygen release. Dopants have also been found to influence the relative stability of material phases observed during cycling, such as layered, spinel, and rock-salt. (9) In most of the NCM and NCA materials, diffusing Li-ions follows an ODH pathway during early delithiation, while at later stages of deintercalation Li ions follow a TSH pathway. The ODH pathway is expected to be the rate limiting step and hence determine the experimentally observed diffusion rate. (10) In layered $R\bar{3}m$ materials, the (104) surface is energetically favorable. Questions of surface segregation in Ni-rich materials, as well as phase changes at the surface, have been addressed from theoretical approaches.

Beyond the many properties of layered NCM and NCA materials discussed in this review, an additional crucial aspect related to the rapidly growing use of LIB is disposal of spent batteries.^{372–375} Inefficient or reckless disposal of spent LIBs can result in various environmental and health issues due to the presence of toxic and flammable heavy metals and organic electrolyte components in these materials.^{373–378} Currently, biometallurgical, pyrometallurgical, and hydrometallurgical processes are widely used approaches for recycling.^{372,374,376,379,380} Molecular level insights from computational studies can provide vital information on the factors affecting the recycling properties of spent LIBs, as shown by recent studies on LiCoO_2 ,³⁸¹ NCM333,²⁸⁷ and Mn-rich NCM materials.³⁸² Thus, in conjunction with the ongoing efforts toward improving electrochemical properties of LIBs, development of environmental benign recycling technologies of spent LIBs is also of great importance.

In spite of the significant advance in the area of computational materials science, limitations with current methods leave room for improvement. Next, we summarize some points related to the core issue that all computed properties depend on, namely, the PES, followed by aspects relating to the realistic atomic-level modeling.

The GGA method gives reasonably good electron density but often fails to predict correct band gaps and certain electrochemical properties. Adding the empirical $+U$ to PBE often improves the band gap but thereby introduces deficiencies into the electron density. Due to the empirical nature of U , inappropriate values of U (e.g., high values) often incorrectly perturb the electronic structure. Additionally, the PBE+ U approach is problematic for continuous (de)lithiation processes, as the oxidation states of transition metals change during this process, and oxidation state dependent U parameters should not be altered as one is in essence changing the energy functional. Additionally, neither PBE nor PBE+ U account for any significant short-range dispersion interactions. The performance of computationally expensive hybrid functionals, such as HSE06, depends on the amount of exact exchange used, and the optimal amount can be system dependent. Recently we have shown that the newly developed meta-GGA functional SCAN improves the performance for layered cathode materials due to better treatment of dispersion interactions and localized states.^{138,209} For layered oxides, which include strongly correlated elements, these higher rung DFT functionals perform better than lower level functionals for a range of properties, including electrochemically relevant properties. So, future improvements in XC functionals in DFT will undoubtedly have great impact on the accuracy of the computed physical and electrochemical properties for battery

materials. Additional developments that will be crucial for computational electrochemistry is further advancement of linear scaling DFT methods, which will allow simulations that are both longer and of increasingly larger systems.

An additional challenge for the current state-of-the-art computational electrochemistry approaches is more realistic modeling of the cathode system being studied.¹⁰⁰ Both DFT and empirical force field type potentials require an atomic level model that reflects the experimental phase of the materials. Indeed, without such a realistic model, any calculations could be meaningless. In the case of NCM and NCA materials, it is essential to know the distribution of metals in the TM layer, as well as the extent and nature of cation mixing between the Li and the TM layers. Methods for such predictions have been presented recently.^{85,283} Additionally, it is crucial to know what the active phase of the material is and what possible phase transitions can take place. In Ni-rich NCM and NCA materials, as well as in Li-excess layered materials, phase transitions are known to take place on cycling. In NCM and NCA materials, transitions to spinel and rock-salt phases take place, but the atomic level structure and distribution of these phases are not always well characterized. In particular, the atomic level structure of metastable states, such as disordered phases, is challenging to predict for computational approaches. In such cases, methods that incorporate experimental data from XRD and NMR may be advantageous,²⁸³ as well as KMC or genetic algorithm based methods.¹⁰⁰ If the search configuration space is large, one must invariably resort to classical energy potential methods. Additionally, it can be challenging to treat low-concentration doping, as it is necessary to employ very large supercells and identify the correct doping site using configuration search methods. Moreover, dopants tend to segregate at the surfaces of particles and might preferentially stabilize certain phases, like rock-salt, although the detailed role of dopants is not fully understood.⁹³ Also, constructing realistic models of surface coating, including the accompanying interfaces, is a significant challenge. Finally, the chemistry between cathode and electrolyte occurring at the SEI is a significant computational challenge that is being addressed by several groups, but much remains to be done in this area. Future studies of such interface chemistry will likely see an increasing use of multiscale tools.³⁸³

■ AUTHOR INFORMATION

Corresponding Author

Dan Thomas Major – Department of Chemistry and Institute for Nanotechnology & Advanced Materials, Bar-Ilan University, Ramat-Gan 52900, Israel;  orcid.org/0000-0002-9231-0676; Phone: + 972 3 531 73 92; Email: majort@biu.ac.il; Fax: + 972 3 738 40 53

Authors

Arup Chakraborty – Department of Chemistry and Institute for Nanotechnology & Advanced Materials, Bar-Ilan University, Ramat-Gan 52900, Israel

Sooraj Kunnikuruvan – Department of Chemistry and Institute for Nanotechnology & Advanced Materials, Bar-Ilan University, Ramat-Gan 52900, Israel

Sandeep Kumar – Department of Chemistry and Institute for Nanotechnology & Advanced Materials, Bar-Ilan University, Ramat-Gan 52900, Israel

Boris Markovsky – Department of Chemistry and Institute for Nanotechnology & Advanced Materials, Bar-Ilan University,

Ramat-Gan 52900, Israel;  orcid.org/0000-0001-7756-0071

Doron Aurbach – Department of Chemistry and Institute for Nanotechnology & Advanced Materials, Bar-Ilan University, Ramat-Gan 52900, Israel;  orcid.org/0000-0001-8047-9020

Mudit Dixit – Department of Chemistry and Institute for Nanotechnology & Advanced Materials, Bar-Ilan University, Ramat-Gan 52900, Israel;  orcid.org/0000-0001-9456-7806

Complete contact information is available at:
<https://pubs.acs.org/10.1021/acs.chemmater.9b04066>

Author Contributions

[†](A. Chakraborty, S. Kunnikuruvan, and S. Kumar) These authors contributed equally.

Notes

The authors declare no competing financial interest.

ACKNOWLEDGMENTS

This work was partially supported by the Israel Science Foundation (ISF) in the framework of the INREP project.

LIST OF FREQUENTLY USED ABBREVIATIONS

DFT: Density functional theory

DOS: Density of states

GGA: Generalized gradient approximation density functional

HSE06: Heyd–Scuseria–Ernzerhof 06 hybrid functional

KMC: Kinetic Monte Carlo

LCO: LiCoO₂

LDA: Local density approximation density functional

LIB: Lithium-ion battery

LMO: LiMnO₂

LNO: LiNiO₂

MC: Monte Carlo

MD: Molecular Dynamics

NCA: LiNi_{1-x-y}Co_xAl_yO₂

NCA333: LiNi_{0.3}Co_{0.3}Al_{0.3}O₂

NCA81515: LiNi_{0.80}Co_{0.15}Al_{0.15}O₂

NCM: LiNi_{1-x-y}Co_xMn_yO₂

NCM333: LiNi_{0.3}Co_{0.3}Mn_{0.3}O₂

NCM424: LiNi_{0.4}Co_{0.2}Mn_{0.4}O₂

NCM45145: LiNi_{0.45}Co_{0.10}Mn_{0.45}O₂

NCM523: LiNi_{0.5}Co_{0.2}Mn_{0.3}O₂

NCM622: LiNi_{0.6}Co_{0.2}Mn_{0.2}O₂

NCM71515: LiNi_{0.70}Co_{0.15}Mn_{0.15}O₂

NCM811: LiNi_{0.8}Co_{0.1}Mn_{0.1}O₂

NEB: Nudged elastic band

NMR: Nuclear magnetic resonance

OCV: Open circuit voltage

ODH: Oxygen dumbbell hopping

PBE: Perdew–Burke–Ernzerhof density functional

PBE+U: Perdew–Burke–Ernzerhof + Hubbard-U functional

PES: Potential energy surface

SCAN: Strongly constrained and appropriately normed functional

TM: Transition metal

TSH: Tetrahedral site hopping

XRD: X-ray diffraction

REFERENCES

- (1) Dincer, I. Renewable energy and sustainable development: a crucial review. *Renewable Sustainable Energy Rev.* **2000**, *4* (2), 157–175.
- (2) Panwar, N. L.; Kaushik, S. C.; Kothari, S. Role of renewable energy sources in environmental protection: A review. *Renewable Sustainable Energy Rev.* **2011**, *15* (3), 1513–1524.
- (3) Thackeray, M. M.; Wolverton, C.; Isaacs, E. D. Electrical energy storage for transportation—approaching the limits of, and going beyond, lithium-ion batteries. *Energy Environ. Sci.* **2012**, *5* (7), 7854–7863.
- (4) Liu, J.; Zhang, J.-G.; Yang, Z.; Lemmon, J. P.; Imhoff, C.; Graff, G. L.; Li, L.; Hu, J.; Wang, C.; Xiao, J.; Xia, G.; Viswanathan, V. V.; Baskaran, S.; Sprenkle, V.; Li, X.; Shao, Y.; Schwenzer, B. Materials Science and Materials Chemistry for Large Scale Electrochemical Energy Storage: From Transportation to Electrical Grid. *Adv. Funct. Mater.* **2013**, *23* (8), 929–946.
- (5) Ellabban, O.; Abu-Rub, H.; Blaabjerg, F. Renewable energy resources: Current status, future prospects and their enabling technology. *Renewable Sustainable Energy Rev.* **2014**, *39*, 748–764.
- (6) Owusu, P. A.; Asumadu-Sarkodie, S. A review of renewable energy sources, sustainability issues and climate change mitigation. *Cogent Eng.* **2016**, *3* (1), 1167990.
- (7) Dunn, B.; Kamath, H.; Tarascon, J.-M. Electrical Energy Storage for the Grid: A Battery of Choices. *Science* **2011**, *334* (6058), 928.
- (8) Winter, M.; Brodd, R. J. What Are Batteries, Fuel Cells, and Supercapacitors? *Chem. Rev.* **2004**, *104* (10), 4245–4270.
- (9) Hadjipaschalidis, I.; Poullikkas, A.; Efthimiou, V. Overview of current and future energy storage technologies for electric power applications. *Renewable Sustainable Energy Rev.* **2009**, *13* (6), 1513–1522.
- (10) Divya, K. C.; Østergaard, J. Battery energy storage technology for power systems—An overview. *Electr. Power Syst. Res.* **2009**, *79* (4), 511–520.
- (11) Yang, Z.; Zhang, J.; Kintner-Meyer, M. C. W.; Lu, X.; Choi, D.; Lemmon, J. P.; Liu, J. Electrochemical Energy Storage for Green Grid. *Chem. Rev.* **2011**, *111* (5), 3577–3613.
- (12) Yabuuchi, N.; Kubota, K.; Dahbi, M.; Komaba, S. Research Development on Sodium-Ion Batteries. *Chem. Rev.* **2014**, *114* (23), 11636–11682.
- (13) Massé, R. C.; Uchaker, E.; Cao, G. Beyond Li-ion: electrode materials for sodium- and magnesium-ion batteries. *Sci. China Mater.* **2015**, *58* (9), 715–766.
- (14) Liu, C.; Neale, Z. G.; Cao, G. Understanding electrochemical potentials of cathode materials in rechargeable batteries. *Mater. Today* **2016**, *19* (2), 109–123.
- (15) Whittingham, M. S. Lithium Batteries and Cathode Materials. *Chem. Rev.* **2004**, *104* (10), 4271–4302.
- (16) Goodenough, J. B.; Kim, Y. Challenges for Rechargeable Li Batteries. *Chem. Mater.* **2010**, *22* (3), 587–603.
- (17) Whittingham, M. S. Ultimate Limits to Intercalation Reactions for Lithium Batteries. *Chem. Rev.* **2014**, *114* (23), 11414–11443.
- (18) Deng, D. Li-ion batteries: basics, progress, and challenges. *Energy Sci. Eng.* **2015**, *3* (5), 385–418.
- (19) Choi, J. W.; Aurbach, D. Promise and reality of post-lithium-ion batteries with high energy densities. *Nat. Rev. Mater.* **2016**, *1*, 16013.
- (20) Nitta, N.; Wu, F.; Lee, J. T.; Yushin, G. Li-ion battery materials: present and future. *Mater. Today* **2015**, *18* (5), 252–264.
- (21) Goodenough, J. B.; Park, K.-S. The Li-Ion Rechargeable Battery: A Perspective. *J. Am. Chem. Soc.* **2013**, *135* (4), 1167–1176.
- (22) Kraysberg, A.; Ein-Eli, Y. Higher, Stronger, Better...□ A Review of 5 V Cathode Materials for Advanced Lithium-Ion Batteries. *Adv. Energy Mater.* **2012**, *2* (8), 922–939.
- (23) Hayner, C. M.; Zhao, X.; Kung, H. H. Materials for Rechargeable Lithium-Ion Batteries. *Annu. Rev. Chem. Biomol. Eng.* **2012**, *3* (1), 445–471.
- (24) Xu, X.; Lee, S.; Jeong, S.; Kim, Y.; Cho, J. Recent progress on nanostructured 4V cathode materials for Li-ion batteries for mobile electronics. *Mater. Today* **2013**, *16* (12), 487–495.

- (25) Dou, S. Review and prospect of layered lithium nickel manganese oxide as cathode materials for Li-ion batteries. *J. Solid State Electrochem.* **2013**, *17* (4), 911–926.
- (26) Marom, R.; Amalraj, S. F.; Leifer, N.; Jacob, D.; Aurbach, D. A review of advanced and practical lithium battery materials. *J. Mater. Chem.* **2011**, *21* (27), 9938–9954.
- (27) Etacheri, V.; Marom, R.; Elazari, R.; Salitra, G.; Aurbach, D. Challenges in the development of advanced Li-ion batteries: a review. *Energy Environ. Sci.* **2011**, *4* (9), 3243–3262.
- (28) Scrosati, B.; Garche, J. Lithium batteries: Status, prospects and future. *J. Power Sources* **2010**, *195* (9), 2419–2430.
- (29) Li, H.; Wang, Z.; Chen, L.; Huang, X. Research on Advanced Materials for Li-ion Batteries. *Adv. Mater.* **2009**, *21* (45), 4593–4607.
- (30) Tarascon, J. M.; Armand, M. Issues and challenges facing rechargeable lithium batteries. *Nature* **2001**, *414*, 359.
- (31) Li, M.; Lu, J.; Chen, Z.; Amine, K. 30 Years of Lithium-Ion Batteries. *Adv. Mater.* **2018**, *30* (33), 1800561.
- (32) Tarascon, J. M. Key challenges in future Li-battery research. *Philos. Trans. R. Soc., A* **2010**, *368* (1923), 3227.
- (33) Manthiram, A. Materials Challenges and Opportunities of Lithium Ion Batteries. *J. Phys. Chem. Lett.* **2011**, *2* (3), 176–184.
- (34) Tian, H.; Xin, F.; Wang, X.; He, W.; Han, W. High capacity group-IV elements (Si, Ge, Sn) based anodes for lithium-ion batteries. *J. Materomics* **2015**, *1* (3), 153–169.
- (35) Fang, C.; Li, J.; Zhang, M.; Zhang, Y.; Yang, F.; Lee, J. Z.; Lee, M.-H.; Alvarado, J.; Schroeder, M. A.; Yang, Y.; Lu, B.; Williams, N.; Ceja, M.; Yang, L.; Cai, M.; Gu, J.; Xu, K.; Wang, X.; Meng, Y. S. Quantifying inactive lithium in lithium metal batteries. *Nature* **2019**, *572* (7770), 511–515.
- (36) Blomgren, G. E. The Development and Future of Lithium Ion Batteries. *J. Electrochem. Soc.* **2017**, *164* (1), A5019–A5025.
- (37) Islam, M. S.; Fisher, C. A. Lithium and sodium battery cathode materials: computational insights into voltage, diffusion and nanostructural properties. *Chem. Soc. Rev.* **2014**, *43* (1), 185–204.
- (38) Rozier, P.; Tarascon, J. M. Review—Li-Rich Layered Oxide Cathodes for Next-Generation Li-Ion Batteries: Chances and Challenges. *J. Electrochem. Soc.* **2015**, *162* (14), A2490–A2499.
- (39) Schipper, F.; Nayak, K. P.; Erickson, M. E.; Amalraj, F. S.; Srur-Lavi, O.; Penki, R. T.; Talianker, M.; Grinblat, J.; Sclar, H.; Breuer, O.; Julien, M. C.; Munichandraiah, N.; Kovacheva, D.; Dixit, M.; Major, T. D.; Markovsky, B.; Aurbach, D. Study of Cathode Materials for Lithium-Ion Batteries: Recent Progress and New Challenges. *Inorganics* **2017**, *5* (2), 32.
- (40) Radin, M. D.; Hy, S.; Sina, M.; Fang, C.; Liu, H.; Vinckeviciute, J.; Zhang, M.; Whittingham, M. S.; Meng, Y. S.; Van der Ven, A. Narrowing the Gap between Theoretical and Practical Capacities in Li-Ion Layered Oxide Cathode Materials. *Adv. Energy Mater.* **2017**, *7* (20), 1602888.
- (41) Meng, Y. S.; Arroyo-de Dompablo, M. E. Recent Advances in First Principles Computational Research of Cathode Materials for Lithium-Ion Batteries. *Acc. Chem. Res.* **2013**, *46* (5), 1171–1180.
- (42) Delmas, C.; Fouassier, C.; Hagenmuller, P. Structural classification and properties of the layered oxides. *Physica B+C* **1980**, *99* (1), 81–85.
- (43) Islam, M. S. Recent atomistic modelling studies of energy materials: batteries included. *Philos. Trans. R. Soc., A* **2010**, *368* (1923), 3255.
- (44) Islam, M. S.; Dominko, R.; Masquelier, C.; Sirisopanaporn, C.; Armstrong, A. R.; Bruce, P. G. Silicate cathodes for lithium batteries: alternatives to phosphates? *J. Mater. Chem.* **2011**, *21* (27), 9811–9818.
- (45) Recham, N.; Chotard, J. N.; Dupont, L.; Delacourt, C.; Walker, W.; Armand, M.; Tarascon, J. M. A 3.6 V lithium-based fluorosulphate insertion positive electrode for lithium-ion batteries. *Nat. Mater.* **2010**, *9*, 68.
- (46) Liu, W.; Oh, P.; Liu, X.; Lee, M.-J.; Cho, W.; Chae, S.; Kim, Y.; Cho, J. Nickel-Rich Layered Lithium Transition-Metal Oxide for High-Energy Lithium-Ion Batteries. *Angew. Chem., Int. Ed.* **2015**, *54* (15), 4440–4457.
- (47) Delmas, C.; Ménétrier, M.; Croguennec, L.; Saadoune, I.; Rougier, A.; Pouillerie, C.; Prado, G.; Grüne, M.; Fournès, L. An overview of the $\text{Li}(\text{Ni}_x\text{M})\text{O}_2$ systems: syntheses, structures and properties. *Electrochim. Acta* **1999**, *45* (1), 243–253.
- (48) Ohzuku, T.; Brodd, R. J. An overview of positive-electrode materials for advanced lithium-ion batteries. *J. Power Sources* **2007**, *174* (2), 449–456.
- (49) He, P.; Yu, H.; Li, D.; Zhou, H. Layered lithium transition metal oxide cathodes towards high energy lithium-ion batteries. *J. Mater. Chem.* **2012**, *22* (9), 3680–3695.
- (50) Myung, S.-T.; Maglia, F.; Park, K.-J.; Yoon, C. S.; Lamp, P.; Kim, S.-J.; Sun, Y.-K. Nickel-Rich Layered Cathode Materials for Automotive Lithium-Ion Batteries: Achievements and Perspectives. *ACS Energy Lett.* **2017**, *2* (1), 196–223.
- (51) Mizushima, K.; Jones, P. C.; Wiseman, P. J.; Goodenough, J. B. Li_xCoO_2 ($0 < x < -1$) A new cathode material for batteries of high energy density. *Mater. Res. Bull.* **1980**, *15* (6), 783–789.
- (52) Nishi, Y. The Dawn of Lithium-Ion Batteries. *Electrochim. Soc. Interface* **2016**, *25* (3), 71–74.
- (53) Whittingham, M. S. Electrical Energy Storage and Intercalation Chemistry. *Science* **1976**, *192* (4244), 1126.
- (54) Whittingham, M. S.; Gamble, F. R. The lithium intercalates of the transition metal dichalcogenides. *Mater. Res. Bull.* **1975**, *10* (5), 363–371.
- (55) Yoshino, A. The Birth of the Lithium-Ion Battery. *Angew. Chem., Int. Ed.* **2012**, *51* (24), 5798–5800.
- (56) Schipper, F.; Erickson, E. M.; Erk, C.; Shin, J.-Y.; Chesneau, F. F.; Aurbach, D. Review—Recent Advances and Remaining Challenges for Lithium Ion Battery Cathodes: I. Nickel-Rich, $\text{LiNi}_x\text{Co}_y\text{Mn}_z\text{O}_2$. *J. Electrochem. Soc.* **2017**, *164* (1), A6220–A6228.
- (57) Li, W.; Reimers, J. N.; Dahn, J. R. Crystal structure of $\text{Li}_x\text{Ni}_{2-x}\text{O}_2$ and a lattice-gas model for the order-disorder transition. *Phys. Rev. B: Condens. Matter Mater. Phys.* **1992**, *46* (6), 3236–3246.
- (58) Ohzuku, T.; Ueda, A.; Nagayama, M. Electrochemistry and Structural Chemistry of LiNiO_2 ($\text{R}\bar{3}\text{m}$) for 4 V Secondary Lithium Cells. *J. Electrochem. Soc.* **1993**, *140* (7), 1862–1870.
- (59) Manthiram, A. An Outlook on Lithium Ion Battery Technology. *ACS Cent. Sci.* **2017**, *3* (10), 1063–1069.
- (60) Bianchini, M.; Roca-Ayats, M.; Hartmann, P.; Brezesinski, T.; Janek, J. There and back again - The journey of LiNiO_2 as cathode active material. *Angew. Chem., Int. Ed.* **2019**, *58*, 10434–10458.
- (61) Thomas, M. G. S. R.; David, W. I. F.; Goodenough, J. B.; Groves, P. Synthesis and structural characterization of the normal spinel $\text{Li}[\text{Ni}_2]\text{O}_4$. *Mater. Res. Bull.* **1985**, *20* (10), 1137–1146.
- (62) Dahn, J. R.; von Sacken, U.; Juzkow, M. W.; Al-Janaby, H. Rechargeable $\text{LiNiO}_2/\text{Carbon}$ Cells. *J. Electrochem. Soc.* **1991**, *138* (8), 2207–2211.
- (63) Armstrong, A. R.; Bruce, P. G. Synthesis of layered LiMnO_2 as an electrode for rechargeable lithium batteries. *Nature* **1996**, *381*, 499.
- (64) Fergus, J. W. Recent developments in cathode materials for lithium ion batteries. *J. Power Sources* **2010**, *195* (4), 939–954.
- (65) Ammundsen, B.; Paulsen, J. Novel Lithium-Ion Cathode Materials Based on Layered Manganese Oxides. *Adv. Mater.* **2001**, *13* (12–13), 943–956.
- (66) Sun, Y.-K.; Jeon, Y.-S.; Leeb, H. J. Overcoming Jahn-Teller Distortion for Spinel Mn Phase. *Electrochim. Solid-State Lett.* **1999**, *3* (1), 7–9.
- (67) Thackeray, M. M. Manganese oxides for lithium batteries. *Prog. Solid State Chem.* **1997**, *25* (1–2), 1–71.
- (68) Komaba, S.; Kumagai, N.; Kataoka, Y. Influence of manganese(II), cobalt(II), and nickel(II) additives in electrolyte on performance of graphite anode for lithium-ion batteries. *Electrochim. Acta* **2002**, *47* (8), 1229–1239.
- (69) Zhecheva, E.; Stoyanova, R. Stabilization of the layered crystal structure of LiNiO_2 by Co-substitution. *Solid State Ionics* **1993**, *66* (1), 143–149.
- (70) Saadoune, I.; Delmas, C. $\text{LiNi}_{1-y}\text{Co}_y\text{O}_2$ positive electrode materials: relationships between the structure, physical properties and electrochemical behaviour. *J. Mater. Chem.* **1996**, *6* (2), 193–199.

- (71) Ohzuku, T.; Makimura, Y. Layered Lithium Insertion Material of $\text{LiCo}_{1/3}\text{Ni}_{1/3}\text{Mn}_{1/3}\text{O}_2$ for Lithium-Ion Batteries. *Chem. Lett.* **2001**, *30* (7), 642–643.
- (72) Noh, H.-J.; Youn, S.; Yoon, C. S.; Sun, Y.-K. Comparison of the structural and electrochemical properties of layered $\text{Li}[\text{Ni}_x\text{Co}_y\text{Mn}_z]\text{O}_2$ ($x = 1/3, 0.5, 0.6, 0.7, 0.8$ and 0.85) cathode material for lithium-ion batteries. *J. Power Sources* **2013**, *233*, 121–130.
- (73) Zeng, X.; Li, M.; Abd El-Hady, D.; Alshitari, W.; Al-Bogami, A. S.; Lu, J.; Amine, K. Commercialization of Lithium Battery Technologies for Electric Vehicles. *Adv. Energy Mater.* **2019**, *9* (27), 1900161.
- (74) Choi, J.; Manthiram, A. Role of Chemical and Structural Stabilities on the Electrochemical Properties of Layered $\text{Li-Ni}_{1/3}\text{Co}_{1/3}\text{Mn}_{1/3}\text{O}_2$ Cathodes. *J. Electrochem. Soc.* **2005**, *152* (9), A1714–A1718.
- (75) de Biasi, L.; Kondrakov, A. O.; Geßwein, H.; Brezesinski, T.; Hartmann, P.; Janek, J. Between Scylla and Charybdis: Balancing Among Structural Stability and Energy Density of Layered NCM Cathode Materials for Advanced Lithium-Ion Batteries. *J. Phys. Chem. C* **2017**, *121* (47), 26163–26171.
- (76) Jung, R.; Metzger, M.; Maglia, F.; Stinner, C.; Gasteiger, H. A. Oxygen Release and Its Effect on the Cycling Stability of $\text{LiNi}_x\text{Mn}_y\text{Co}_z\text{O}_2$ (NMC) Cathode Materials for Li-Ion Batteries. *J. Electrochem. Soc.* **2017**, *164* (7), A1361–A1377.
- (77) Jung, S.-K.; Gwon, H.; Hong, J.; Park, K.-Y.; Seo, D.-H.; Kim, H.; Hyun, J.; Yang, W.; Kang, K. Understanding the Degradation Mechanisms of $\text{LiNi}_{0.5}\text{Co}_{0.2}\text{Mn}_{0.3}\text{O}_2$ Cathode Material in Lithium Ion Batteries. *Adv. Energy Mater.* **2014**, *4* (1), 1300787.
- (78) Breuer, O.; Chakraborty, A.; Liu, J.; Kravchuk, T.; Burstein, L.; Grinblat, J.; Kauffman, Y.; Gladikh, A.; Nayak, P.; Tsubery, M.; Frenkel, A. I.; Talianker, M.; Major, D. T.; Markovsky, B.; Aurbach, D. Understanding the Role of Minor Molybdenum Doping in $\text{LiNi}_{0.5}\text{Co}_{0.2}\text{Mn}_{0.3}\text{O}_2$ Electrodes: from Structural and Surface Analyses and Theoretical Modeling to Practical Electrochemical Cells. *ACS Appl. Mater. Interfaces* **2018**, *10* (35), 29608–29621.
- (79) Gilbert, J. A.; Bareño, J.; Spila, T.; Trask, S. E.; Miller, D. J.; Polzin, B. J.; Jansen, A. N.; Abraham, D. P. Cycling Behavior of NCM523/Graphite Lithium-Ion Cells in the 3–4.4 V Range: Diagnostic Studies of Full Cells and Harvested Electrodes. *J. Electrochem. Soc.* **2017**, *164* (1), A6054–A6065.
- (80) Bang, H.; Kim, D.-H.; Bae, Y. C.; Prakash, J.; Sun, Y.-K. Effects of Metal Ions on the Structural and Thermal Stabilities of $\text{Li}[\text{Ni}_{1-x-y}\text{Co}_x\text{Mn}_y]\text{O}_2$ ($x + y = 0.5$) Studied by In Situ High Temperature XRD. *J. Electrochem. Soc.* **2008**, *155* (12), A952–A958.
- (81) Kim, M.-H.; Shin, H.-S.; Shin, D.; Sun, Y.-K. Synthesis and electrochemical properties of $\text{Li}[\text{Ni}_{0.8}\text{Co}_{0.1}\text{Mn}_{0.1}]\text{O}_2$ and $\text{Li}[\text{Ni}_{0.8}\text{Co}_{0.2}]\text{O}_2$ via co-precipitation. *J. Power Sources* **2006**, *159* (2), 1328–1333.
- (82) Neudeck, S.; Strauss, F.; Garcia, G.; Wolf, H.; Janek, J.; Hartmann, P.; Brezesinski, T. Room temperature, liquid-phase Al_2O_3 surface coating approach for Ni-rich layered oxide cathode material. *Chem. Commun.* **2019**, *55* (15), 2174–2177.
- (83) Song, C.; Wang, W.; Peng, H.; Wang, Y.; Zhao, C.; Zhang, H.; Tang, Q.; Lv, J.; Du, X.; Dou, Y. Improving the Electrochemical Performance of $\text{LiNi}_{0.80}\text{Co}_{0.15}\text{Al}_{0.05}\text{O}_2$ in Lithium Ion Batteries by LiAlO_2 Surface Modification. *Appl. Sci.* **2018**, *8* (3), 378.
- (84) Susai, F. A.; Sclar, H.; Shilina, Y.; Penki, T. R.; Raman, R.; Maddukuri, S.; Maiti, S.; Halalay, I. C.; Luski, S.; Markovsky, B.; Aurbach, D. Horizons for Li-Ion Batteries Relevant to Electro-Mobility: High-Specific-Energy Cathodes and Chemically Active Separators. *Adv. Mater.* **2018**, *30* (41), 1801348.
- (85) Dixit, M.; Kosa, M.; Lavi, O. S.; Markovsky, B.; Aurbach, D.; Major, D. T. Thermodynamic and kinetic studies of $\text{Li-Ni}_{0.5}\text{Co}_{0.2}\text{Mn}_{0.3}\text{O}_2$ as a positive electrode material for Li-ion batteries using first principles. *Phys. Chem. Chem. Phys.* **2016**, *18* (9), 6799–6812.
- (86) Dixit, M.; Markovsky, B.; Schipper, F.; Aurbach, D.; Major, D. T. Origin of Structural Degradation During Cycling and Low Thermal Stability of Ni-Rich Layered Transition Metal-Based Electrode Materials. *J. Phys. Chem. C* **2017**, *121* (41), 22628–22636.
- (87) Schipper, F.; Dixit, M.; Kovacheva, D.; Talianker, M.; Haik, O.; Grinblat, J.; Erickson, E. M.; Ghanty, C.; Major, D. T.; Markovsky, B.; Aurbach, D. Stabilizing nickel-rich layered cathode materials by a high-charge cation doping strategy: zirconium-doped $\text{Li-Ni}_{0.6}\text{Co}_{0.2}\text{Mn}_{0.2}\text{O}_2$. *J. Mater. Chem. A* **2016**, *4* (41), 16073–16084.
- (88) Xu, J.; Lin, F.; Doeff, M. M.; Tong, W. A review of Ni-based layered oxides for rechargeable Li-ion batteries. *J. Mater. Chem. A* **2017**, *5* (3), 874–901.
- (89) Guilmard, M.; Croguennec, L.; Delmas, C. Thermal Stability of Lithium Nickel Oxide Derivatives. Part II: $\text{Li}_{x}\text{Ni}_{0.70}\text{Co}_{0.15}\text{Al}_{0.15}\text{O}_2$ and $\text{Li}_{x}\text{Ni}_{0.90}\text{Mn}_{0.10}\text{O}_2$ ($x = 0.50$ and 0.30). Comparison with $\text{Li}_{x}\text{Ni}_{1.02}\text{O}_2$ and $\text{Li}_{x}\text{Ni}_{0.89}\text{Al}_{0.16}\text{O}_2$. *Chem. Mater.* **2003**, *15* (23), 4484–4493.
- (90) Guilmard, M.; Croguennec, L.; Denux, D.; Delmas, C. Thermal Stability of Lithium Nickel Oxide Derivatives. Part I: $\text{Li}_{x}\text{Ni}_{1.02}\text{O}_2$ and $\text{Li}_{x}\text{Ni}_{0.89}\text{Al}_{0.16}\text{O}_2$ ($x = 0.50$ and 0.30). *Chem. Mater.* **2003**, *15* (23), 4476–4483.
- (91) Dixit, M.; Markovsky, B.; Aurbach, D.; Major, D. T. Unraveling the Effects of Al Doping on the Electrochemical Properties of $\text{LiNi}_{0.5}\text{Co}_{0.2}\text{Mn}_{0.3}\text{O}_2$ Using First Principles. *J. Electrochem. Soc.* **2017**, *164* (1), A6359–A6365.
- (92) Schipper, F.; Bouzaglo, H.; Dixit, M.; Erickson, E. M.; Weigel, T.; Talianker, M.; Grinblat, J.; Burstein, L.; Schmidt, M.; Lampert, J.; Erk, C.; Markovsky, B.; Major, D. T.; Aurbach, D. From Surface ZrO_2 Coating to Bulk Zr Doping by High Temperature Annealing of Nickel-Rich Lithiated Oxides and Their Enhanced Electrochemical Performance in Lithium Ion Batteries. *Adv. Energy Mater.* **2018**, *8* (4), 1701682.
- (93) Kim, U. H.; Jun, D. W.; Park, K. J.; Zhang, Q.; Kaghazchi, P.; Aurbach, D.; Major, D. T.; Goobes, G.; Dixit, M.; Leifer, N.; Wang, C. M.; Yan, P.; Ahn, D.; Kim, K. H.; Yoon, C. S.; Sun, Y. K. Pushing the limit of layered transition metal oxide cathodes for high-energy density rechargeable Li ion batteries. *Energy Environ. Sci.* **2018**, *11* (5), 1271–1279.
- (94) Kim, J.; Amine, K. A comparative study on the substitution of divalent, trivalent and tetravalent metal ions in $\text{LiNi}_{1-x}\text{M}_x\text{O}_2$ ($\text{M} = \text{Cu}^{2+}, \text{Al}^{3+}$ and Ti^{4+}). *J. Power Sources* **2002**, *104* (1), 33–39.
- (95) Zhang, J.-N.; Li, Q.; Ouyang, C.; Yu, X.; Ge, M.; Huang, X.; Hu, E.; Ma, C.; Li, S.; Xiao, R.; Yang, W.; Chu, Y.; Liu, Y.; Yu, H.; Yang, X.-Q.; Huang, X.; Chen, L.; Li, H. Trace doping of multiple elements enables stable battery cycling of LiCoO_2 at 4.6 V. *Nat. Energy* **2019**, *4* (7), 594–603.
- (96) Liu, Q.; Su, X.; Lei, D.; Qin, Y.; Wen, J.; Guo, F.; Wu, Y. A.; Rong, Y.; Kou, R.; Xiao, X.; Aguesse, F.; Bareño, J.; Ren, Y.; Lu, W.; Li, Y. Approaching the capacity limit of lithium cobalt oxide in lithium ion batteries via lanthanum and aluminium doping. *Nat. Energy* **2018**, *3* (11), 936–943.
- (97) Lee, S.; Park, S. S. Atomistic Simulation Study of Mixed-Metal Oxide ($\text{LiNi}_{1/3}\text{Co}_{1/3}\text{Mn}_{1/3}\text{O}_2$) Cathode Material for Lithium Ion Battery. *J. Phys. Chem. C* **2012**, *116* (10), 6484–6489.
- (98) Croguennec, L.; Shao-Horn, Y.; Gloter, A.; Colliex, C.; Guilmard, M.; Fauth, F.; Delmas, C. Segregation Tendency in Layered Aluminum-Substituted Lithium Nickel Oxides. *Chem. Mater.* **2009**, *21* (6), 1051–1059.
- (99) Jain, A.; Shin, Y.; Persson, K. A. Computational predictions of energy materials using density functional theory. *Nat. Rev. Mater.* **2016**, *1*, 15004.
- (100) Urban, A.; Seo, D.-H.; Ceder, G. Computational understanding of Li-ion batteries. *npj Comput. Mater.* **2016**, *2*, 16002.
- (101) Chevrier, V. L.; Dahn, J. R. First Principles Studies of Disordered Lithiated Silicon. *J. Electrochem. Soc.* **2010**, *157* (4), A392–A398.
- (102) Persson, K.; Sethuraman, V. A.; Hardwick, L. J.; Hinuma, Y.; Meng, Y. S.; van der Ven, A.; Srinivasan, V.; Kostecki, R.; Ceder, G. Lithium Diffusion in Graphitic Carbon. *J. Phys. Chem. Lett.* **2010**, *1* (8), 1176–1180.
- (103) Chan, M. K. Y.; Wolverton, C.; Greeley, J. P. First Principles Simulations of the Electrochemical Lithiation and Delithiation of

- Faceted Crystalline Silicon. *J. Am. Chem. Soc.* **2012**, *134* (35), 14362–14374.
- (104) Kirklin, S.; Meredig, B.; Wolverton, C. High-Throughput Computational Screening of New Li-Ion Battery Anode Materials. *Adv. Energy Mater.* **2013**, *3* (2), 252–262.
- (105) Mo, Y.; Ong, S. P.; Ceder, G. First Principles Study of the $\text{Li}_{10}\text{GeP}_2\text{S}_{12}$ Lithium Super Ionic Conductor Material. *Chem. Mater.* **2012**, *24* (1), 15–17.
- (106) Wang, Y.; Richards, W. D.; Ong, S. P.; Miara, L. J.; Kim, J. C.; Mo, Y.; Ceder, G. Design principles for solid-state lithium superionic conductors. *Nat. Mater.* **2015**, *14*, 1026.
- (107) Richards, W. D.; Miara, L. J.; Wang, Y.; Kim, J. C.; Ceder, G. Interface Stability in Solid-State Batteries. *Chem. Mater.* **2016**, *28* (1), 266–273.
- (108) Aykol, M.; Kirklin, S.; Wolverton, C. Thermodynamic Aspects of Cathode Coatings for Lithium-Ion Batteries. *Adv. Energy Mater.* **2014**, *4* (17), 1400690.
- (109) Aydinol, M. K.; Kohan, A. F.; Ceder, G.; Cho, K.; Joannopoulos, J. Ab initio study of lithium intercalation in metal oxides and metal dichalcogenides. *Phys. Rev. B: Condens. Matter Mater. Phys.* **1997**, *56* (3), 1354–1365.
- (110) Aydinol, M. K.; Kohan, A. F.; Ceder, G. Ab initio calculation of the intercalation voltage of lithium-transition-metal oxide electrodes for rechargeable batteries. *J. Power Sources* **1997**, *68* (2), 664–668.
- (111) Benco, L. u. r.; Barras, J.-L.; Atanasov, M.; Daul, C. A.; Deiss, E. First-principles prediction of voltages of lithiated oxides for lithium-ion batteries. *Solid State Ionics* **1998**, *112* (3), 255–259.
- (112) Jain, A.; Hautier, G.; Moore, C. J.; Ping Ong, S.; Fischer, C. C.; Mueller, T.; Persson, K. A.; Ceder, G. A high-throughput infrastructure for density functional theory calculations. *Comput. Mater. Sci.* **2011**, *50* (8), 2295–2310.
- (113) Mueller, T.; Hautier, G.; Jain, A.; Ceder, G. Evaluation of Tavorite-Structured Cathode Materials for Lithium-Ion Batteries Using High-Throughput Computing. *Chem. Mater.* **2011**, *23* (17), 3854–3862.
- (114) Meng, Y. S.; Arroyo-de Dompablo, M. E. First principles computational materials design for energy storage materials in lithium ion batteries. *Energy Environ. Sci.* **2009**, *2* (6), 589–609.
- (115) Van der Ven, A.; Thomas, J. C.; Xu, Q.; Swoboda, B.; Morgan, D. Nondilute diffusion from first principles: Li diffusion in Li_xTiS_2 . *Phys. Rev. B: Condens. Matter Mater. Phys.* **2008**, *78* (10), 104306.
- (116) Van der Ven, A.; Ceder, G. Lithium diffusion mechanisms in layered intercalation compounds. *J. Power Sources* **2001**, *97*–*98*, 529–531.
- (117) Wei, Y.; Zheng, J.; Cui, S.; Song, X.; Su, Y.; Deng, W.; Wu, Z.; Wang, X.; Wang, W.; Rao, M.; Lin, Y.; Wang, C.; Amine, K.; Pan, F. Kinetics Tuning of Li-Ion Diffusion in Layered $\text{Li}(\text{Ni}_x\text{Mn}_y\text{Co}_z)\text{O}_2$. *J. Am. Chem. Soc.* **2015**, *137* (26), 8364–8367.
- (118) Kang, K.; Meng, Y. S.; Bréger, J.; Grey, C. P.; Ceder, G. Electrodes with High Power and High Capacity for Rechargeable Lithium Batteries. *Science* **2006**, *311* (5763), 977–980.
- (119) Curtarolo, S.; Hart, G. L. W.; Nardelli, M. B.; Mingo, N.; Sanvito, S.; Levy, O. The high-throughput highway to computational materials design. *Nat. Mater.* **2013**, *12*, 191.
- (120) Hautier, G.; Jain, A.; Ong, S. P. From the computer to the laboratory: materials discovery and design using first-principles calculations. *J. Mater. Sci.* **2012**, *47* (21), 7317–7340.
- (121) Hautier, G. Prediction of new battery materials based on ab initio computations. *AIP Conf. Proc.* **2015**, *1765*, 020009.
- (122) Hohenberg, P.; Kohn, W. Inhomogeneous Electron Gas. *Phys. Rev.* **1964**, *136* (3B), B864–B871.
- (123) Kohn, W.; Sham, L. J. Self-Consistent Equations Including Exchange and Correlation Effects. *Phys. Rev.* **1965**, *140* (4A), A1133–A1138.
- (124) Burke, K.; Wagner, L. O. DFT in a nutshell. *Int. J. Quantum Chem.* **2013**, *113* (2), 96–101.
- (125) Perdew, J. P.; Ruzsinszky, A.; Constantin, L. A.; Sun, J.; Csonka, G. I. Some Fundamental Issues in Ground-State Density Functional Theory: A Guide for the Perplexed. *J. Chem. Theory Comput.* **2009**, *5* (4), 902–908.
- (126) Perdew, J. P.; Schmidt, K. Jacob's ladder of density functional approximations for the exchange-correlation energy. *AIP Conf. Proc.* **2000**, *577* (1), 1–20.
- (127) Perdew, J. P.; Chevary, J. A.; Vosko, S. H.; Jackson, K. A.; Pederson, M. R.; Singh, D. J.; Fiolhais, C. Atoms, molecules, solids, and surfaces: Applications of the generalized gradient approximation for exchange and correlation. *Phys. Rev. B: Condens. Matter Mater. Phys.* **1992**, *46* (11), 6671–6687.
- (128) Stoyanova, R.; Zhecheva, E.; Alcántara, R.; Tirado, J. L.; Bromiley, G.; Bromiley, F.; Boffa Ballaran, T. Lithium/nickel mixing in the transition metal layers of lithium nickelate: high-pressure synthesis of layered $\text{Li}[\text{Li}_x\text{Ni}_{1-x}]\text{O}_2$ oxides as cathode materials for lithium-ion batteries. *Solid State Ionics* **2003**, *161* (3), 197–204.
- (129) Hao, P.; Sun, J.; Xiao, B.; Ruzsinszky, A.; Csonka, G. I.; Tao, J.; Glindmeyer, S.; Perdew, J. P. Performance of meta-GGA Functionals on General Main Group Thermochemistry, Kinetics, and Noncovalent Interactions. *J. Chem. Theory Comput.* **2013**, *9* (1), 355–363.
- (130) Becke, A. D. A new mixing of Hartree–Fock and local density-functional theories. *J. Chem. Phys.* **1993**, *98* (2), 1372–1377.
- (131) Becke, A. D. Density-functional exchange-energy approximation with correct asymptotic behavior. *Phys. Rev. A: At., Mol., Opt. Phys.* **1988**, *38* (6), 3098–3100.
- (132) Grimme, S. Semiempirical hybrid density functional with perturbative second-order correlation. *J. Chem. Phys.* **2006**, *124* (3), 034108.
- (133) Perdew, J. P.; Burke, K.; Ernzerhof, M. Generalized Gradient Approximation Made Simple. *Phys. Rev. Lett.* **1996**, *77* (18), 3865–3868.
- (134) Liechtenstein, A. I.; Anisimov, V. I.; Zaanen, J. Density-functional theory and strong interactions: Orbital ordering in Mott-Hubbard insulators. *Phys. Rev. B: Condens. Matter Mater. Phys.* **1995**, *52* (8), R5467–R5470.
- (135) Dudarev, S. L.; Botton, G. A.; Savrasov, S. Y.; Humphreys, C. J.; Sutton, A. P. Electron-energy-loss spectra and the structural stability of nickel oxide: An LSDA+U study. *Phys. Rev. B: Condens. Matter Mater. Phys.* **1998**, *57* (3), 1505–1509.
- (136) Himmetoglu, B.; Floris, A.; de Gironcoli, S.; Cococcioni, M. Hubbard-corrected DFT energy functionals: The LDA+U description of correlated systems. *Int. J. Quantum Chem.* **2014**, *114* (1), 14–49.
- (137) Kulik, H. J.; Marzari, N. A self-consistent Hubbard U density-functional theory approach to the addition-elimination reactions of hydrocarbons on bare FeO^+ . *J. Chem. Phys.* **2008**, *129* (13), 134314.
- (138) Chakraborty, A.; Dixit, M.; Aurbach, D.; Major, D. T. Predicting accurate cathode properties of layered oxide materials using the SCAN meta-GGA density functional. *npj Comput. Mater.* **2018**, *4* (1), 60.
- (139) Kulik, H. J.; Marzari, N. Accurate potential energy surfaces with a DFT+U(R) approach. *J. Chem. Phys.* **2011**, *135* (19), 194105.
- (140) Cococcioni, M.; Marzari, N. Energetics and cathode voltages of LiMPO_4 olivines ($M = \text{Fe}, \text{Mn}$) from extended Hubbard functionals. *Phys. Rev. Mater.* **2019**, *3* (3), 033801.
- (141) Grimme, S. Density functional theory with London dispersion corrections. *Wiley Interdiscip. Rev. Comput. Mol. Sci.* **2011**, *1* (2), 211–228.
- (142) Grimme, S. Accurate description of van der Waals complexes by density functional theory including empirical corrections. *J. Comput. Chem.* **2004**, *25* (12), 1463–1473.
- (143) Grimme, S. Semiempirical GGA-type density functional constructed with a long-range dispersion correction. *J. Comput. Chem.* **2006**, *27* (15), 1787–1799.
- (144) Grimme, S.; Antony, J.; Ehrlich, S.; Krieg, H. A consistent and accurate ab initio parametrization of density functional dispersion correction (DFT-D) for the 94 elements H–Pu. *J. Chem. Phys.* **2010**, *132* (15), 154104.

- (145) Tkatchenko, A.; Scheffler, M. Accurate Molecular Van Der Waals Interactions from Ground-State Electron Density and Free-Atom Reference Data. *Phys. Rev. Lett.* **2009**, *102* (7), 073005.
- (146) Sun, J.; Remsing, R. C.; Zhang, Y.; Sun, Z.; Ruzsinszky, A.; Peng, H.; Yang, Z.; Paul, A.; Waghmare, U.; Wu, X.; Klein, M. L.; Perdew, J. P. Accurate first-principles structures and energies of diversely bonded systems from an efficient density functional. *Nat. Chem.* **2016**, *8*, 831.
- (147) Blöchl, P. E. Projector augmented-wave method. *Phys. Rev. B: Condens. Matter Mater. Phys.* **1994**, *50* (24), 17953–17979.
- (148) Giannozzi, P.; Andreussi, O.; Brumme, T.; Bunau, O.; Buongiorno Nardelli, M.; Calandra, M.; Car, R.; Cavazzoni, C.; Ceresoli, D.; Cococcioni, M.; Colonna, N.; Carnimeo, I.; Dal Corso, A.; de Gironcoli, S.; Delugas, P.; DiStasio, R. A.; Ferretti, A.; Floris, A.; Fratesi, G.; Fugallo, G.; Gebauer, R.; Gerstmann, U.; Giustino, F.; Gorni, T.; Jia, J.; Kawamura, M.; Ko, H. Y.; Kokalj, A.; Küçükbenli, E.; Lazzeri, M.; Marsili, M.; Marzari, N.; Mauri, F.; Nguyen, N. L.; Nguyen, H. V.; Otero-de-la-Roza, A.; Paulatto, L.; Poncé, S.; Rocca, D.; Sabatini, R.; Santra, B.; Schlipf, M.; Seitsonen, A. P.; Smogunov, A.; Timrov, I.; Thonhauser, T.; Umari, P.; Vast, N.; Wu, X.; Baroni, S. Advanced capabilities for materials modelling with Q quantum ESPRESSO. *J. Phys.: Condens. Matter* **2017**, *29* (46), 465901.
- (149) Gonze, X.; Beuken, J. M.; Caracas, R.; Detraux, F.; Fuchs, M.; Rignanese, G. M.; Sindic, L.; Verstraete, M.; Zerah, G.; Jollet, F.; Torrent, M.; Roy, A.; Mikami, M.; Ghosez, P.; Raty, J. Y.; Allan, D. C. First-principles computation of material properties: the ABINIT software project. *Comput. Mater. Sci.* **2002**, *25* (3), 478–492.
- (150) Gonze, X.; Amadon, B.; Anglade, P. M.; Beuken, J. M.; Bottin, F.; Boulanger, P.; Bruneval, F.; Caliste, D.; Caracas, R.; Côté, M.; Deutsch, T.; Genovese, L.; Ghosez, P.; Giantomassi, M.; Goedecker, S.; Hamann, D. R.; Hermet, P.; Jollet, F.; Jomard, G.; Leroux, S.; Mancini, M.; Mazevert, S.; Oliveira, M. J. T.; Onida, G.; Pouillon, Y.; Rangel, T.; Rignanese, G. M.; Sangalli, D.; Shaltaf, R.; Torrent, M.; Verstraete, M. J.; Zerah, G.; Zwanziger, J. W. ABINIT: First-principles approach to material and nanosystem properties. *Comput. Phys. Commun.* **2009**, *180* (12), 2582–2615.
- (151) Clark, S. J.; Segall, M. D.; Pickard, C. J.; Hasnip, P. J.; Probert, M. I. J.; Refson, K.; Payne, M. C. First principles methods using CASTEP. *Z. Kristallogr. - Cryst. Mater.* **2005**, *220*, 567.
- (152) Kresse, G.; Furthmüller, J. Efficiency of ab-initio total energy calculations for metals and semiconductors using a plane-wave basis set. *Comput. Mater. Sci.* **1996**, *6* (1), 15–50.
- (153) Kresse, G.; Hafner, J. Ab initio molecular dynamics for liquid metals. *Phys. Rev. B: Condens. Matter Mater. Phys.* **1993**, *47* (1), 558–561.
- (154) Kresse, G.; Hafner, J. Ab initio molecular-dynamics simulation of the liquid-metal–amorphous-semiconductor transition in germanium. *Phys. Rev. B: Condens. Matter Mater. Phys.* **1994**, *49* (20), 14251–14269.
- (155) Feynman, R. P. Forces in Molecules. *Phys. Rev.* **1939**, *56* (4), 340–343.
- (156) Hwang, B. J.; Tsai, Y. W.; Carlier, D.; Ceder, G. A Combined Computational/Experimental Study on LiNi_{1/3}Co_{1/3}Mn_{1/3}O₂. *Chem. Mater.* **2003**, *15* (19), 3676–3682.
- (157) Liang, C.; Kong, F.; Longo, R. C.; Kc, S.; Kim, J.-S.; Jeon, S.; Choi, S.; Cho, K. Unraveling the Origin of Instability in Ni-Rich LiNi_{1-2x}Co_xMn_xO₂ (NCM) Cathode Materials. *J. Phys. Chem. C* **2016**, *120* (12), 6383–6393.
- (158) Dogan, F.; Vaughey, J. T.; Iddir, H.; Key, B. Direct Observation of Lattice Aluminum Environments in Li Ion Cathodes LiNi_{1-y-z}Co_yAl_zO₂ and Al-Doped LiNi_xMn_yCo_zO₂ via ²⁷Al MAS NMR Spectroscopy. *ACS Appl. Mater. Interfaces* **2016**, *8* (26), 16708–16717.
- (159) Tang, W.; Sanville, E.; Henkelman, G. A grid-based Bader analysis algorithm without lattice bias. *J. Phys.: Condens. Matter* **2009**, *21* (8), 084204.
- (160) Deringer, V. L.; Tchougréeff, A. L.; Dronskowski, R. Crystal Orbital Hamilton Population (COHP) Analysis As Projected from Plane-Wave Basis Sets. *J. Phys. Chem. A* **2011**, *115* (21), 5461–5466.
- (161) Dronskowski, R.; Bloechl, P. E. Crystal orbital Hamilton populations (COHP): energy-resolved visualization of chemical bonding in solids based on density-functional calculations. *J. Phys. Chem.* **1993**, *97* (33), 8617–8624.
- (162) Maintz, S.; Deringer, V. L.; Tchougréeff, A. L.; Dronskowski, R. Analytic projection from plane-wave and PAW wavefunctions and application to chemical-bonding analysis in solids. *J. Comput. Chem.* **2013**, *34* (29), 2557–2567.
- (163) van de Walle, A.; Asta, M.; Ceder, G. The alloy theoretic automated toolkit: A user guide. *CALPHAD: Comput. Coupling Phase Diagrams Thermochem.* **2002**, *26* (4), 539–553.
- (164) van de Walle, A. Multicomponent multisublattice alloys, nonconfigurational entropy and other additions to the Alloy Theoretic Automated Toolkit. *CALPHAD: Comput. Coupling Phase Diagrams Thermochem.* **2009**, *33* (2), 266–278.
- (165) Van der Ven, A.; Thomas, J. C.; Xu, Q.; Bhattacharya, J. Linking the electronic structure of solids to their thermodynamic and kinetic properties. *Math. Comput. Simul.* **2010**, *80* (7), 1393–1410.
- (166) Puchala, B.; Van der Ven, A. Thermodynamics of the Zr-O system from first-principles calculations. *Phys. Rev. B: Condens. Matter Mater. Phys.* **2013**, *88* (9), 094108.
- (167) Thomas, J. C.; Ven, A. V. d. Finite-temperature properties of strongly anharmonic and mechanically unstable crystal phases from first principles. *Phys. Rev. B: Condens. Matter Mater. Phys.* **2013**, *88* (21), 214111.
- (168) Abdellahi, A.; Urban, A.; Dacek, S.; Ceder, G. Understanding the Effect of Cation Disorder on the Voltage Profile of Lithium Transition-Metal Oxides. *Chem. Mater.* **2016**, *28* (15), 5373–5383.
- (169) Trease, N. M.; Seymour, I. D.; Radin, M. D.; Liu, H.; Liu, H.; Hy, S.; Chernova, N.; Parikh, P.; Devaraj, A.; Wiaderek, K. M.; Chupas, P. J.; Chapman, K. W.; Whittingham, M. S.; Meng, Y. S.; Van der Van, A.; Grey, C. P. Identifying the Distribution of Al³⁺ in LiNi_{0.8}Co_{0.15}Al_{0.05}O₂. *Chem. Mater.* **2016**, *28* (22), 8170–8180.
- (170) Ratcliff, L. E.; Mohr, S.; Huhs, G.; Deutsch, T.; Masella, M.; Genovese, L. Challenges in large scale quantum mechanical calculations. *Wiley Interdiscip. Rev. Comput. Mol. Sci.* **2017**, *7* (1), e1290.
- (171) Zhang, X.; Lu, G. Coupled quantum mechanics/molecular mechanics modeling of metallic materials: Theory and applications. *J. Mater. Res.* **2018**, *33* (7), 796–812.
- (172) Bernstein, N.; Kermode, J. R.; Csányi, G. Hybrid atomistic simulation methods for materials systems. *Rep. Prog. Phys.* **2009**, *72* (2), 026501.
- (173) Shi, S.; Gao, J.; Liu, Y.; Zhao, Y.; Wu, Q.; Ju, W.; Ouyang, C.; Xiao, R. Multi-scale computation methods: Their applications in lithium-ion battery research and development. *Chin. Phys. B* **2016**, *25* (1), 018212.
- (174) Lifson, S.; Warshel, A. Consistent Force Field for Calculations of Conformations, Vibrational Spectra, and Enthalpies of Cycloalkane and n-Alkane Molecules. *J. Chem. Phys.* **1968**, *49* (11), 5116–5129.
- (175) Applequist, J. A multipole interaction theory of electric polarization of atomic and molecular assemblies. *J. Chem. Phys.* **1985**, *83* (2), 809–826.
- (176) Dick, B. G.; Overhauser, A. W. Theory of the Dielectric Constants of Alkali Halide Crystals. *Phys. Rev.* **1958**, *112* (1), 90–103.
- (177) Fisher, C. A. J.; Hart Prieto, V. M.; Islam, M. S. Lithium Battery Materials LiMPO₄ (M = Mn, Fe, Co, and Ni): Insights into Defect Association, Transport Mechanisms, and Doping Behavior. *Chem. Mater.* **2008**, *20* (18), 5907–5915.
- (178) Gale, J. D.; Rohl, A. L. The General Utility Lattice Program (GULP). *Mol. Simul.* **2003**, *29* (5), 291–341.
- (179) Smith, W.; Yong, C. W.; Rodger, P. M. DL_POLY: Application to molecular simulation. *Mol. Simul.* **2002**, *28* (5), 385–471.
- (180) Lee, E.; Lee, K.-R.; Lee, B.-J. Interatomic Potential of Li–Mn–O and Molecular Dynamics Simulations on Li Diffusion in Spinel Li_{1-x}Mn₂O₄. *J. Phys. Chem. C* **2017**, *121* (24), 13008–13017.
- (181) Lee, E.; Lee, K.-R.; Lee, B.-J. An interatomic potential for the Li–Co–O ternary system. *Comput. Mater. Sci.* **2018**, *142*, 47–58.

- (182) Henkelman, G.; Uberuaga, B. P.; Jónsson, H. A climbing image nudged elastic band method for finding saddle points and minimum energy paths. *J. Chem. Phys.* **2000**, *113* (22), 9901–9904.
- (183) Li, Z.; Wang, C.; Ma, X.; Yuan, L.; Sun, J. Synthesis, structures and electrochemical properties of $\text{Li}_x\text{Ni}_{1-x}\text{O}$. *Mater. Chem. Phys.* **2005**, *91* (1), 36–39.
- (184) Koyama, Y.; Tanaka, I.; Adachi, H.; Makimura, Y.; Ohzuku, T. Crystal and electronic structures of superstructural $\text{Li}_{1-x}[\text{Co}_{1/3}\text{Ni}_{1/3}\text{Mn}_{1/3}]\text{O}_2$ ($0 \leq x \leq 1$). *J. Power Sources* **2003**, *119–121*, 644–648.
- (185) Cahill, L. S.; Yin, S. C.; Samoson, A.; Heinmaa, I.; Nazar, L. F.; Goward, G. R. ^6Li NMR Studies of Cation Disorder and Transition Metal Ordering in $\text{Li}[\text{Ni}_{1/3}\text{Mn}_{1/3}\text{Co}_{1/3}]\text{O}_2$ Using Ultrafast Magic Angle Spinning. *Chem. Mater.* **2005**, *17* (26), 6560–6566.
- (186) Zeng, D.; Cabana, J.; Bréger, J.; Yoon, W.-S.; Grey, C. P. Cation Ordering in $\text{Li}[\text{Ni}_x\text{Mn}_x\text{Co}_{(1-2x)}]\text{O}_2$ -Layered Cathode Materials: A Nuclear Magnetic Resonance (NMR), Pair Distribution Function, X-ray Absorption Spectroscopy, and Electrochemical Study. *Chem. Mater.* **2007**, *19* (25), 6277–6289.
- (187) Weill, F.; Tran, N.; Croguennec, L.; Delmas, C. Cation ordering in the layered $\text{Li}_{1+x}(\text{Ni}_{0.425}\text{Mn}_{0.425}\text{Co}_{0.15})_{1-x}\text{O}_2$ materials ($x = 0$ and 0.12). *J. Power Sources* **2007**, *172* (2), 893–900.
- (188) Meng, Y. S.; Ceder, G.; Grey, C. P.; Yoon, W. S.; Jiang, M.; Bréger, J.; Shao-Horn, Y. Cation Ordering in Layered O₃ $\text{Li}[\text{Ni}_x\text{Li}_{1/3-2x/3}\text{Mn}_{2/3-x/3}]\text{O}_2$ ($0 \leq x \leq 1/2$) Compounds. *Chem. Mater.* **2005**, *17* (9), 2386–2394.
- (189) Yu, H.; Qian, Y.; Otani, M.; Tang, D.; Guo, S.; Zhu, Y.; Zhou, H. Study of the lithium/nickel ions exchange in the layered $\text{LiNi}_{0.42}\text{Mn}_{0.42}\text{Co}_{0.16}\text{O}_2$ cathode material for lithium ion batteries: experimental and first-principles calculations. *Energy Environ. Sci.* **2014**, *7* (3), 1068–1078.
- (190) Sun, H.; Zhao, K. Electronic Structure and Comparative Properties of $\text{LiNi}_x\text{Mn}_y\text{Co}_z\text{O}_2$ Cathode Materials. *J. Phys. Chem. C* **2017**, *121* (11), 6002–6010.
- (191) Min, K.; Kim, K.; Jung, C.; Seo, S.-W.; Song, Y. Y.; Lee, H. S.; Shin, J.; Cho, E. A comparative study of structural changes in lithium nickel cobalt manganese oxide as a function of Ni content during delithiation process. *J. Power Sources* **2016**, *315*, 111–119.
- (192) Aykol, M.; Kim, S.; Wolverton, C. van der Waals Interactions in Layered Lithium Cobalt Oxides. *J. Phys. Chem. C* **2015**, *119* (33), 19053–19058.
- (193) Andersson, A. S.; Thomas, J. O. The source of first-cycle capacity loss in LiFePO_4 . *J. Power Sources* **2001**, *97–98*, 498–502.
- (194) Koyama, Y.; Yabuuchi, N.; Tanaka, I.; Adachi, H.; Ohzuku, T. Solid-State Chemistry and Electrochemistry of $\text{LiCo}_{1/3}\text{Ni}_{1/3}\text{Mn}_{1/3}\text{O}_2$ for Advanced Lithium-Ion Batteries: I. First-Principles Calculation on the Crystal and Electronic Structures. *J. Electrochem. Soc.* **2004**, *151* (10), A1545–A1551.
- (195) Laubach, S.; Laubach, S.; Schmidt, P. C.; Ensling, D.; Schmid, S.; Jaegermann, W.; Thißen, A.; Nikolowski, K.; Ehrenberg, H. Changes in the crystal and electronic structure of LiCoO_2 and LiNiO_2 upon Li intercalation and de-intercalation. *Phys. Chem. Chem. Phys.* **2009**, *11* (17), 3278–3289.
- (196) Yoshida, T.; Hongo, K.; Maezono, R. First-Principles Study of Structural Transitions in LiNiO_2 and High-Throughput Screening for Long Life Battery. *J. Phys. Chem. C* **2019**, *123* (23), 14126–14131.
- (197) Dahéron, L.; Martinez, H.; Dedryvère, R.; Baraille, I.; Ménétrier, M.; Denage, C.; Delmas, C.; Gonbeau, D. Surface Properties of LiCoO_2 Investigated by XPS Analyses and Theoretical Calculations. *J. Phys. Chem. C* **2009**, *113* (14), 5843–5852.
- (198) van Elp, J.; Wieland, J. L.; Eskes, H.; Kuiper, P.; Sawatzky, G. A.; de Groot, F. M. F.; Turner, T. S. Electronic structure of CoO , Li-doped CoO , and LiCoO_2 . *Phys. Rev. B: Condens. Matter Mater. Phys.* **1991**, *44* (12), 6090–6103.
- (199) Kong, F.; Longo, R. C.; Park, M.-S.; Yoon, J.; Yeon, D.-H.; Park, J.-H.; Wang, W.-H.; Kc, S.; Doo, S.-G.; Cho, K. Ab initio study of doping effects on LiMnO_2 and Li_2MnO_3 cathode materials for Li-ion batteries. *J. Mater. Chem. A* **2015**, *3* (16), 8489–8500.
- (200) Zheng, J.; Teng, G.; Xin, C.; Zhuo, Z.; Liu, J.; Li, Q.; Hu, Z.; Xu, M.; Yan, S.; Yang, W.; Pan, F. Role of Supereexchange Interaction on Tuning of Ni/Li Disordering in Layered $\text{Li}(\text{Ni}_x\text{Mn}_y\text{Co}_z)\text{O}_2$. *J. Phys. Chem. Lett.* **2017**, *8* (22), 5537–5542.
- (201) Zhang, M.-J.; Teng, G.; Chen-Wiegart, Y.-C. K.; Duan, Y.; Ko, J. Y. P.; Zheng, J.; Thieme, J.; Dooryhee, E.; Chen, Z.; Bai, J.; Amine, K.; Pan, F.; Wang, F. Cationic Ordering Coupled to Reconstruction of Basic Building Units during Synthesis of High-Ni Layered Oxides. *J. Am. Chem. Soc.* **2018**, *140* (39), 12484–12492.
- (202) Van der Ven, A.; Bhattacharya, J.; Belak, A. A. Understanding Li Diffusion in Li-Intercalation Compounds. *Acc. Chem. Res.* **2013**, *46* (5), 1216–1225.
- (203) Zhou, F.; Cococcioni, M.; Marianetti, C. A.; Morgan, D.; Ceder, G. First-principles prediction of redox potentials in transition-metal compounds with LDA+U. *Phys. Rev. B: Condens. Matter Mater. Phys.* **2004**, *70* (23), 235121.
- (204) Markus, I. M.; Lin, F.; Kam, K. C.; Asta, M.; Doeff, M. M. Computational and Experimental Investigation of Ti Substitution in $\text{Li}_1(\text{Ni}_x\text{Mn}_x\text{Co}_{1-2x-y}\text{Ti}_y)\text{O}_2$ for Lithium Ion Batteries. *J. Phys. Chem. Lett.* **2014**, *5* (21), 3649–3655.
- (205) Seo, D.-H.; Urban, A.; Ceder, G. Calibrating transition-metal energy levels and oxygen bands in first-principles calculations: Accurate prediction of redox potentials and charge transfer in lithium transition-metal oxides. *Phys. Rev. B: Condens. Matter Mater. Phys.* **2015**, *92* (11), 115118.
- (206) Ensling, D.; Thissen, A.; Laubach, S.; Schmidt, P. C.; Jaegermann, W. Electronic structure of LiCoO_2 thin films: A combined photoemission spectroscopy and density functional theory study. *Phys. Rev. B: Condens. Matter Mater. Phys.* **2010**, *82* (19), 195431.
- (207) Santana, J. A.; Kim, J.; Kent, P.; Reboredo, F. A. Successes and failures of Hubbard-corrected density functional theory: The case of Mg doped LiCoO_2 . *J. Chem. Phys.* **2014**, *141* (16), 164706.
- (208) Singh, V.; Kosa, M.; Majhi, K.; Major, D. T. Putting DFT to the Test: A First-Principles Study of Electronic, Magnetic, and Optical Properties of Co_3O_4 . *J. Chem. Theory Comput.* **2015**, *11* (1), 64–72.
- (209) Isaacs, E. B.; Wolverton, C. Performance of the strongly constrained and appropriately normed density functional for solid-state materials. *Phys. Rev. Mater.* **2018**, *2* (6), 063801.
- (210) Park, M.; Zhang, X.; Chung, M.; Less, G. B.; Sastry, A. M. A review of conduction phenomena in Li-ion batteries. *J. Power Sources* **2010**, *195* (24), 7904–7929.
- (211) Wu, M.; Xu, B.; Ouyang, C. Physics of electron and lithium-ion transport in electrode materials for Li-ion batteries. *Chin. Phys. B* **2016**, *25* (1), 018206.
- (212) Yoon, G.; Kim, D.-H.; Park, I.; Chang, D.; Kim, B.; Lee, B.; Oh, K.; Kang, K. Using First-Principles Calculations for the Advancement of Materials for Rechargeable Batteries. *Adv. Funct. Mater.* **2017**, *27* (40), 1702887.
- (213) Van der Ven, A.; Ceder, G.; Asta, M.; Tepesch, P. D. First-principles theory of ionic diffusion with nondilute carriers. *Phys. Rev. B: Condens. Matter Mater. Phys.* **2001**, *64* (18), 184307.
- (214) Henkelman, G.; Jóhannesson, G.; Jónsson, H. *Methods for Finding Saddle Points and Minimum Energy Paths*; Schwartz, S. D., Ed.; Springer Netherlands: Dordrecht, 2002; pp 269–302.
- (215) Ong, S. P.; Chevrier, V. L.; Hautier, G.; Jain, A.; Moore, C.; Kim, S.; Ma, X.; Ceder, G. Voltage, stability and diffusion barrier differences between sodium-ion and lithium-ion intercalation materials. *Energy Environ. Sci.* **2011**, *4* (9), 3680–3688.
- (216) Tian, C.; Lin, F.; Doeff, M. M. Electrochemical Characteristics of Layered Transition Metal Oxide Cathode Materials for Lithium Ion Batteries: Surface, Bulk Behavior, and Thermal Properties. *Acc. Chem. Res.* **2018**, *51* (1), 89–96.
- (217) Piao, J.-Y.; Sun, Y.-G.; Duan, S.-Y.; Cao, A.-M.; Wang, X.-L.; Xiao, R.-J.; Yu, X.-Q.; Gong, Y.; Gu, L.; Li, Y.; Liu, Z.-J.; Peng, Z.-Q.; Qiao, R.-M.; Yang, W.-L.; Yang, X.-Q.; Goodenough, J. B.; Wan, L.-J. Stabilizing Cathode Materials of Lithium-Ion Batteries by Controlling Interstitial Sites on the Surface. *Chem.* **2018**, *4* (7), 1685–1695.

- (218) Qian, J.; Liu, L.; Yang, J.; Li, S.; Wang, X.; Zhuang, H. L.; Lu, Y. Electrochemical surface passivation of LiCoO_2 particles at ultrahigh voltage and its applications in lithium-based batteries. *Nat. Commun.* **2018**, *9* (1), 4918.
- (219) Markevich, E.; Salitra, G.; Aurbach, D. Fluoroethylene Carbonate as an Important Component for the Formation of an Effective Solid Electrolyte Interphase on Anodes and Cathodes for Advanced Li-Ion Batteries. *ACS Energy Lett.* **2017**, *2* (6), 1337–1345.
- (220) Erickson, E. M.; Markevich, E.; Salitra, G.; Sharon, D.; Hirshberg, D.; de la Llave, E.; Shterenberg, I.; Rosenman, A.; Frimer, A.; Aurbach, D. Review—Development of Advanced Rechargeable Batteries: A Continuous Challenge in the Choice of Suitable Electrolyte Solutions. *J. Electrochem. Soc.* **2015**, *162* (14), A2424–A2438.
- (221) Lin, F.; Markus, I. M.; Nordlund, D.; Weng, T.-C.; Asta, M. D.; Xin, H. L.; Doeff, M. M. Surface reconstruction and chemical evolution of stoichiometric layered cathode materials for lithium-ion batteries. *Nat. Commun.* **2014**, *5*, 3529.
- (222) Sun, H.-H.; Manthiram, A. Impact of Microcrack Generation and Surface Degradation on a Nickel-Rich Layered $\text{Li}[\text{Ni}_{0.9}\text{Co}_{0.05}\text{Mn}_{0.05}]\text{O}_2$ Cathode for Lithium-Ion Batteries. *Chem. Mater.* **2017**, *29* (19), 8486–8493.
- (223) Lin, F.; Nordlund, D.; Markus, I. M.; Weng, T.-C.; Xin, H. L.; Doeff, M. M. Profiling the nanoscale gradient in stoichiometric layered cathode particles for lithium-ion batteries. *Energy Environ. Sci.* **2014**, *7* (9), 3077–3085.
- (224) Liang, C.; Longo, R. C.; Kong, F.; Zhang, C.; Nie, Y.; Zheng, Y.; Cho, K. Ab Initio Study on Surface Segregation and Anisotropy of Ni-Rich $\text{LiNi}_{1-2y}\text{Co}_y\text{Mn}_y\text{O}_2$ (NCM) ($y \leq 0.1$) Cathodes. *ACS Appl. Mater. Interfaces* **2018**, *10* (7), 6673–6680.
- (225) Miller, D. J.; Proff, C.; Wen, J. G.; Abraham, D. P.; Bareño, J. Observation of Microstructural Evolution in Li Battery Cathode Oxide Particles by In Situ Electron Microscopy. *Adv. Energy Mater.* **2013**, *3* (8), 1098–1103.
- (226) Ahn, J.; Kim, J. H.; Cho, B. W.; Chung, K. Y.; Kim, S.; Choi, J. W.; Oh, S. H. Nanoscale Zirconium-Abundant Surface Layers on Lithium- and Manganese-Rich Layered Oxides for High-Rate Lithium-Ion Batteries. *Nano Lett.* **2017**, *17* (12), 7869–7877.
- (227) Cabana, J.; Kwon, B. J.; Hu, L. Mechanisms of Degradation and Strategies for the Stabilization of Cathode–Electrolyte Interfaces in Li-Ion Batteries. *Acc. Chem. Res.* **2018**, *51* (2), 299–308.
- (228) Lu, Z.; Chen, G.; Li, Y.; Wang, H.; Xie, J.; Liao, L.; Liu, C.; Liu, Y.; Wu, T.; Li, Y.; Luntz, A. C.; Bajdich, M.; Cui, Y. Identifying the Active Surfaces of Electrochemically Tuned LiCoO_2 for Oxygen Evolution Reaction. *J. Am. Chem. Soc.* **2017**, *139* (17), 6270–6276.
- (229) Tebbe, J. L.; Fuerst, T. F.; Musgrave, C. B. Degradation of Ethylene Carbonate Electrolytes of Lithium Ion Batteries via Ring Opening Activated by LiCoO_2 Cathode Surfaces and Electrolyte Species. *ACS Appl. Mater. Interfaces* **2016**, *8* (40), 26664–26674.
- (230) Giordano, L.; Karayalali, P.; Yu, Y.; Katayama, Y.; Maglia, F.; Lux, S.; Shao-Horn, Y. Chemical Reactivity Descriptor for the Oxide-Electrolyte Interface in Li-Ion Batteries. *J. Phys. Chem. Lett.* **2017**, *8* (16), 3881–3887.
- (231) Xu, S.; Luo, G.; Jacobs, R.; Fang, S.; Mahanthappa, M. K.; Hamers, R. J.; Morgan, D. Ab Initio Modeling of Electrolyte Molecule Ethylene Carbonate Decomposition Reaction on $\text{Li}(\text{Ni},\text{Mn},\text{Co})\text{O}_2$ Cathode Surface. *ACS Appl. Mater. Interfaces* **2017**, *9* (24), 20545–20553.
- (232) Østergaard, T. M.; Giordano, L.; Castelli, I. E.; Maglia, F.; Antonopoulos, B. K.; Shao-Horn, Y.; Rossmeisl, J. Oxidation of Ethylene Carbonate on Li Metal Oxide Surfaces. *J. Phys. Chem. C* **2018**, *122* (19), 10442–10449.
- (233) Sun, W.; Ceder, G. Efficient creation and convergence of surface slabs. *Surf. Sci.* **2013**, *617*, 53–59.
- (234) Huai, L.; Chen, Z.; Li, J. Degradation Mechanism of Dimethyl Carbonate (DMC) Dissociation on the LiCoO_2 Cathode Surface: A First-Principles Study. *ACS Appl. Mater. Interfaces* **2017**, *9* (41), 36377–36384.
- (235) Yu, Y.; Karayalali, P.; Katayama, Y.; Giordano, L.; Gauthier, M.; Maglia, F.; Jung, R.; Lund, I.; Shao-Horn, Y. Coupled LiPF_6 Decomposition and Carbonate Dehydrogenation Enhanced by Highly Covalent Metal Oxides in High-Energy Li-Ion Batteries. *J. Phys. Chem. C* **2018**, *122* (48), 27368–27382.
- (236) Reed, J.; Ceder, G.; Van Der Ven, A. Layered-to-Spinel Phase Transition in Li_xMnO_2 . *Electrochim. Solid-State Lett.* **2001**, *4* (6), A78–A81.
- (237) Zhang, H.; Karki, K.; Huang, Y.; Whittingham, M. S.; Stach, E. A.; Zhou, G. Atomic Insight into the Layered/Spinel Phase Transformation in Charged $\text{LiNi}_{0.80}\text{Co}_{0.15}\text{Al}_{0.05}\text{O}_2$ Cathode Particles. *J. Phys. Chem. C* **2017**, *121* (3), 1421–1430.
- (238) Kong, F.; Liang, C.; Wang, L.; Zheng, Y.; Perananthan, S.; Longo, R. C.; Ferraris, J. P.; Kim, M.; Cho, K. Kinetic Stability of Bulk LiNiO_2 and Surface Degradation by Oxygen Evolution in LiNiO_2 -Based Cathode Materials. *Adv. Energy Mater.* **2019**, *9* (2), 1802586.
- (239) Bak, S.-M.; Hu, E.; Zhou, Y.; Yu, X.; Senanayake, S. D.; Cho, S.-J.; Kim, K.-B.; Chung, K. Y.; Yang, X.-Q.; Nam, K.-W. Structural Changes and Thermal Stability of Charged $\text{LiNi}_x\text{Mn}_y\text{Co}_z\text{O}_2$ Cathode Materials Studied by Combined In Situ Time-Resolved XRD and Mass Spectroscopy. *ACS Appl. Mater. Interfaces* **2014**, *6* (24), 22594–22601.
- (240) Van der Ven, A.; Aydinol, M. K.; Ceder, G.; Kresse, G.; Hafner, J. First-principles investigation of phase stability in Li_xCoO_2 . *Phys. Rev. B: Condens. Matter Mater. Phys.* **1998**, *58* (6), 2975–2987.
- (241) Ceder, G.; Van der Ven, A. Phase diagrams of lithium transition metal oxides: investigations from first principles. *Electrochim. Acta* **1999**, *45* (1), 131–150.
- (242) Reed, J.; Ceder, G. Role of Electronic Structure in the Susceptibility of Metastable Transition-Metal Oxide Structures to Transformation. *Chem. Rev.* **2004**, *104* (10), 4513–4534.
- (243) Reimers, J. N.; Dahn, J. R. Electrochemical and In Situ X-Ray Diffraction Studies of Lithium Intercalation in Li_xCoO_2 . *J. Electrochem. Soc.* **1992**, *139* (8), 2091–2097.
- (244) Arroyo y de Dompablo, M. E.; Van der Ven, A.; Ceder, G. First-principles calculations of lithium ordering and phase stability on Li_xNiO_2 . *Phys. Rev. B: Condens. Matter Mater. Phys.* **2002**, *66* (6), 064112.
- (245) Koyama, Y.; Makimura, Y.; Tanaka, I.; Adachi, H.; Ohzuku, T. Systematic Research on Insertion Materials Based on Superlattice Models in a Phase Triangle of LiCoO_2 LiNiO_2 LiMnO_2 : I. First-Principles Calculation on Electronic and Crystal Structures, Phase Stability and New $\text{LiNi}_{1/2}\text{Mn}_{1/2}\text{O}_2$ Material. *J. Electrochem. Soc.* **2004**, *151* (9), A1499–A1506.
- (246) Gauthier, M.; Carney, T. J.; Grimaud, A.; Giordano, L.; Pour, N.; Chang, H.-H.; Fenning, D. P.; Lux, S. F.; Paschos, O.; Bauer, C.; Maglia, F.; Lupart, S.; Lamp, P.; Shao-Horn, Y. Electrode–Electrolyte Interface in Li-Ion Batteries: Current Understanding and New Insights. *J. Phys. Chem. Lett.* **2015**, *6* (22), 4653–4672.
- (247) Wang, L.; Maxisch, T.; Ceder, G. A First-Principles Approach to Studying the Thermal Stability of Oxide Cathode Materials. *Chem. Mater.* **2007**, *19* (3), 543–552.
- (248) Zheng, J.; Liu, T.; Hu, Z.; Wei, Y.; Song, X.; Ren, Y.; Wang, W.; Rao, M.; Lin, Y.; Chen, Z.; Lu, J.; Wang, C.; Amine, K.; Pan, F. Tuning of Thermal Stability in Layered $\text{Li}(\text{Ni}_x\text{Mn}_y\text{Co}_z)\text{O}_2$. *J. Am. Chem. Soc.* **2016**, *138* (40), 13326–13334.
- (249) Li, W.; Asl, H. Y.; Xie, Q.; Manthiram, A. Collapse of $\text{LiNi}_{1-x-y}\text{CoxMnyO}_2$ Lattice at Deep Charge Irrespective of Nickel Content in Lithium-Ion Batteries. *J. Am. Chem. Soc.* **2019**, *141* (13), 5097–5101.
- (250) Zhang, H.; May, B. M.; Omenya, F.; Whittingham, M. S.; Cabana, J.; Zhou, G. Layered Oxide Cathodes for Li-Ion Batteries: Oxygen Loss and Vacancy Evolution. *Chem. Mater.* **2019**, *31* (18), 7790–7798.
- (251) Liu, D.; Wang, Z.; Chen, L. Comparison of structure and electrochemistry of Al- and Fe-doped $\text{LiNi}_{1/3}\text{Co}_{1/3}\text{Mn}_{1/3}\text{O}_2$. *Electrochim. Acta* **2006**, *51* (20), 4199–4203.
- (252) Liu, L.; Sun, K.; Zhang, N.; Yang, T. Improvement of high-voltage cycling behavior of $\text{LiNi}_{1/3}\text{Co}_{1/3}\text{Mn}_{1/3}\text{O}_2$ cathodes by Mg, Cr,

- and Al substitution. *J. Solid State Electrochem.* **2009**, *13* (9), 1381–1386.
- (253) Wang, D.; Huang, Y.; Huo, Z.; Chen, L. Synthesize and electrochemical characterization of Mg-doped Li-rich layered $\text{Li}[\text{Li}_{0.2}\text{Ni}_{0.6}\text{Mn}_{0.6}]_{\text{O}_2}$ cathode material. *Electrochim. Acta* **2013**, *107*, 461–466.
- (254) Jin, X.; Xu, Q.; Liu, H.; Yuan, X.; Xia, Y. Excellent rate capability of Mg doped $\text{Li}[\text{Li}_{0.2}\text{Ni}_{0.13}\text{Co}_{0.13}\text{Mn}_{0.54}]_{\text{O}_2}$ cathode material for lithium-ion battery. *Electrochim. Acta* **2014**, *136*, 19–26.
- (255) Aurbach, D.; Srur-Lavi, O.; Ghanty, C.; Dixit, M.; Haik, O.; Talianker, M.; Grinblat, Y.; Leifer, N.; Lavi, R.; Major, D. T.; Goobes, G.; Zinigrad, E.; Erickson, E. M.; Kosa, M.; Markovsky, B.; Lampert, J.; Volkov, A.; Shin, J.-Y.; Garsuch, A. Studies of Aluminum-Doped $\text{LiNi}_{0.5}\text{Co}_{0.2}\text{Mn}_{0.3}\text{O}_2$: Electrochemical Behavior, Aging, Structural Transformations, and Thermal Characteristics. *J. Electrochem. Soc.* **2015**, *162* (6), A1014–A1027.
- (256) Chen, C. H.; Liu, J.; Stoll, M. E.; Henriksen, G.; Vissers, D. R.; Amine, K. Aluminum-doped lithium nickel cobalt oxide electrodes for high-power lithium-ion batteries. *J. Power Sources* **2004**, *128* (2), 278–285.
- (257) Ding, Y.; Zhang, P.; Long, Z.; Jiang, Y.; Xu, F. Morphology and electrochemical properties of Al doped $\text{LiNi}_{1/3}\text{Co}_{1/3}\text{Mn}_{1/3}\text{O}_2$ nanofibers prepared by electrospinning. *J. Alloys Compd.* **2009**, *487* (1), 507–510.
- (258) Wu, J.; Liu, H.; Ye, X.; Xia, J.; Lu, Y.; Lin, C.; Yu, X. Effect of Nb doping on electrochemical properties of $\text{LiNi}_{1/3}\text{Co}_{1/3}\text{Mn}_{1/3}\text{O}_2$ at high cutoff voltage for lithium-ion battery. *J. Alloys Compd.* **2015**, *644*, 223–227.
- (259) Liu, S.; Dang, Z.; Liu, D.; Zhang, C.; Huang, T.; Yu, A. Comparative studies of zirconium doping and coating on $\text{LiNi}_{0.6}\text{Co}_{0.2}\text{Mn}_{0.2}\text{O}_2$ cathode material at elevated temperatures. *J. Power Sources* **2018**, *396*, 288–296.
- (260) Ren, H.; Mu, X.; Huang, Y.; Li, Z.; Wang, Y.; Cai, P.; Peng, Z.; Zhou, Y. Effects of Sn doping on electrochemical characterizations of $\text{Li}[\text{Ni}_{1/3}\text{Co}_{1/3}\text{Mn}_{1/3}]_{\text{O}_2}$ cathode material. *Ionics* **2010**, *16* (6), 497–502.
- (261) Park, S.-H.; Oh, S. W.; Sun, Y.-K. Synthesis and structural characterization of layered $\text{Li}[\text{Ni}_{1/3+x}\text{Co}_{1/3}\text{Mn}_{1/3-2x}\text{Mo}_x]_{\text{O}_2}$ cathode materials by ultrasonic spray pyrolysis. *J. Power Sources* **2005**, *146* (1), 622–625.
- (262) Ding, Y.; Zhang, P.; Jiang, Y.; Gao, D. Effect of rare earth elements doping on structure and electrochemical properties of $\text{LiNi}_{1/3}\text{Co}_{1/3}\text{Mn}_{1/3}\text{O}_2$ for lithium-ion battery. *Solid State Ionics* **2007**, *178* (13), 967–971.
- (263) Kim, Y. Effects and distribution of Zr introduced in Ni-based cathode material for Li-ion batteries. *Phys. Chem. Chem. Phys.* **2019**, *21* (23), 12505–12517.
- (264) Makov, G.; Payne, M. C. Periodic boundary conditions in ab initio calculations. *Phys. Rev. B: Condens. Matter Mater. Phys.* **1995**, *51* (7), 4014–4022.
- (265) Freysoldt, C.; Neugebauer, J.; Van de Walle, C. G. Fully Ab Initio Finite-Size Corrections for Charged-Defect Supercell Calculations. *Phys. Rev. Lett.* **2009**, *102* (1), 016402.
- (266) Grey, C. P.; Dupré, N. NMR Studies of Cathode Materials for Lithium-Ion Rechargeable Batteries. *Chem. Rev.* **2004**, *104* (10), 4493–4512.
- (267) Blanc, F.; Leskes, M.; Grey, C. P. In Situ Solid-State NMR Spectroscopy of Electrochemical Cells: Batteries, Supercapacitors, and Fuel Cells. *Acc. Chem. Res.* **2013**, *46* (9), 1952–1963.
- (268) Pecher, O.; Carretero-González, J.; Griffith, K. J.; Grey, C. P. Materials' Methods: NMR in Battery Research. *Chem. Mater.* **2017**, *29* (1), 213–242.
- (269) Chandrashekhar, S.; Trease, N. M.; Chang, H. J.; Du, L.-S.; Grey, C. P.; Jerschow, A. ^7Li MRI of Li batteries reveals location of microstructural lithium. *Nat. Mater.* **2012**, *11*, 311.
- (270) Middlemiss, D. S.; Ilott, A. J.; Clément, R. J.; Strobridge, F. C.; Grey, C. P. Density Functional Theory-Based Bond Pathway Decompositions of Hyperfine Shifts: Equipping Solid-State NMR to Characterize Atomic Environments in Paramagnetic Materials. *Chem. Mater.* **2013**, *25* (9), 1723–1734.
- (271) Wolf, T.; Kumar, S.; Singh, H.; Chakrabarty, T.; Aussenac, F.; Frenkel, A. I.; Major, D. T.; Leskes, M. Endogenous Dynamic Nuclear Polarization for Natural Abundance ^{17}O and Lithium NMR in the Bulk of Inorganic Solids. *J. Am. Chem. Soc.* **2019**, *141* (1), 451–462.
- (272) Pickard, C. J.; Mauri, F. All-electron magnetic response with pseudopotentials: NMR chemical shifts. *Phys. Rev. B: Condens. Matter Mater. Phys.* **2001**, *63* (24), 245101.
- (273) Schwarz, K.; Blaha, P. Solid state calculations using WIEN2k. *Comput. Mater. Sci.* **2003**, *28* (2), 259–273.
- (274) Yates, J. R.; Pickard, C. J.; Mauri, F. Calculation of NMR chemical shifts for extended systems using ultrasoft pseudopotentials. *Phys. Rev. B: Condens. Matter Mater. Phys.* **2007**, *76* (2), 024401.
- (275) de Wijs, G. A.; Laskowski, R.; Blaha, P.; Havenith, R. W. A.; Kresse, G.; Marsman, M. NMR shieldings from density functional perturbation theory: GIPAW versus all-electron calculations. *J. Chem. Phys.* **2017**, *146* (6), 064115.
- (276) Mondal, A.; Gaulois, M. W.; Pell, A. J.; Iannuzzi, M.; Grey, C. P.; Hutter, J.; Kaupp, M. Large-Scale Computation of Nuclear Magnetic Resonance Shifts for Paramagnetic Solids Using CP2K. *J. Chem. Theory Comput.* **2018**, *14* (1), 377–394.
- (277) Petrilli, H. M.; Blöchl, P. E.; Blaha, P.; Schwarz, K. Electric-field-gradient calculations using the projector augmented wave method. *Phys. Rev. B: Condens. Matter Mater. Phys.* **1998**, *57* (23), 14690–14697.
- (278) Ellis, B. L.; Lee, K. T.; Nazar, L. F. Positive Electrode Materials for Li-Ion and Li-Batteries. *Chem. Mater.* **2010**, *22* (3), 691–714.
- (279) Yoon, W.-S.; Chung, K. Y.; McBreen, J.; Yang, X.-Q. A comparative study on structural changes of $\text{LiCo}_{1/3}\text{Ni}_{1/3}\text{Mn}_{1/3}\text{O}_2$ and $\text{LiNi}_{0.8}\text{Co}_{0.15}\text{Al}_{0.05}\text{O}_2$ during first charge using in situ XRD. *Electrochim. Commun.* **2006**, *8* (8), 1257–1262.
- (280) Wilcox, J.; Patoux, S.; Doeuff, M. Structure and Electrochemistry of $\text{LiNi}_{1/3}\text{Co}_{1/3-y}\text{M}_y\text{Mn}_{1/3}\text{O}_2$ ($\text{M} = \text{Ti}, \text{Al}, \text{Fe}$) Positive Electrode Materials. *J. Electrochem. Soc.* **2009**, *156* (3), A192–A198.
- (281) Yabuuchi, N.; Koyama, Y.; Nakayama, N.; Ohzuku, T. Solid-State Chemistry and Electrochemistry of $\text{LiCo}_{1/3}\text{Ni}_{1/3}\text{Mn}_{1/3}\text{O}_2$ for Advanced Lithium-Ion Batteries: II. Preparation and Characterization. *J. Electrochem. Soc.* **2005**, *152* (7), A1434–A1440.
- (282) Karino, W. Order of the transition metal layer in $\text{LiNi}_{1/3}\text{Co}_{1/3}\text{Mn}_{1/3}\text{O}_2$ and stability of the crystal structure. *Ionics* **2016**, *22* (6), 991–995.
- (283) Harris, K. J.; Foster, J. M.; Tessaro, M. Z.; Jiang, M.; Yang, X.; Wu, Y.; Protas, B.; Goward, G. R. Structure Solution of Metal-Oxide Li Battery Cathodes from Simulated Annealing and Lithium NMR Spectroscopy. *Chem. Mater.* **2017**, *29* (13), 5550–5557.
- (284) Yang, C.; Zhang, X.; Huang, M.; Huang, J.; Fang, Z. Preparation and Rate Capability of Carbon Coated $\text{LiNi}_{1/3}\text{Co}_{1/3}\text{Mn}_{1/3}\text{O}_2$ as Cathode Material in Lithium Ion Batteries. *ACS Appl. Mater. Interfaces* **2017**, *9* (14), 12408–12415.
- (285) Zhang, L.-L.; Wang, J.-Q.; Yang, X.-L.; Liang, G.; Li, T.; Yu, P.-L.; Ma, D. Enhanced Electrochemical Performance of Fast Ionic Conductor $\text{LiTi}_2(\text{PO}_4)_3$ -Coated $\text{LiNi}_{1/3}\text{Co}_{1/3}\text{Mn}_{1/3}\text{O}_2$ Cathode Material. *ACS Appl. Mater. Interfaces* **2018**, *10* (14), 11663–11670.
- (286) Zhao, E.; Fang, L.; Chen, M.; Chen, D.; Huang, Q.; Hu, Z.; Yan, Q.-b.; Wu, M.; Xiao, X. New insight into Li/Ni disorder in layered cathode materials for lithium ion batteries: a joint study of neutron diffraction, electrochemical kinetic analysis and first-principles calculations. *J. Mater. Chem. A* **2017**, *5* (4), 1679–1686.
- (287) Bennett, J. W.; Jones, D.; Huang, X.; Hamers, R. J.; Mason, S. E. Dissolution of Complex Metal Oxides from First-Principles and Thermodynamics: Cation Removal from the (001) Surface of $\text{Li}(\text{Ni}_{1/3}\text{Mn}_{1/3}\text{Co}_{1/3})_{\text{O}_2}$. *Environ. Sci. Technol.* **2018**, *52* (10), 5792–5802.
- (288) Hoang, K.; Johanns, M. Defect Physics and Chemistry in Layered Mixed Transition Metal Oxide Cathode Materials: $(\text{Ni},\text{Co},\text{Mn})$ vs $(\text{Ni},\text{Co},\text{Al})$. *Chem. Mater.* **2016**, *28* (5), 1325–1334.

- (289) Garrity, K. F.; Bennett, J. W.; Rabe, K. M.; Vanderbilt, D. Pseudopotentials for high-throughput DFT calculations. *Comput. Mater. Sci.* **2014**, *81*, 446–452.
- (290) Heyd, J.; Scuseria, G. E.; Ernzerhof, M. Hybrid functionals based on a screened Coulomb potential. *J. Chem. Phys.* **2003**, *118* (18), 8207–8215.
- (291) Yin, S. C.; Rho, Y. H.; Swainson, I.; Nazar, L. F. X-ray/Neutron Diffraction and Electrochemical Studies of Lithium De/Re-Intercalation in $\text{Li}_{1-x}\text{Co}_{1/3}\text{Ni}_{1/3}\text{Mn}_{1/3}\text{O}_2$ ($x = 0 \rightarrow 1$). *Chem. Mater.* **2006**, *18* (7), 1901–1910.
- (292) Park, M. S. First-principles study of native point defects in $\text{LiNi}_{1/3}\text{Co}_{1/3}\text{Mn}_{1/3}\text{O}_2$ and Li_2MnO_3 . *Phys. Chem. Chem. Phys.* **2014**, *16* (31), 16798–16804.
- (293) Yoon, W.-S.; Balasubramanian, M.; Chung, K. Y.; Yang, X.-Q.; McBreen, J.; Grey, C. P.; Fischer, D. A. Investigation of the Charge Compensation Mechanism on the Electrochemically Li-Ion Deintercalated $\text{Li}_{1-x}\text{Co}_{1/3}\text{Ni}_{1/3}\text{Mn}_{1/3}\text{O}_2$ Electrode System by Combination of Soft and Hard X-ray Absorption Spectroscopy. *J. Am. Chem. Soc.* **2005**, *127* (49), 17479–17487.
- (294) Wang, Y.; Roller, J.; Maric, R. Morphology-Controlled One-Step Synthesis of Nanostructured $\text{LiNi}_{1/3}\text{Mn}_{1/3}\text{Co}_{1/3}\text{O}_2$ Electrodes for Li-Ion Batteries. *ACS Omega* **2018**, *3* (4), 3966–3973.
- (295) Hoang, K.; Johannes, M. D. Defect chemistry in layered transition-metal oxides from screened hybrid density functional calculations. *J. Mater. Chem. A* **2014**, *2* (15), 5224–5235.
- (296) Kang, K.; Ceder, G. Factors that affect Li mobility in layered lithium transition metal oxides. *Phys. Rev. B: Condens. Matter Mater. Phys.* **2006**, *74* (9), 094105.
- (297) Liu, H.; Bugnet, M.; Tessaro, M. Z.; Harris, K. J.; Dunham, M. J. R.; Jiang, M.; Goward, G. R.; Botton, G. A. Spatially resolved surface valence gradient and structural transformation of lithium transition metal oxides in lithium-ion batteries. *Phys. Chem. Chem. Phys.* **2016**, *18* (42), 29064–29075.
- (298) Lee, J. Y.; Kim, J. Y.; Cho, H. I.; Lee, C. H.; Kim, H. S.; Lee, S. U.; Prosa, T. J.; Larson, D. J.; Yu, T. H.; Ahn, J.-P. Three-dimensional evaluation of compositional and structural changes in cycled $\text{LiNi}_{1/3}\text{Co}_{1/3}\text{Mn}_{1/3}\text{O}_2$ by atom probe tomography. *J. Power Sources* **2018**, *379*, 160–166.
- (299) Zheng, J.; Myeong, S.; Cho, W.; Yan, P.; Xiao, J.; Wang, C.; Cho, J.; Zhang, J.-G. Li- and Mn-Rich Cathode Materials: Challenges to Commercialization. *Adv. Energy Mater.* **2017**, *7* (6), 1601284.
- (300) Garcia, J. C.; Bareño, J.; Yan, J.; Chen, G.; Hauser, A.; Croy, J. R.; Iddir, H. Surface Structure, Morphology, and Stability of $\text{LiNi}_{1/3}\text{Co}_{1/3}\text{Mn}_{1/3}\text{O}_2$ Cathode Material. *J. Phys. Chem. C* **2017**, *121* (15), 8290–8299.
- (301) Zhu, H.; Xie, T.; Chen, Z.; Li, L.; Xu, M.; Wang, W.; Lai, Y.; Li, J. The impact of vanadium substitution on the structure and electrochemical performance of $\text{LiNi}_{0.5}\text{Co}_{0.2}\text{Mn}_{0.3}\text{O}_2$. *Electrochim. Acta* **2014**, *135*, 77–85.
- (302) Li, J.; Zhang, Q.; Liu, C.; He, X. ZrO_2 coating of $\text{LiNi}_{1/3}\text{Co}_{1/3}\text{Mn}_{1/3}\text{O}_2$ cathode materials for Li-ion batteries. *Ionics* **2009**, *15* (4), 493–496.
- (303) Li, J.; Fan, M.; He, X.; Zhao, R.; Jiange, C.; Wan, C. TiO_2 coating of $\text{LiNi}_{1/3}\text{Co}_{1/3}\text{Mn}_{1/3}\text{O}_2$ cathode materials for Li-ion batteries. *Ionics* **2006**, *12* (3), 215–218.
- (304) Lu, J.; Peng, Q.; Wang, W.; Nan, C.; Li, L.; Li, Y. Nanoscale Coating of LiMO_2 ($M = \text{Ni}, \text{Co}, \text{Mn}$) Nanobelts with Li+-Conductive Li_2TiO_3 : Toward Better Rate Capabilities for Li-Ion Batteries. *J. Am. Chem. Soc.* **2013**, *135* (5), 1649–1652.
- (305) Cheng, C.; Chen, F.; Yi, H.; Lai, G. Enhanced electrochemical and safe performances of $\text{LiNi}_{1/3}\text{Co}_{1/3}\text{Mn}_{1/3}\text{O}_2$ by nano- CeO_2 coating via a novel hydrolysis precipitate reaction route. *J. Alloys Compd.* **2018**, *753*, 155–161.
- (306) Myung, S.-T.; Lee, K.-S.; Yoon, C. S.; Sun, Y.-K.; Amine, K.; Yashiro, H. Effect of AlF_3 Coating on Thermal Behavior of Chemically Delithiated $\text{Li}_{0.35}[\text{Ni}_{1/3}\text{Co}_{1/3}\text{Mn}_{1/3}]_{0.2}$. *J. Phys. Chem. C* **2010**, *114* (10), 4710–4718.
- (307) Wang, J.-H.; Wang, Y.; Guo, Y.-Z.; Ren, Z.-Y.; Liu, C.-W. Effect of heat-treatment on the surface structure and electrochemical behavior of AlPO_4 -coated $\text{LiNi}_{1/3}\text{Co}_{1/3}\text{Mn}_{1/3}\text{O}_2$ cathode materials. *J. Mater. Chem. A* **2013**, *1* (15), 4879–4884.
- (308) Venkateswara Rao, C.; Leela Mohana Reddy, A.; Ishikawa, Y.; Ajayan, P. M. $\text{LiNi}_{1/3}\text{Co}_{1/3}\text{Mn}_{1/3}\text{O}_2$ –Graphene Composite as a Promising Cathode for Lithium-Ion Batteries. *ACS Appl. Mater. Interfaces* **2011**, *3* (8), 2966–2972.
- (309) Du, H.; Zheng, Y.; Dou, Z.; Zhan, H. Zn-Doped $\text{LiNi}_{1/3}\text{Co}_{1/3}\text{Mn}_{1/3}\text{O}_2$ Composite as Cathode Material for Lithium Ion Battery: Preparation, Characterization, and Electrochemical Properties. *J. Nanomater.* **2015**, *2015*, 867618.
- (310) Liu, Z.; Yu, A.; Lee, J. Y. Synthesis and characterization of $\text{LiNi}_{1-x-y}\text{Co}_x\text{Mn}_y\text{O}_2$ as the cathode materials of secondary lithium batteries. *J. Power Sources* **1999**, *81*–82, 416–419.
- (311) Hua, W.; Zhang, J.; Zheng, Z.; Liu, W.; Peng, X.; Guo, X.-D.; Zhong, B.; Wang, Y.-J.; Wang, X. Na-doped Ni-rich $\text{LiNi}_{0.5}\text{Co}_{0.2}\text{Mn}_{0.3}\text{O}_2$ cathode material with both high rate capability and high tap density for lithium ion batteries. *Dalton Trans.* **2014**, *43* (39), 14824–14832.
- (312) Choi, M.-H.; Yoon, C. S.; Myung, S.-T.; Lim, B.-B.; Komaba, S.; Sun, Y.-K. Effect of Lithium in Transition Metal Layers of Ni-Rich Cathode Materials on Electrochemical Properties. *J. Electrochem. Soc.* **2015**, *162* (12), A2313–A2318.
- (313) Zhao, X.; An, L.; Sun, J.; Liang, G. $\text{LiNi}_{0.5}\text{Co}_{0.2}\text{Mn}_{0.3}\text{O}_2$ hollow microspheres-synthesis, characterization and application as cathode materials for power lithium ion batteries. *J. Electroanal. Chem.* **2018**, *810*, 1–10.
- (314) Wang, D.; Li, X.; Wang, Z.; Guo, H.; Xu, Y.; Fan, Y.; Ru, J. Role of zirconium dopant on the structure and high voltage electrochemical performances of $\text{LiNi}_{0.5}\text{Co}_{0.2}\text{Mn}_{0.3}\text{O}_2$ cathode materials for lithium ion batteries. *Electrochim. Acta* **2016**, *188*, 48–56.
- (315) Zhang, Y.; Wang, Z.-B.; Yu, F.-D.; Que, L.-F.; Wang, M.-J.; Xia, Y.-F.; Xue, Y.; Wu, J. Studies on stability and capacity for long-life cycle performance of $\text{Li}(\text{Ni}_{0.5}\text{Co}_{0.2}\text{Mn}_{0.3})\text{O}_2$ by Mo modification for lithium-ion battery. *J. Power Sources* **2017**, *358*, 1–12.
- (316) Han, B.; Paulauskas, T.; Key, B.; Peebles, C.; Park, J. S.; Klie, R. F.; Vaughtey, J. T.; Dogan, F. Understanding the Role of Temperature and Cathode Composition on Interface and Bulk: Optimizing Aluminum Oxide Coatings for Li-Ion Cathodes. *ACS Appl. Mater. Interfaces* **2017**, *9* (17), 14769–14778.
- (317) Hu, G.; Zhang, M.; Liang, L.; Peng, Z.; Du, K.; Cao, Y. Mg–Al–B co-substitution $\text{LiNi}_{0.5}\text{Co}_{0.2}\text{Mn}_{0.3}\text{O}_2$ cathode materials with improved cycling performance for lithium-ion battery under high cutoff voltage. *Electrochim. Acta* **2016**, *190*, 264–275.
- (318) Mo, Y.; Li, D.; Chen, Y.; Cao, B.; Hou, B.; Zhu, Z.; Li, J. Synthesis and characterization of $\text{LiNi}_{0.48}\text{Co}_{0.18}\text{Mn}_{0.3}\text{Mg}_{0.02}\text{Ti}_{0.02}\text{O}_2$ as a cathode material for lithium ion batteries. *RSC Adv.* **2016**, *6* (79), 75293–75298.
- (319) Wu, Z.; Han, X.; Zheng, J.; Wei, Y.; Qiao, R.; Shen, F.; Dai, J.; Hu, L.; Xu, K.; Lin, Y.; Yang, W.; Pan, F. Depolarized and Fully Active Cathode Based on $\text{Li}(\text{Ni}_{0.5}\text{Co}_{0.2}\text{Mn}_{0.3})\text{O}_2$ Embedded in Carbon Nanotube Network for Advanced Batteries. *Nano Lett.* **2014**, *14* (8), 4700–4706.
- (320) Wu, Z.; Ji, S.; Zheng, J.; Hu, Z.; Xiao, S.; Wei, Y.; Zhuo, Z.; Lin, Y.; Yang, W.; Xu, K.; Amine, K.; Pan, F. Prelithiation Activates $\text{Li}(\text{Ni}_{0.5}\text{Mn}_{0.3}\text{Co}_{0.2})\text{O}_2$ for High Capacity and Excellent Cycling Stability. *Nano Lett.* **2015**, *15* (8), 5590–5596.
- (321) Mo, Y.; Guo, L.; Cao, B.; Wang, Y.; Zhang, L.; Jia, X.; Chen, Y. Correlating structural changes of the improved cyclability upon Nd-substitution in $\text{LiNi}_{0.5}\text{Co}_{0.2}\text{Mn}_{0.3}\text{O}_2$ cathode materials. *Energy Storage Mater.* **2019**, *18*, 260–268.
- (322) Liang, L.; Du, K.; Peng, Z.; Cao, Y.; Duan, J.; Jiang, J.; Hu, G. Co-precipitation synthesis of $\text{Ni}_{0.6}\text{Co}_{0.2}\text{Mn}_{0.2}(\text{OH})_2$ precursor and characterization of $\text{LiNi}_{0.6}\text{Co}_{0.2}\text{Mn}_{0.2}\text{O}_2$ cathode material for secondary lithium batteries. *Electrochim. Acta* **2014**, *130*, 82–89.
- (323) Ryu, H.-H.; Park, K.-J.; Yoon, C. S.; Sun, Y.-K. Capacity Fading of Ni-Rich $\text{Li}[\text{Ni}_{x}\text{Co}_y\text{Mn}_{1-x-y}]_{0.2}$ ($0.6 \leq x \leq 0.95$) Cathodes for High-Energy-Density Lithium-Ion Batteries: Bulk or Surface Degradation? *Chem. Mater.* **2018**, *30* (3), 1155–1163.

- (324) Fu, J.; Mu, D.; Wu, B.; Bi, J.; Liu, X.; Peng, Y.; Li, Y.; Wu, F. Enhanced electrochemical performance of $\text{LiNi}_{0.6}\text{Co}_{0.2}\text{Mn}_{0.2}\text{O}_2$ cathode at high cutoff voltage by modifying electrode/electrolyte interface with lithium metasilicate. *Electrochim. Acta* **2017**, *246*, 27–34.
- (325) Tao, T.; Chen, C.; Yao, Y.; Liang, B.; Lu, S.; Chen, Y. Enhanced electrochemical performance of ZrO_2 modified $\text{Li-Ni}_{0.6}\text{Co}_{0.2}\text{Mn}_{0.2}\text{O}_2$ cathode material for lithium ion batteries. *Ceram. Int.* **2017**, *43* (17), 15173–15178.
- (326) Fu, J.; Mu, D.; Wu, B.; Bi, J.; Cui, H.; Yang, H.; Wu, H.; Wu, F. Electrochemical Properties of the $\text{LiNi}_{0.6}\text{Co}_{0.2}\text{Mn}_{0.2}\text{O}_2$ Cathode Material Modified by Lithium Tungstate under High Voltage. *ACS Appl. Mater. Interfaces* **2018**, *10* (23), 19704–19711.
- (327) Wang, Q.; Shen, C.-H.; Shen, S.-Y.; Xu, Y.-F.; Shi, C.-G.; Huang, L.; Li, J.-T.; Sun, S.-G. Origin of Structural Evolution in Capacity Degradation for Overcharged NMC622 via Operando Coupled Investigation. *ACS Appl. Mater. Interfaces* **2017**, *9* (29), 24731–24742.
- (328) Wang, H.; Sun, D.; Li, X.; Ge, W.; Deng, B.; Qu, M.; Peng, G. Alternative Multifunctional Cyclic Organosilicon as an Efficient Electrolyte Additive for High Performance Lithium-Ion Batteries. *Electrochim. Acta* **2017**, *254*, 112–122.
- (329) Kaneda, H.; Koshika, Y.; Nakamura, T.; Nagata, H.; Ushio, R.; Mor, K. Improving the cycling performance and thermal stability of $\text{LiNi}_{0.6}\text{Co}_{0.2}\text{Mn}_{0.2}\text{O}_2$ cathode materials by Nb - doping and surface modification. *Int. J. Electrochem. Sci.* **2017**, *12* (5), 4640–4653.
- (330) Liu, S.; Chen, X.; Zhao, J.; Su, J.; Zhang, C.; Huang, T.; Wu, J.; Yu, A. Uncovering the role of Nb modification in improving the structure stability and electrochemical performance of $\text{Li-Ni}_{0.6}\text{Co}_{0.2}\text{Mn}_{0.2}\text{O}_2$ cathode charged at higher voltage of 4.5 V. *J. Power Sources* **2018**, *374*, 149–157.
- (331) Sun, S.; Du, C.; Qu, D.; Zhang, X.; Tang, Z. Li_2ZrO_3 -coated $\text{LiNi}_{0.6}\text{Co}_{0.2}\text{Mn}_{0.2}\text{O}_2$ for high-performance cathode material in lithium-ion battery. *Ionics* **2015**, *21* (7), 2091–2100.
- (332) Peng, Z.; Yang, G.; Li, F.; Zhu, Z.; Liu, Z. Improving the cathode properties of Ni-rich $\text{LiNi}_{0.6}\text{Co}_{0.2}\text{Mn}_{0.2}\text{O}_2$ at high voltages under 5 C by Li_2SiO_3 coating and Si^{4+} doping. *J. Alloys Compd.* **2018**, *762*, 827–834.
- (333) Neudeck, S.; Walther, F.; Bergfeldt, T.; Suchomski, C.; Rohnke, M.; Hartmann, P.; Janek, J.; Brezesinski, T. Molecular Surface Modification of NCM622 Cathode Material Using Organophosphates for Improved Li-Ion Battery Full-Cells. *ACS Appl. Mater. Interfaces* **2018**, *10* (24), 20487–20498.
- (334) Jo, C.-H.; Cho, D.-H.; Noh, H.-J.; Yashiro, H.; Sun, Y.-K.; Myung, S. T. An effective method to reduce residual lithium compounds on Ni-rich $\text{Li}[\text{Ni}_{0.6}\text{Co}_{0.2}\text{Mn}_{0.2}] \text{O}_2$ active material using a phosphoric acid derived Li_3PO_4 nanolayer. *Nano Res.* **2015**, *8* (5), 1464–1479.
- (335) Deng, B.; Wang, H.; Ge, W.; Li, X.; Yan, X.; Chen, T.; Qu, M.; Peng, G. Investigating the influence of high temperatures on the cycling stability of a $\text{LiNi}_{0.6}\text{Co}_{0.2}\text{Mn}_{0.2}\text{O}_2$ cathode using an innovative electrolyte additive. *Electrochim. Acta* **2017**, *236*, 61–71.
- (336) Kim, Y. Lithium Nickel Cobalt Manganese Oxide Synthesized Using Alkali Chloride Flux: Morphology and Performance As a Cathode Material for Lithium Ion Batteries. *ACS Appl. Mater. Interfaces* **2012**, *4* (5), 2329–2333.
- (337) Kondrakov, A. O.; Geßwein, H.; Galdina, K.; de Biasi, L.; Meded, V.; Filatova, E. O.; Schumacher, G.; Wenzel, W.; Hartmann, P.; Brezesinski, T.; Janek, J. Charge-Transfer-Induced Lattice Collapse in Ni-Rich NCM Cathode Materials during Delithiation. *J. Phys. Chem. C* **2017**, *121* (44), 24381–24388.
- (338) Lim, J.-M.; Hwang, T.; Kim, D.; Park, M.-S.; Cho, K.; Cho, M. Intrinsic Origins of Crack Generation in Ni-rich $\text{LiNi}_{0.8}\text{Co}_{0.1}\text{Mn}_{0.1}\text{O}_2$ Layered Oxide Cathode Material. *Sci. Rep.* **2017**, *7*, 39669.
- (339) Märker, K.; Reeves, P. J.; Xu, C.; Griffith, K. J.; Grey, C. P. Evolution of Structure and Lithium Dynamics in $\text{LiNi}_{0.8}\text{Mn}_{0.1}\text{Co}_{0.1}\text{O}_2$ (NMC811) Cathodes during Electrochemical Cycling. *Chem. Mater.* **2019**, *31* (7), 2545–2554.
- (340) Manthiram, A.; Song, B.; Li, W. A perspective on nickel-rich layered oxide cathodes for lithium-ion batteries. *Energy Storage Mater.* **2017**, *6*, 125–139.
- (341) Xiong, X.; Ding, D.; Bu, Y.; Wang, Z.; Huang, B.; Guo, H.; Li, X. Enhanced electrochemical properties of a LiNiO_2 -based cathode material by removing lithium residues with $(\text{NH}_4)_2\text{HPO}_4$. *J. Mater. Chem. A* **2014**, *2* (30), 11691–11696.
- (342) Eom, J.; Kim, M. G.; Cho, J. Storage Characteristics of $\text{LiNi}_{0.8}\text{Co}_{0.1+x}\text{Mn}_{0.1-x}\text{O}_2$ ($x = 0, 0.03$, and 0.06) Cathode Materials for Lithium Batteries. *J. Electrochem. Soc.* **2008**, *155* (3), A239–A245.
- (343) Li, Q.; Dang, R.; Chen, M.; Lee, Y.; Hu, Z.; Xiao, X. Synthesis Method for Long Cycle Life Lithium-Ion Cathode Material: Nickel-Rich Core–Shell $\text{LiNi}_{0.8}\text{Co}_{0.1}\text{Mn}_{0.1}\text{O}_2$. *ACS Appl. Mater. Interfaces* **2018**, *10* (21), 17850–17860.
- (344) Ranganathan, S. On the geometry of coincidence-site lattices. *Acta Crystallogr.* **1966**, *21* (2), 197–199.
- (345) Zhang, Z.; Chen, D.; Chang, C. Improved electrochemical performance of $\text{LiNi}_{0.8}\text{Co}_{0.1}\text{Mn}_{0.1}\text{O}_2$ cathode materials via incorporation of rubidium cations into the original Li sites. *RSC Adv.* **2017**, *7* (81), 51721–51728.
- (346) Li, L.-J.; Li, X.-H.; Wang, Z.-X.; Guo, H.-J.; Yue, P.; Chen, W.; Wu, L. Synthesis, structural and electrochemical properties of $\text{LiNi}_{0.79}\text{Co}_{0.1}\text{Mn}_{0.1}\text{Cr}_{0.01}\text{O}_2$ via fast co-precipitation. *J. Alloys Compd.* **2010**, *507* (1), 172–177.
- (347) Sun, H.-H.; Choi, W.; Lee, J. K.; Oh, I.-H.; Jung, H.-G. Control of electrochemical properties of nickel-rich layered cathode materials for lithium ion batteries by variation of the manganese to cobalt ratio. *J. Power Sources* **2015**, *275*, 877–883.
- (348) Li, H.; Cormier, M.; Zhang, N.; Inglis, J.; Li, J.; Dahn, J. R. Is Cobalt Needed in Ni-Rich Positive Electrode Materials for Lithium Ion Batteries? *J. Electrochem. Soc.* **2019**, *166* (4), A429–A439.
- (349) Park, K.-J.; Jung, H.-G.; Kuo, L.-Y.; Kaghazchi, P.; Yoon, C. S.; Sun, Y.-K. Improved Cycling Stability of $\text{Li}[\text{Ni}_{0.90}\text{Co}_{0.05}\text{Mn}_{0.05}] \text{O}_2$ Through Microstructure Modification by Boron Doping for Li-Ion Batteries. *Adv. Energy Mater.* **2018**, *8* (25), 1801202.
- (350) Ma, M.; Chernova, N. A.; Toby, B. H.; Zavalij, P. Y.; Whittingham, M. S. Structural and electrochemical behavior of $\text{LiMn}_{0.4}\text{Ni}_{0.4}\text{Co}_{0.2}\text{O}_2$. *J. Power Sources* **2007**, *165* (2), 517–534.
- (351) Leifer, N.; Srur-Lavi, O.; Matlahov, I.; Markovsky, B.; Aurbach, D.; Goobes, G. $\text{LiNi}_{0.8}\text{Co}_{0.15}\text{Al}_{0.05}\text{O}_2$ Cathode Material: New Insights via ^7Li and ^{27}Al Magic-Angle Spinning NMR Spectroscopy. *Chem. Mater.* **2016**, *28* (21), 7594–7604.
- (352) Ohzuku, T.; Yanagawa, T.; Kouuchi, M.; Ueda, A. Innovative insertion material of $\text{LiAl}_{1/4}\text{Ni}_{3/4}\text{O}_2$ (R-m) for lithium-ion (shuttlecock) batteries. *J. Power Sources* **1997**, *68* (1), 131–134.
- (353) Lin, Y.-K.; Lu, C.-H.; Wu, H.-C.; Yang, M.-H. New layer-structured $\text{LiNi}_{1/3}\text{Co}_{1/3}\text{Al}_{1/3}\text{O}_2$ prepared via water-in-oil microemulsion method. *J. Power Sources* **2005**, *146* (1), 594–597.
- (354) Love, C. T.; Johannes, M. D.; Swider-Lyons, K. Thermal Stability of Delithiated Al-substituted $\text{Li}(\text{Ni}_{1/3}\text{Co}_{1/3}\text{Mn}_{1/3}) \text{O}_2$ Cathodes. *ECS Trans.* **2009**, *25* (36), 231–240.
- (355) Miyashiro, H.; Kobayashi, Y.; Seki, S.; Mita, Y.; Usami, A.; Nakayama, M.; Wakihara, M. Fabrication of All-Solid-State Lithium Polymer Secondary Batteries Using Al_2O_3 -Coated LiCoO_2 . *Chem. Mater.* **2005**, *17* (23), S603–S605.
- (356) Cho, J.; Kim, Y. J.; Park, B. Novel LiCoO_2 Cathode Material with Al_2O_3 Coating for a Li Ion Cell. *Chem. Mater.* **2000**, *12* (12), 3788–3791.
- (357) Zuo, D.; Tian, G.; Li, X.; Chen, D.; Shu, K. Recent progress in surface coating of cathode materials for lithium ion secondary batteries. *J. Alloys Compd.* **2017**, *706*, 24–40.
- (358) Cao, H.; Xia, B.; Xu, N.; Zhang, C. Structural and electrochemical characteristics of Co and Al co-doped lithium nickelate cathode materials for lithium-ion batteries. *J. Alloys Compd.* **2004**, *376* (1), 282–286.
- (359) Doeff, M. M. Batteries for Sustainability: Selected Entries from the Encyclopedia of Sustainability Science and Technology. In *Batteries for Sustainability: Selected Entries from the Encyclopedia of*

- Sustainability Science and Technology*; Brodd, R. J., Ed.; Springer New York: New York, NY, 2013; pp 5–49.
- (360) Kondo, H.; Takeuchi, Y.; Sasaki, T.; Kawauchi, S.; Itou, Y.; Hiruta, O.; Okuda, C.; Yonemura, M.; Kamiyama, T.; Ukyo, Y. Effects of Mg-substitution in Li(Ni_xCo_{1-x}Al)O₂ positive electrode materials on the crystal structure and battery performance. *J. Power Sources* **2007**, *174* (2), 1131–1136.
- (361) Eremin, R. A.; Zolotarev, P. N.; Ivanshina, O. Y.; Bobrikov, I. A. Li(Ni_xCo_{1-x}Al)O₂ Cathode Delithiation: A Combination of Topological Analysis, Density Functional Theory, Neutron Diffraction, and Machine Learning Techniques. *J. Phys. Chem. C* **2017**, *121* (51), 28293–28305.
- (362) Flores, E.; Vonrütli, N.; Novák, P.; Aschauer, U.; Berg, E. J. Elucidation of Li_xNi_{0.8}Co_{0.15}Al_{0.05}O₂ Redox Chemistry by Operando Raman Spectroscopy. *Chem. Mater.* **2018**, *30* (14), 4694–4703.
- (363) Srur-Lavi, O.; Miikkulainen, V.; Markovsky, B.; Grinblat, J.; Taliander, M.; Fleger, Y.; Cohen-Taguri, G.; Mor, A.; Tal-Yosef, Y.; Aurbach, D. Studies of the Electrochemical Behavior of Li-Ni_{0.80}Co_{0.15}Al_{0.05}O₂ Electrodes Coated with LiAlO₂. *J. Electrochem. Soc.* **2017**, *164* (13), A3266–A3275.
- (364) Ghatak, K.; Basu, S.; Das, T.; Sharma, V.; Kumar, H.; Datta, D. Effect of cobalt content on the electrochemical properties and structural stability of NCA type cathode materials. *Phys. Chem. Chem. Phys.* **2018**, *20* (35), 22805–22817.
- (365) Amin, R.; Ravnsbæk, D. B.; Chiang, Y.-M. Characterization of Electronic and Ionic Transport in Li_{1-x}Ni_{0.8}Co_{0.15}Al_{0.05}O₂ (NCA). *J. Electrochem. Soc.* **2015**, *162* (7), A1163–A1169.
- (366) Zhang, L.; Luo, F.; Wang, J. H.; Guo, Y. Z. Surface Coating and Electrochemical Properties of LiNi_{0.8}Co_{0.15}Al_{0.05}O₂ Cathode in Lithium-Ion Cells. *Adv. Mater. Res.* **2014**, *1058*, 317–320.
- (367) Karki, K.; Huang, Y.; Hwang, S.; Gamalski, A. D.; Whittingham, M. S.; Zhou, G.; Stach, E. A. Tuning the Activity of Oxygen in LiNi_{0.8}Co_{0.15}Al_{0.05}O₂ Battery Electrodes. *ACS Appl. Mater. Interfaces* **2016**, *8* (41), 27762–27771.
- (368) Zhang, H.; May, B. M.; Serrano-Sevillano, J.; Casas-Cabanas, M.; Cabana, J.; Wang, C.; Zhou, G. Facet-Dependent Rock-Salt Reconstruction on the Surface of Layered Oxide Cathodes. *Chem. Mater.* **2018**, *30* (3), 692–699.
- (369) Park, K.-J.; Choi, M.-J.; Maglia, F.; Kim, S.-J.; Kim, K.-H.; Yoon, C. S.; Sun, Y.-K. High-Capacity Concentration Gradient Li[Ni_{0.865}Co_{0.120}Al_{0.015}]O₂ Cathode for Lithium-Ion Batteries. *Adv. Energy Mater.* **2018**, *8* (19), 1703612.
- (370) Trepka, B.; Erler, P.; Selzer, S.; Kollek, T.; Boldt, K.; Fonin, M.; Nowak, U.; Wolf, D.; Lubk, A.; Polarz, S. Nanomorphology Effects in Semiconductors with Native Ferromagnetism: Hierarchical Europium (II) Oxide Tubes Prepared via a Topotactic Nanostructure Transition. *Adv. Mater.* **2018**, *30* (1), 1703612.
- (371) Park, K.-J.; Hwang, J.-Y.; Ryu, H.-H.; Maglia, F.; Kim, S.-J.; Lamp, P.; Yoon, C. S.; Sun, Y.-K. Degradation Mechanism of Ni-Enriched NCA Cathode for Lithium Batteries: Are Microcracks Really Critical? *ACS Energy Lett.* **2019**, *4* (6), 1394–1400.
- (372) Zhang, B.; Xie, H.; Lu, B.; Chen, X.; Xing, P.; Qu, J.; Song, Q.; Yin, H. A Green Electrochemical Process to Recover Co and Li from Spent LiCoO₂-Based Batteries in Molten Salts. *ACS Sustainable Chem. Eng.* **2019**, *7* (15), 13391–13399.
- (373) Lv, W.; Wang, Z.; Cao, H.; Sun, Y.; Zhang, Y.; Sun, Z. A Critical Review and Analysis on the Recycling of Spent Lithium-Ion Batteries. *ACS Sustainable Chem. Eng.* **2018**, *6* (2), 1504–1521.
- (374) Zheng, X.; Zhu, Z.; Lin, X.; Zhang, Y.; He, Y.; Cao, H.; Sun, Z. A Mini-Review on Metal Recycling from Spent Lithium Ion Batteries. *Engineering* **2018**, *4* (3), 361–370.
- (375) Contestabile, M.; Panero, S.; Scrosati, B. A laboratory-scale lithium-ion battery recycling process. *J. Power Sources* **2001**, *92* (1), 65–69.
- (376) Natarajan, S.; Aravindan, V. Recycling Strategies for Spent Li-Ion Battery Mixed Cathodes. *ACS Energy Lett.* **2018**, *3* (9), 2101–2103.
- (377) Hang, M. N.; Hudson-Smith, N. V.; Clement, P. L.; Zhang, Y.; Wang, C.; Haynes, C. L.; Hamers, R. J. Influence of Nanoparticle Morphology on Ion Release and Biological Impact of Nickel Manganese Cobalt Oxide (NMC) Complex Oxide Nanomaterials. *ACS Appl. Nano Mater.* **2018**, *1* (4), 1721–1730.
- (378) Notter, D. A.; Gauch, M.; Widmer, R.; Wäger, P.; Stamp, A.; Zah, R.; Althaus, H.-J. Contribution of Li-Ion Batteries to the Environmental Impact of Electric Vehicles. *Environ. Sci. Technol.* **2010**, *44* (17), 6550–6556.
- (379) Xu, J.; Thomas, H. R.; Francis, R. W.; Lum, K. R.; Wang, J.; Liang, B. A review of processes and technologies for the recycling of lithium-ion secondary batteries. *J. Power Sources* **2008**, *177* (2), 512–527.
- (380) Zhang, X.; Xie, Y.; Lin, X.; Li, H.; Cao, H. An overview on the processes and technologies for recycling cathodic active materials from spent lithium-ion batteries. *J. Mater. Cycles Waste Manage.* **2013**, *15* (4), 420–430.
- (381) Ali, A.-T.; Bennett, J. W.; Jones, D. T.; Cartagena-Gonzalez, N.; Jones, Z. R.; Laudadio, E. D.; Hamers, R. J.; Santana, J. A.; Mason, S. E. DFT and Thermodynamics Calculations of Surface Cation Release in LiCoO₂. *ChemRxiv* 9764774, 2019, DOI: [10.26434/chemrxiv.9764774.v1](https://doi.org/10.26434/chemrxiv.9764774.v1) (accessed on December 31, 2019).
- (382) Bennett, J. W.; Jones, D. T.; Hamers, R. J.; Mason, S. E. First-Principles and Thermodynamics Study of Compositionally Tuned Complex Metal Oxides: Cation Release from the (001) Surface of Mn-Rich Lithium Nickel Manganese Cobalt Oxide. *Inorg. Chem.* **2018**, *57* (21), 13300–13311.
- (383) Warshel, A. Multiscale Modeling of Biological Functions: From Enzymes to Molecular Machines (Nobel Lecture). *Angew. Chem., Int. Ed.* **2014**, *53*, 10020–10031.